Master's thesis

NTNU
Norwegian University of Science and Technology
Faculty of Engineering
Department of Marine Technology

Øyvind Onestad Olsen

A Numerical Study of a Multi-torus Floating Solar Island Concept, with the use of Computer Programming

Master's thesis in Marine Hydrodynamics
Supervisor: Trygve Kristiansen
June 2020

NTNU
Norwegian University of
Science and Technology

Øyvind Onestad Olsen

A Numerical Study of a Multi-torus Floating Solar Island Concept, with the use of Computer Programming

Master's thesis in Marine Hydrodynamics
Supervisor: Trygve Kristiansen
June 2020

Norwegian University of Science and Technology
Faculty of Engineering
Department of Marine Technology

NTNU
Norwegian University of
Science and Technology

Preface

This Master's thesis is the concluding part of my Master of Science degree in Marine Hydrodynamics at the Department of Marine Technology (IMT), at the Norwegian University of Science and Technology (NTNU) in Trondheim, Norway. The work was carried out during the spring of 2020, and is a continuation of my project thesis carried out during the autumn of 2019.

The thesis investigates the response of a floating solar island, in a given sea-state using a numerical method. The floater solar island concept was first introduced by Prof. Bruce Patterson at the University of Zürich, proposing the idea of utilising solar energy to extract CO_2 from sea-water to produce methanol. Professor Trygve Kristiansen at the Department of Marin Hydrodynamics (NTNU), proposed the multi-tori concept of the solar island. He has been my supervisor throughout the 5^{th} year, guiding me with the project thesis and the Master's thesis.

The whole work, except writing of thesis, was done in collaboration with fellow student, Svanhild Toppe Tolaas.

The reader should have basic knowledge regarding hydrodynamics and structural dynamics.

Øyvind Onestad Olsen

Trondheim, June 10, 2020, Øyvind Onestad Olsen

Acknowledgements

I want to express my sincere gratitude to my supervisor, Prof. Trygve Kristiansen, for his devotion and guidance during the work of this Master's thesis. His knowledge and way of thinking have been genuinely inspiring. It has been rewarding, and much appreciated to discuss new topics. Thank you for answering countless of e-mails and for always being available, especially after the $COVID - 19$ outbreak. Moreover, I could not have asked for a better mentor.

I want to thank my fellow student and friend, Svanhild Toppe Tolaas. It has been a pleasure working together. Her knowledge, and always positive attitude to new challenges, have made this work both educational and joyful. I want to thank for all Zoom-meetings during the last couple of months. It would not have been possible without her.

Lastly, I would like to thank all my fellow student for five memorable years. It has been a pleasure getting to know all of you.

Summary

A semi-submerged multi-torus model is numerically implemented to investigate the response of such structure. The numerical model, consisting of tori connected with elastic bands (trusses), have been created with the programming software MATLAB, using relevant theory.

The verification study considers a single-torus model with a previously made truss model. Time-step study and study of damp ratio ξ, show promising results for each motion of a single-torus. They are indicating correct implementation. Previous experimental results are used as a tool to investigate possible structural- or hydrodynamic interaction between the tori. The multi-torus model is solved for a two-tori concept and a five-tori concept.

Results from the response amplitude operator (RAO) show that the innermost torus generally has the most significant deviation to the theory. Heave and pitch response are compared to the zero-frequency theory (ZFT) for a single floater. The results correspond well for low wavenumbers. With increasing wave number, a deviation is observed. Compared to experiments, the deviations do not show similar trends. Thus, the deviation from experiment is believed to be caused by other effects.

Radial modes and surge show more substantial deviation from theory, for all tori. For the five-tori case, surge is found to have a resonance at $kR \simeq 5$. This is believed to be due to structural interactions between the tori, through the elastic bands.

An analysis of hydrodynamic interactions for five-tori without elastic bands, show some influence in RAO, compared to theory, but cannot alone explain the deviation seen in the experiments.

Unfortunately, the numerical model has an unresolved error. Countless attempts of debug were made but with no success. After closer study on the effect of this error, it is questioned whether the model gives non-realistic results. The error is found to be small, and thus, the numerical model is believed to describe the system correctly to some extent.

The concluding remarks can be summarised by the numerical model for implementing the multi-torus concept showing potential. The model is successfully generalised to take any number of tori, and elastic band. It shows indication of capturing certain phenomena like structural- and hydrodynamic interaction. Although containing an unknown error, the code is a solid foundation for further development.

Sammendrag

En halvt nedsenket fler-torus modell er implementert numerisk, med hensikt å undersøke responsen til en slik struktur. Den numeriske modellen, bestående av flere sirkulære flytere koblet sammen med elastiske bånd (strekkstag), er laget med programmeringsprogramvaren MATLAB, ved bruk av relevant teori.

Verifiseringsstudiet betrakter en modell av en enkel flyter med en tidligere strekkstag-modell. Tids-steg studie og studie av dempnings forholdet ξ, viser lovende resultater for bevegelse av en enkelt flyter. Hvilket indikerer riktig implementering av modellen. Tidligere eksperimentelle resultater brukes som verktøy for å undersøke mulig strukturell eller hydrodynamisk interaksjon mellom de ulike flyterne. Den fullstendige modellen er laget for et to-flyter-konsept og et fem-flyter-konsept.

Resultater fra RAOer viser at den innerste flyteren generelt har størst avvik fra teorien. Hiv og stamp sammenlignes med null-frekvens-teorien (ZFT) for en enkelt flyter. Resultatene tilsvarer godt for lave bølgetall. Med økende bølgetall observeres et avvik. Sammenlignet med eksperimenter er ikke disse avvikene sammenlignbare og tyder på at avvik fra eksperiment skyldes andre faktorer.

Radielle moder og jag viser sterkere avvik fra teori, for alle flytere. For tilfellet med fem flytere er det funnet at jag har resonans ved $kR \simeq 5$. Dette antas å skyldes strukturelle interaksjoner mellom flyterne, gjennom de elastiske båndene. Analyse av hydrodynamiske interaksjoner for fem-flyter modell, uten elastiske bånd, viser en viss innflytelse i RAO, sammenlignet med teori. Det kan dog, ikke alene forklare avviket sett i eksperimentene.

Dessverre viser det seg at modellen har en uløst feil i koden. Utallige forsøk har blitt gjort, men uten hell. Etter å nærmere undersøke effekten av feilen, stilles det spørsmål om hvorvidt modellen gir ikke-realistiske resultater. Feilen viser seg å være liten i resultatene, og det antas derfor at den numeriske modellen, til en viss grad, beskriver systemet tilfredsstillende.

For å konkludere viser implementeringen at den numeriske modellen har potensial. Modellen er blitt generalisert til å kunne ha et gitt antall flytere og elastiske bånd. Modellen viser indikasjon på å fange opp ulike fenomener som strukturell og hydrodynamisk interaksjon. Uavhengig av at koden inneholder en feil, er den et solid grunnlag for videre utvikling.

Table of Contents

Nomenclature

Acronyms

CO_2	Carbon dioxide
H/λ	Wave steepness [-]
N_{ramp}	Number of ramping periods
2D	Two-dimensional
3D	Three-dimensional
BVP	Boundary value problem
FFT	Fast Fourier Transform
FK	Froude-Kriloff
ODE	Ordinary Differential Equation
RAO	Response Amplitude Operator
ZFT	Zero Frequency Theory

Greek Letters

β	Radial position of node on torus [rad]
η_2	Surge motion [m]
λ	Wave length [m]
ω	Wave frequency [rad/s]
ϕ	General velocity potential

ϕ^F	Far-field description velocity potential
ϕ^N	Near-field description velocity potential
ϕ_I^F	Inner expansion of far-field velocity potential
ρ	Fluid density (Sea water $[\mathrm{kg}/\mathrm{m}^3]$
ζ_a	Incident Wave Amplitude [m]

Roman Letters

$\ddot{v}$	Radial Floater Acceleration $[\mathrm{m}/\mathrm{s}^2]$
$\ddot{w}$	Vertical Floater Acceleration $[\mathrm{m}/\mathrm{s}^2]$
$\mathbf{a}$	Nodal Acceleration $[\mathrm{m}/\mathrm{s}^2]$
$\mathbf{s_k}$	Tangential Unit Vector of Truss
$\mathbf{v}$	Nodal Velocity [m/s]
$\mathbf{x}$	Nodal Position [m]
A_{11}	Added mass in surge
a_{33}^n	Vertical added mass for mode n
a_n	Vertical Modal Amplitude of Mode n [m]
a_{rr}^n	Radial added mass
b_n	Radial Modal Amplitude of Mode n [m]
c	Cross-sectional Radius of Torus [m]
EI	Bending Stiffness [MPa]
g	Gravitational acceleration $[\mathrm{m}/\mathrm{s}^2$
k	Wave Number [1/m]
k_m	Mooring-line Spring Stiffness [N/m]
k_t	Elastic-band Truss Spring Stiffness [N/m]
kR	Non-dimensional wave number, k multiplied by radius R of torus [-]
l_m	Mooring-line Length [m]
l_t	Elastic-band truss length [m]
M	Total mass of floater [kg]
m	Mass per unit length [kg/m]
$m_{i,j}$	Mass of truss node [kg]
n	Index used for mode number

R	Radius of lfoater [m]
T_p	Pre-tension [N]
T_w	Wave Period [s]
v	Radial Floater Motion [m]
w	Vertical Floater Motion [m]

Chapter 1

Introduction

Energy has over the centuries become more and more vital for the human population, and is part of almost all of our daily routines. In Norway, we found our first oil in 1967, which would later define us as one of the world's largest energy exporters IEA (2019b). With the development of the electric network, sources like nuclear-, wind- and solar energy have gained a global position as energy sources.

Increase in the global population, and new technology, the global energy demand is expected to continue to increase at a high pace. International Energy Agency IEA (2019a) states that in 2018 the Total Global Primary Energy Demand(TGPD) was 14 301 Mtoe (Million tonnes oil equivalent). If the TGPD is to have an average annual increase of about 1.2%, TGPD would in 2035 be around 17 812 Mtoe. Hence, there would be a significant gap in the energy demand that needs to be filled.

Limiting the global warming to below 2°C, which is the goal set by the Paris Agreement of the United Nations Framework on Climate Change FCCC (2016), will require a massive reduction of the greenhouse gasses. Among these is carbon dioxide, the main focus. Today's challenge consists of reassuring that the energy sources have low carbon emissions, and at the same time meet the future TGPD.

A postulated alternative is renewable CO_2 recycling in order to create synthetic fuel, Bruce et al. (2019). The idea is to look towards the marine environment and use the ocean as a medium for CO_2 extraction. Floating platforms are equipped with solar photovoltaic (PV) panels and generate the required energy for the CO_2 extraction and production of methanol at a production facility.

In order to realise such a vision, cheap, but robust marine platforms must be constructed. Locating this in the marine environment requires a thorough analysis. This masters thesis will focus on the platform that is to be designed.

The proposed structure is a multi-torus, composed of several single elastic concentric cylinders, similar to the ones used in aquaculture cages for fish farms. The individual tori are connected and moored by the use of elastic bands and mooring-lines. These are tension systems not able to take compression. There already exist studies on similar concepts and different derived theories. A summary of different contributions within this concept is given as part of previous studies below.

1.1 Previous studies

A considerable amount of literature has, over the years, been published on elastic circular collar often used as floating fish farms, also known as a torus. Most of the theories developed concerns slender body semi-submerged single-torus.

O. M. Faltinsen (2011) studied the wave-induced loads on a circular floater, also looking at the effect of including two floaters. Using linear slender body theory in deep water, he found asymptotic values to account for 3D added mass effects when $\omega \to 0$. He derived the theory, also referred to as the Zero-frequency-theory (ZFT). Later Li et al. (2012) developed the low-frequency slender-body theory (LFT) being a more complex and accurate theory for vertical added mass, damping and wave excitation loads. Both theories are based on a matched asymptotic expansion between a far-field potential and a near-field potential.

Regarding trusses, Marichal (2003) was first to introduce the theory and method for implementing numerical analysis on a cod-end using elastic trusses as net. It was later modified, further derived and presented by Kristiansen et al. (2014).

Two master students have already conducted experiments on the multi-torus concept. Windsvold (2018) performed an experiment in regular and irregular sea state for the multi-torus without the deck intended as support for the solar panels. He concluded that slamming and over-topping were not significant for the tested sea-conditions. From experiments of the response of the multi-torus, he observed the response to deviate from the proposed ZFT. He proposed that there could be structural interactions between the tori as they were connected. He concluded that the experiment had shown potential, but further work had to be done.

Sigstad (2019) continued the work of Windsvold and included a membrane on the top deck of the multi-torus. Weights were added to the membrane in order to simulate the weight of the deck supporting the solar panels. The results were promising, indicating that the multi-torus were able to follow the waves for several sea-conditions, but some over-topping and slamming-like wave motions were observed. The same results regarding the deviation in response compared to ZFT were observed. She also implemented a numerical code for simulating the response on a single torus floater coupled with trusses. The code did not work as intended and gave unsatisfactory results. She concluded that further work in developing a numerical code for response analysis for the multi-torus should be addressed. This will be the primary goal of this master's thesis.

1.2 Scope and objectives

This master thesis explores the hydro-elastic response of a multi-torus floater, being a structure consisting of five elastic concentric circular cylinders. These are attached to each another by elastic bands or *trusses*. A single floater will in this paper be referred to as a *single-torus* or *torus*, compared to *multi-torus* or *tori*.

The specific objective of this thesis is to develop a code in MATLAB to model a full solar island model, similar to the one used in the experiments mentioned above. Being able to analyse the model numerically is an essential step towards realising the concept as it allows fast computation and several cases, with different configurations, to be tested. These results are compared with experimental data already performed. The project will consist of modelling a multi-torus connected and moored by trusses. Here fundamental knowledge about hydrodynamics and mechanics are needed.

The thesis is a continuation of the preliminary study done as part of the project thesis from August to December 2019. The goal is to contribute with new knowledge considering the behaviour of a multi-torus concept. As a summary, the main objectives of this master's are given below:

1. Present previous research relevant to the thesis.
2. Read upon, and give an overview of relevant theory needed for the numerical implementation.
3. Conduct verification studies of a single-torus alongside the implementation process of the multi-torus model.
4. Finalise the numerical model for the multi-torus and compare with experimental results.
5. Analyse results and try to identify physical phenomena like structural interactions and hydrodynamic interactions.

1.3 Limitations

The scope of the masters is limited to study the behaviour of the multi-tours in regular waves. The numerical model will, in some cases, be compared with the experimental studies to evaluate and investigate the results. The theory uses potential theory, and all non-linear effects are neglected.

Due to the complexity of the multi-torus, the motion of the floater is limited to vertical- and horizontal motions. Sway is assumed to be negligible and is not accounted for. Current is not considered. Implementation of the coupled floater-truss code is first done with a single-torus model with and without mooring lines and is used as a verification of the code and theory.

With the *COVID-19* outbreak, the process has been more difficult. Thus, the results have been limited to only two different multi-torus concepts, with single truss connections.

1.4 Approach to problem

During the semester, the goal has been to model a full solar island model numerically. The approach has been to divide the system into several parts in order to isolate each problem separately. These can be summarised as,

1. The first part was to find and gather theory in order to obtain a numerical representation of a single-torus model, as a flexible beam, with mooring-lines modelled as trusses. The truss model was already established during the project thesis.
2. To verify the single-torus model, it was decided to only model one motion at a time. These were vertical-, surge- and radial motion.
3. With a satisfying verification study, further development of the numerical code will be to define a multi-torus model.
4. Due to the limited amount of time, few cases were conducted with the multi-torus model.
5. The results from the model have been compared to previous experiments in order to investigate physical phenomena.

1.5 Outline of Project Thesis

Chapter 2 presents the main theories regarding the truss model and the solar island model. The theories are further derived in order to be implemented numerically. Some theory has been further modified for numerical purpose.

Chapter 3 presents theory on hydrodynamic interaction, using the far-field approach. Based on an unpublished (2020) paper by supervisor Prof. Kristiansen.

Chapter 4 includes the verification studies done throughout the semester. The procedure of verifying the coupled single-torus model is presented. Finally, a verification study on hydrodynamic interaction is presented. Discussion of verification results are presented successively.

Chapter 5 presents the results for the final multi-torus, full solar island model. Trusses are included. Different configurations are tested. Hydrodynamic interactions are tested for a full solar island model, not considering elastic bands connecting the tori. All results are discussed successively. A summary of experimental results performed by Sigstad (2019) and Windsvold et al. (2019) are presented.

Chapter 6 concludes the study done in this project and suggests further work.

Appendix A presents additional derived theory. These being a derivation of truss equation and near-field approach of hydrodynamic interaction between bodies. The latter being based on an unpublished (2020) paper by supervisor Prof. Kristiansen.

Appendix B presents the verification study for truss model with results.

Appendix C presents the RAO from the verification studies for the vertical- surge- and radial motions, with different damping.

Appendix D presents new results from the full solar island model. Snapshots from the behaviour of the floater found with the numerical model are given.

Appendix E presents results from lab test of elastic bands.

Chapter 2

Solar Island Model: Theory

In this chapter, relevant theory needed for the numerical implementation of a combined floater-truss model is given. The derivation of the truss equation is given for elastic trusses, originated from Marichal (2003). Further, a description of the linear wave theory and modal analysis, are given as a foundation to understand the physical behaviour of the floater model, as well as the assumption made. The zero-frequency theory (ZFT) is described based on O. M. Faltinsen (2011). A procedure of coupling the truss model with the floater model is thoroughly described, inspired by the unpublished paper of supervisor Kristiansen (2012).

2.1 Truss-model

A truss is a tension system with direct analogy to chains, wires and tread. It is used in various industries as tension carriers. For offshore applications, mooring lines and fish-nets are the best examples. For the thesis, the numerical model focus on implementing the truss model to be used as a key component when studying the floating solar island.

The truss model was first proposed by Marichal (2003) in a numerical study of a cod-end. Kristiansen et al. (2014) has later modified this with their work on aquaculture fish-net. In this thesis, the latter model is implemented. A numerical model is used to calculate the tensions in the trusses for different time step. The model makes it possible to find the displacement of the truss in time. Trusses are defined by a line between two nodes, each with a three dimensional spatial coordinate $\{x, y, z\}$. Thus the system of trusses consist of $N_{nodes} = N_{truss} + 1$. The nodes are denoted i and j in figure 2.1, indicating the start and end node, respectively.

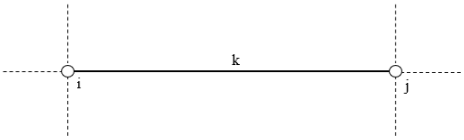

Figure 2.1: Definition of truss k with corresponding nodes i and j

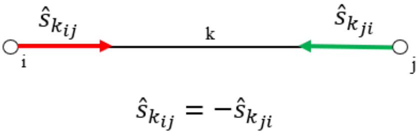

Figure 2.2: Direction and notation of the tangential unit vectors on truss k

Deriving the mechanical equations for a system of trusses, it is interesting to first look at the fundamental principle of the dynamics, i.e. Newton's second law. We have

$$m\ddot{\mathbf{x}}(t) = \sum F_{ex} \tag{2.1}$$

where $\ddot{\mathbf{x}}(t)$ is the nodal acceleration $\mathbf{a}(t)$, m is the mass of the truss and $\mathbf{F}_{ex}$ are external forces.

The external forces are further divided into tensions and gravitational forces.

$$m\ddot{\mathbf{x}}(t) = m\mathbf{g} + \sum T_k \mathbf{s}_k \tag{2.2}$$

Here $\mathbf{g}$ is the gravitational acceleration vector, T_k is the truss tension and $\mathbf{s}_k$ is the three-dimensional tangential unit vector of the truss, given by

$$\mathbf{s}_k = \frac{(\mathbf{x}_j - \mathbf{x}_i)}{||(\mathbf{x}_j - \mathbf{x}_i)||} \tag{2.3}$$

This is a second-order ordinary differential equation (ODE). With some algebraic manipulations, this can be expressed in terms of a first-order ODE. Observing that the nodal velocity can be expressed as $\dot{\mathbf{x}} = \mathbf{v}$, and thus $\dot{\mathbf{v}} = \mathbf{a}$ and $\dot{\mathbf{x}} = \mathbf{u}$. We can expressed them by the use of a time integration scheme.

2.2 Time integration scheme

For time-dependent problems, analytical solutions are usually not possible as the systems are rather complex. Numerical methods are then used. To be able to solve a system of equations over a time series numerically, the use of a time integration scheme is necessary. Several time-integration scheme exists, and among these, the implicit and explicit Euler method are widely used. In this section, these two schemes are presented.

Assuming that the time step $\Delta t > 0$ & $\Delta t << 1$ the expression for time derivative can be simplified to

$$\dot{y}^n \approx \frac{y^{n+1} - y^n}{\Delta t} \tag{2.4}$$

where $\dot{y}^n$ is the time derivative of y^n, and y^{n+1} is the value of y at the next time instant $n+1$. This can further be rearranged and expressed in terms of y^{n+1}.

$$y^{n+1} = y^n + \Delta t \dot{y}^n \tag{2.5}$$

From equation (2.5) the information at the next time step can be expressed by information from the present time step.

Another way of obtaining this information is by using the time derivative of the next time step. This is the implicit time scheme.

$$y^{n+1} = y^n + \Delta t \dot{y}^{n+1} \tag{2.6}$$

Equation (2.5) and equation (2.6) will be combined in order to solve the nodal position of the trusses. Expressing the nodal position in terms of equation (2.6) we get.

$$\mathbf{x}^{n+1} = \mathbf{x}^n + \Delta t \mathbf{v}^{n+1} \tag{2.7}$$

It can by this be understood that the nodal position at time instant $n+1$ is dependent on the velocity at the same time instant. This is thus an implicit expression, and is challenging to solve numerically.

The velocity in the next time step is solved explicitly by equation (2.5) and remembering $\dot{\mathbf{v}} = \mathbf{a}$ and $\ddot{\mathbf{x}} = \mathbf{a}$. The implicit scheme in equation (2.7) can be combined with the explicit expression for the velocity. Thus the implicit nodal positions at the next time step can be expressed explicitly, making it much more practical to solve. The final expression, including equation (2.2) is given in the fourth line of equation (2.8).

$$\begin{aligned}
\mathbf{v}^{n+1} &= \mathbf{v}^n + \Delta t \mathbf{a}^n \\
\mathbf{x}^{n+1} &= \mathbf{x}^n + \Delta t \mathbf{v}^{n+1} \\
\mathbf{x}^{n+1} &= \mathbf{x}^n + \Delta t (\mathbf{v}^n + \Delta t \mathbf{a}^n) \\
\mathbf{x}^{n+1} &= \mathbf{x}^n + \Delta t \Big[\mathbf{v}^n + \Delta t \Big(\mathbf{g} + \frac{1}{m} \sum T_k^n \mathbf{s}_k^n \Big) \Big]
\end{aligned} \tag{2.8}$$

These equations are the bases of how to solve the time-dependent problem numerically.

2.2.1 Elastic compound truss

An elastic compound truss is a truss which includes elasticity, meaning it can elongate. These properties are seen in rubber bands. In the marine environment, components like mooring lines can be thought of as a chain of elastic trusses. An expansion from the rigid truss system, presented in appendix A.1, to the elastic truss system is done. This is fairly simple and is derived from Hooke's law.

For an element with elastic properties and a cross-section, Young's modulus E and cross-sectional area A can be found. When subjected to positive tension, the element will increase its length linearly and be represented by Hooke's law in equation (2.9).

$$T = k\Delta l \tag{2.9}$$

where k is the spring constant of the truss given by $k = \frac{EA}{l_0}$.

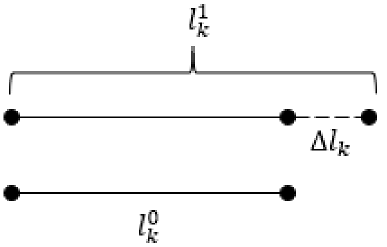

Figure 2.3: Direction and notation of the tangential unit vectors on truss k

From figure 2.3 it is evident that $\Delta l_k = l_k^1 - l_k^0$. This is understood as a pre-tension truss, where l_k^0 is the original length of the truss and l_k^1 is the pre-tension length. Using this relation and solving equation (2.9) the pre-tension is defined by.

$$T_p = k(l_k^1 - l_k^0) \tag{2.10}$$

This is understood as the first time instant of the behaviour of the system. The pre-tension will be an initial condition to the system and give its motions. Given the pre-tension, the geometrical- and material properties of the truss, the pre-tension truss length is found. Numerically the length of a truss is given by,

$$l_k = ||\mathbf{x}_j - \mathbf{x}_i|| \tag{2.11}$$

where **x** is the three-dimensional (3D) vector of the nodes.

When solving with respect to time, it is the incremental change in tension that is of interest, i.e. ΔT. Thus the reference tensions between time steps are T^n and T^{n-1} respectively.

Figure 2.4 show how the length at time step $n+1$ for an elastic truss can be found. Note that as for a rigid truss, the length for time step $n+1$ is found from the previous tension, i.e. T^n.

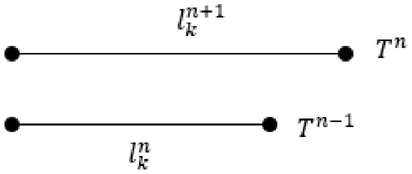

Figure 2.4: Direction and notation of the tangential unit vectors on truss k

Using equation (2.10) it is possible to find the tension at a given time step,

$$\begin{gathered}\Delta T^n = k\Delta l_k^n \\ \Updownarrow \\ (T^n - T^{n-1}) = k(l_k^{n+1} - l_k^n) \\ \Downarrow \\ l_k^{n+1} = l_k^n + \left(\frac{T^n - T^{n-1}}{k}\right)\end{gathered} \tag{2.12}$$

By squaring the absolute values of both sides of equation (2.12), the length of truss at time-step $n+1$ is expressed by,

$$||l_k^{n+1}||^2 - ||l_k^n||^2 = 2\frac{l_k^n(T^n - T^{n-1})}{k} + \mathcal{O}(\epsilon^2 << 1) \tag{2.13}$$

The left-hand side (LHS) is the expression for a rigid truss. We wish to express the length in terms of **x**, **v** and **a**. This is done by recalling equation (2.11), using change of variables, algebraic manipulation, and recalling the cosine formulae for vectors. A thorough derivation of this procedure is given in appendix A.1 for the description of a rigid truss. We then get the LHS of the equation to be,

$$\Delta t^2 \underbrace{||\mathbf{v}_j^n - \mathbf{v}_i^n||^2}_{\mathbf{b}^n} + 2\underbrace{(\mathbf{x}_j^n - \mathbf{x}_i^n)}_{l_k\mathbf{s}_k}(\Delta t \underbrace{(\mathbf{v}_j^n - \mathbf{v}_i^n)}_{\mathbf{c}^n} + \Delta t^2(\mathbf{a}_j^n - \mathbf{a}_i^n)) = 0 \tag{2.14}$$

where we have neglected any O(Δt). The system of equations for the elastic truss can be given.

$$\mathbf{s}_k \cdot (\mathbf{a}_j^n - \mathbf{a}_i^n) - \frac{T^n}{k\Delta t^2} = -\frac{\mathbf{b}^n}{2l_k} - \mathbf{s}_k \frac{\mathbf{c}^n}{\Delta t} - \frac{T^{n-1}}{k\Delta t^2} \tag{2.15}$$

Recall that the acceleration can be expressed in terms of gravity and tension.

$$\mathbf{a}_j = \frac{1}{m_j} \sum_l T_{jl} \mathbf{s}_{jl} + \mathbf{g} \tag{2.16}$$

Finally, equation (2.15) shows the relation between the unknown tension forces on the LHS and the motion of the system on the RHS. Thus, a system consisting of $N_{trusses}$ can be expressed by the linear system of equations **A***T*=*b*, where **A** is a $N_{truss} \times N_{truss}$ matrix and *T* and *b* are $N_{truss} \times 1$ vectors. As the tensions are the only unknown parameter at time step n, solving for *T* for time step n one can thus find the nodal position, velocity and acceleration at time step $n+1$. On matrix form we get, without the additional tension terms,

$$\mathbf{A} = \left[\begin{array}{c:c:c:c} -(\mathbf{s}_1 \cdot \mathbf{s}_1) \cdot A(1,1) & \frac{(\mathbf{s}_1 \cdot \mathbf{s}_2)}{m_2} & 0 & 0 \\ \hdashline \frac{(\mathbf{s}_2 \cdot \mathbf{s}_1)}{m_2} & -\mathbf{s}_2 \cdot \mathbf{s}_2 [\frac{1}{m_3} + \frac{1}{m_2}] & \frac{(\mathbf{s}_2 \cdot \mathbf{s}_3)}{m_3} & 0 \\ \hdashline 0 & \ddots & \ddots & \frac{(\mathbf{s}_{N-1} \cdot \mathbf{s}_N)}{m_N} \\ \hdashline 0 & 0 & \frac{(\mathbf{s}_N \cdot \mathbf{s}_{N-1})}{m_N} & -(\mathbf{s}_N \cdot \mathbf{s}_N) \cdot A(N,N) \end{array}\right] \tag{2.17}$$

$$b = \left[\begin{array}{c} -\frac{\mathbf{b}^n}{2l_1} - \mathbf{s}_{k,1} \frac{\mathbf{c}^n}{\Delta t} - \frac{T^{n-1}}{k\Delta t^2} + B(1,1) \\ \hdashline -\frac{\mathbf{b}^n}{2l_2} - \mathbf{s}_{k,2} \frac{\mathbf{c}^n}{\Delta t} - \frac{T^{n-1}}{k\Delta t^2} \\ \hdashline \ldots \\ \hdashline \ldots \\ \hdashline -\frac{\mathbf{b}^n}{2l_N} - \mathbf{s}_{k,N} \frac{\mathbf{c}^n}{\Delta t} - \frac{T^{n-1}}{k\Delta t^2} + B(N,N) \end{array}\right] \tag{2.18}$$

The additional terms $A(1,1)$, $A(N,N)$, $B(1,1)$ and $B(N,N)$ are variables determined by the boundary conditions for each case. A considers which nodes are to be taken into account when dividing by the masses, while b considers acceleration terms like gravity or external excitation to nodes.

The term considering T^n of equation (2.15) are included in the **A**-matrix in equation (2.17) for the diagonal terms only. The term T^{n-1} is kept on the RHS and included in *b*-vector in equation (2.18).

2.3 Linear wave theory

The physics of waves are, in reality, highly complex and nonlinear. To perform engineering tasks and analysis in such environments, we often use a linear theory of the waves. It gives sufficient accuracy for most problems and also makes it possible to estimate higher-order nonlinear. With the linear wave theory, we can derive statistical properties of regular and irregular sea-states. For this thesis it is nused with the assumption of deep water, and gathered from O. M Faltinsen (1990).

In the linear wave theory, we assume that the fluid is homogeneous, with horizontal fixed dept and the infinite extent of the free-surface. Further, we assume that the potential theory describes fluid motions. The potential theory states that the fluid is at all-time incompressible, irrotational and inviscid. With these assumptions, one can derive the free-surface conditions and the dispersion relation.

For the assumptions of an incompressible fluid, the Laplace equation give $\nabla \cdot \mathbf{V} = 0$, and the kinematic and dynamic conditions at the free-surface can be found to be respectively.

$$\frac{\partial \zeta}{\partial t} = \frac{\partial \phi}{\partial z}, \; on \; z = 0 \tag{2.19}$$

$$g\zeta + \frac{\partial \phi}{\partial t} = 0, \; on \; z = 0 \tag{2.20}$$

where ϕ is the velocity potential of the fluid, and ζ is the elevation of the free-surface. These are evaluated on the mean free-surface $z = 0$. For deep water these are described by equation (2.21) and equation (2.22) respectively.

$$\phi = \frac{g\zeta_a}{\omega} e^{kz} \cos(\omega t - kx) \tag{2.21}$$

$$\zeta = \zeta_a \sin(\omega t - kx) \tag{2.22}$$

Here ζ_a is the wave amplitude, i.e half the wave height $\zeta_a = H/2$. Finally, by combining equation (2.19) and equation (2.20) one can get the dispersion relation giving the connection between the wave frequency ω of the wave and its wave number k.

$$\omega^2 = kg \tag{2.23}$$

where ω and k are described as

$$\omega = \frac{2\pi}{T_w} \tag{2.24}$$

$$k = \frac{2\pi}{\lambda} \tag{2.25}$$

with T_w is the corresponding wave period and λ the wavelength. The wave steepness H/λ gives the ratio of the wave height and the wavelength. This factor is used later to model the waves.

For this thesis, all sea-states are based on properties according to the linear wave theory presented above, and being regular waves.

2.4 Zero Frequency Theory

The zero-frequency theory (ZFT) was developed and published by O. M. Faltinsen, 2011 to find the hydrodynamic loads on a slender circular collar for use in fish farms. This theory is the foundation when describing the vertical forces and motions acting on the structure. Later Kristiansen (2012) used this theory to couple the floater motion of a fish farm with mooring lines described by trusses. A so-called slender-body theory are derived based on a rigid free-surface condition. For this theory to be valid, the following assumptions are made.

- The wave lengths of interest are long relative to the cross-section, i.e $\lambda >> 2c$ with $2c$ being the cross-sectional diameter of a floater.
- The floater/tori is semi-submerged
- Potential flow theory with incompressible fluid is valid
- Deep water is considered, i.e the dispersion relation simplifies to $\omega^2 = kg$.
- Current loads are considered small and negligible.
- Linear hydrodynamic loads on floater.
- Vertical and lateral motions of floater are analyzed separately.

A slender-body theory is considered, stating that the radius of the circular centre-line R of the torus are large compared to the cross-sectional radius c. The vertical motion is described by the modal superposition as given in section 2.6. In order to satisfy the rigid-body conditions, one needs to consider the limiting case where $\omega \to 0$.

To obtain the hydrodynamic loads on the torus, one can express the system with a far-field description and a near-field description. A matched asymptotic expansion is required to obtain a constant that gives a unique solution. O. M. Faltinsen (2011) explains that for a two-dimensional solution, using a classical frequency-domain free-surface condition, the constant we are seeking will go to infinity as $\omega \to 0$. This leads to an infinite 2D added mass for the vertical modes, which is not physical.

For the far-field and the near-field description, a set of coordinate systems are used. These can be seen in figure 2.5

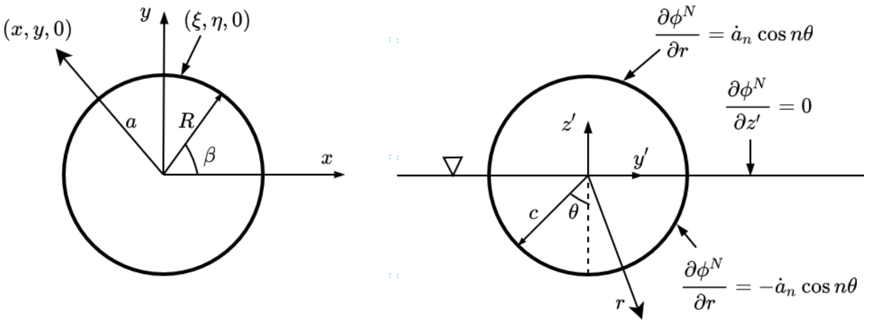

(a) Far-field illustration **(b)** Near-field illustration

Figure 2.5: Illustration of the far-field and near-field description. The illustrations are inspired by O. M. Faltinsen (2011)

Far-field description

In a far-field description of a circular floater, the cross-sectional details are not seen. A point on the floater is given by $(\xi, \eta, 0)$ with a distance R to the centre-line. A field point with distance a has the coordinates $(x, y, 0)$. With a zero frequency wave, the floater acts as a being a line distribution of sources with the strength Q. The velocity potential can thus be described as a 3D source along a circle. An inner expansion of the far-field description is found for the limiting case $r \to 0$, where $r = \sqrt{(a - R)^2}$.

$$\phi^F = \frac{QR}{4\pi} \int_0^{2\pi} \frac{1}{r} d\beta, \qquad r \to 0 \qquad \Rightarrow \phi_I^F = \frac{Q}{2\pi} \log\left(\frac{8R}{r}\right) \tag{2.26}$$

Near-field description

In the near-field description the cross-sectional dimension of the semi-submerged floater is seen. The cross-sectional radius is c. The local polar coordinate (r, θ) is related to a Cartesian coordinate (y', z') by $y' = r\sin(\theta), z' = r\cos(\theta)$. $\theta = 0$ is defined at the negative z'-axis. From figure 2.5b the cross-section of the torus moves with a vertical velocity $\dot{a}_n \cos(n\beta)$. Imaging the semi-circle about the free-surface ($z = 0$), the rigid free-surface condition is satisfied. The near field solution of the velocity potential can be expressed by

$$\phi^N = \dot{a}_n \cos(n\theta)\Big[C \log\Big(\frac{r}{R}\Big) + A_0 + \sum_{n=1}^{\infty} A_n \frac{\cos(n\theta)}{r^n}\Big] \tag{2.27}$$

The constants C, A_0 and A_n are needed. We find A_0 from the matching of the far-field and near-field descriptions. The matching is done for the limiting case where $\phi^N(r \to \infty) = \phi_I^F$. This gives $A_0 = -C\log(8)$. C is further found by solving the boundary value problem (BVP) on the surface of the forced moving body. Lastly A_n is found by substituting equation (2.27) into the BVP, multiplying by $cos(m\theta)$ for $m \geq 1$ and integrating from 0 to 2π.

2.5 RAO

A response amplitude operator (RAO) is of great interest when designing structures. It allows us to get an insight into the expected response of the structure when excited to harmonic loads at different frequencies. The theoretical RAO for the vertical modes are defined by the ZFT described above. For each mode, an RAO is found. Simply put, the RAO is defined as the absolute value of the ratio between the amplitude motion and the incident wave amplitude. The vertical RAO and the lateral RAO with surge will be given, and is later be used to compare results with theory.

Vertical RAO

In order to find the vertical RAO, the equation of motion of the floater must be solved. Assuming zero damping, the equation of motion for a given mode is found from equation (2.45). Neglecting truss forces and assuming the modal amplitude to be of harmonic nature, i.e $a_n(t) = a_{n,a}e^{(-i\omega t)}$. The time-dependent term disappears, and the vertical RAO is given by

$$\left|\frac{a_{n,a}}{\zeta_a}\right| = \left|\frac{(3-\alpha_n)(\rho g b_w - \omega^2 a_{33}^n) i^{n+1} J_n(kR)}{-(m + a_{33}^n)\omega^2 + \rho g b_w + \frac{EI}{R^4}(n^4 - n^2)}\right|, \qquad n \geq 0 \tag{2.28}$$

with $\alpha_n = 2$ for heave and $\alpha_n = 1$ for higher modes. It is important to stress that for, e.g. $n = 1$ being pitch, it is a definition of the pitch mode response rather than the actual pitch angle.

Surge and lateral RAO

As the rigid-body motion of surge needs to be treated in a separate manner. Solving equation (2.60) and equation (2.68), the RAOs are found to be

$$\left|\frac{b_{1,a}}{\zeta_a}\right| = \left|\frac{2\pi R a_{rr}[J_0(kR) - J_2(kR)]}{-(M + A_{22})}\right|, \qquad n = 1 \tag{2.29}$$

for surge, and for lateral we get

$$\left|\frac{b_{n,a}}{\zeta_a}\right| = \left|\frac{2a_{rr}^n \omega^2 i^{n-1}[J_{n-1}[(kR) - J_{n+1}(kR)]}{-(m + a_{rr}^n)\omega^2 + \frac{EI}{R^4}(n^4 - n^2)}\right|, \qquad n \geq 2 \tag{2.30}$$

2.6 Modal analysis

Studying dynamic behaviour of a structure when exposed to external loading is of great interest for most ocean engineering problems. Numerically, it is quite hard as it requires knowledge about the loading and a way of predicting its, usually quite complex, response. For structures, the modal analysis uses the mass and stiffness of the system to find at which frequencies the system resonate with a given shape. Knowing the shapes, a total response of a structure can be approximated by a superposition of all these with their respective magnitude.

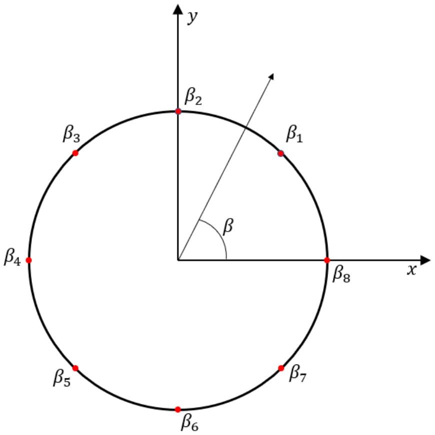

Figure 2.6: Bird view: Illustration of points(red) on the floater at which the response is found

In this masters thesis, modal analysis is used to model the behaviour of the circular floater. The response of a point m at the floater at a time instant t is found from a superposition of n modes, which is made up of a cosine function and a time-dependent modal amplitude.

2.6.1 Vertical modes

For a vertical motion, this is given by

$$w_n(\beta_n, t) = a_0(t) + \sum_{n=1}^{\infty} a_n(t)\cos(n\beta_n) \tag{2.31}$$

where β_n denotes the position on the floater at point n and a_n is its amplitude. Figure 2.7 is an illustration of the physical description of the first four vertical modal shapes of the floater. $n = 0$ is heave, $n = 1$ is pitch and $n = 2$ and $n = 3$ is known as the first- and second flexible respectively. The higher modes are a further development of the flexible modes.

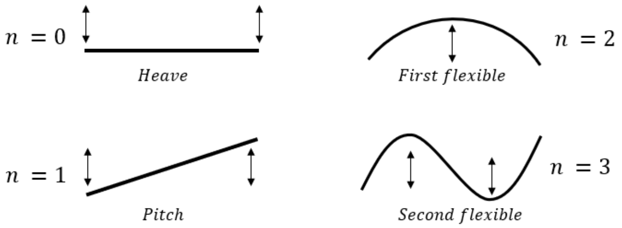

Figure 2.7: Side view: Illustration of the first four vertical modal shapes of floater

2.6.2 Horizontal modes

The horizontal modes are described in a similar manner,

$$v_n(\beta_n, t) = \sum_{n=1}^{\infty} b_n(t)\cos(n\beta_n) \tag{2.32}$$

Mode $n = 0$ is excluded. It describes the floater uniformly expanding or contracting in the radial direction. With a rigid floater, this is considered as a non-physical behaviour. Mode $n = 1$ describes the rigid-body mode surge and will be treated separately. This will be described in further detail in section 2.8. The higher modes are elastic modes, and is described as ovalising modes.

For the radial motion of the floater gives a time-varying x- and y-motion. At a given position at the floater, β_m, the x- and y-position can be described by

$$x_m(\beta_m, t) = \eta_1(t)\cos(\theta) + v(\beta_m, t)\cos(\beta_m - \theta) \tag{2.33}$$

$$y_m(\beta_m, t) = \eta_2(t)\sin(\theta) + v(\beta_m, t)\sin(\beta_m - \theta) \tag{2.34}$$

where θ is the wave direction, chosen to be $\theta = 0$. With η_1 being the rigid-body motion surge and η_2 is sway. The position at each point m along the floater can be found for a known $v(\beta_m, t)$.

2.7 Copuled Model for Single Floater Vertical Motion

The vertical motion *w* of a single torus is found from the generalised Euler-Bernoulli beam equation. The curvature and flexibility is taken into account and is described in P. Li (2017) as

$$m\frac{\partial^2 w}{\partial t^2} + \rho g b_w + EI\frac{\partial^4 w}{\partial s^4} + \frac{EI}{R^2}\frac{\partial^2 w}{\partial s^2} - \frac{\partial}{\partial s}\Big(T_{as}\frac{\partial w}{\partial s}\Big) = f_3(s,t) \tag{2.35}$$

Here m is the floater mass per unit length found from assumption of semi-submerged cylinder. b_w is $2c$, the cross-sectional diameter of the floater when semi-submerged. R is the radius of the circular centre-line curve of the torus. Further EI is the bending stiffness of the floater, whereas the first EI-term considers the curvature of the beam and with the second EI-term represents a rigid torus with $EI \rightarrow \infty$. The latter term on the LHS considers the axial stiffness of the floater and will not be included in our model.

For the RHS, $f_3(s,t) = f_3(s)^{added\ mass} + f_3(s)^{wave\ excit} + f_3^{trusses}$, where $f_3^{added\ mass}$ considers the added mass per unit length of the floater, $f_3^{wave\ excit}$ is the vertical wave excitation force per unit length of the floater. Finally $f_3^{trusses}$ is the tension forces from the mooring lines and the elastics that work as connectors between each floater. Both, the mooring lines and elastics are represented by trusses and described by the elastic truss equation, derived in section 2.2.1.

2.7.1 Vertical modal equation of model

The floater is symmetric about the x- and y-axis, with a wave propagating in the positive x-direction. Thus the vertical motion of the floater can be expressed in terms of a Fourier series. For a linear approximation, the sum of all modes give the exact response. This is referred to as modal superposition.

Using modal superposition, the vertical motion of the floater can be represented by a sum of vertical modal components. a_n given by t and β as shown in equation (2.31).

The vertical elastic response of the floater is found by inserting equation (2.31) into equation (2.35) and using the fact $\partial/\partial s = R^{-1}\partial/\partial\beta$. Using the orthogonality principle, the resulting equation is multiplied equation (2.35) with $\cos(m\beta)$ and integrated from $\beta = 0$ to 2π. The equation becomes

$$m\ddot{a}_n + \Big(\rho g b_w + (n^4 - n^2)\frac{EI}{R^2}\Big)a_n = \frac{1}{\alpha_n \pi}\int_0^{2\pi} f_3(s,t)\cos(m\beta)d\beta\Big) \tag{2.36}$$

Here $\alpha_n = 2$ for $n = 0$ and $\alpha_n = 1$ for $n \geq 1$. The last integral gives us the generalized added mass and wave excitation force, as well as the tensions from the mooring lines. A short description of the forces is given below.

2.7.2 Vertical added mass force

The added mass for a body is found from the integration of the dynamic pressure, $p = -\rho \partial \phi^N / \partial t$, multiplied with normal vector over the submerged part of the body. The expression for a 2D vertical added mass is given in O. M. Faltinsen (2011) as

$$a_{33}^n = 2\rho c^2 \left\{ \frac{2}{\pi} \Big[\log\Big(\frac{8R}{c}\Big) - K_n \Big] + \gamma \right\} \tag{2.37}$$

where $\gamma = 0.07238725793$.

The coefficient K_n comes from the inner expansion of the far-field description, given analytically for any n by (Timokha, 2010) from O. M. Faltinsen (2010) as

$$K_n = \frac{1}{2\sqrt{2}} \int_0^{2\pi} \frac{1 - \cos nx}{\sqrt{1 - \cos x}} dx \tag{2.38}$$

Finally, the added mass force of the torus can be expressed and included into the equation of motion of the floater. The added mass force per unit length of the torus is given by $f_3^{added\ mass} = a_{33}^n \ddot{a}_n$. Moved over to the left side the wave excitation force and mooring line tensions are the ones needed to be found. The equation of motion is

$$(m - a_{33}^n)\ddot{a}_n + \Big(\rho g b_w + (n^4 - n^2)\frac{EI}{R^2}\Big) a_n = \frac{1}{\alpha_n \pi} \int_0^{2\pi} (f_3^{wave\ excit} + f_3^{trusses}) \cos(m\beta) d\beta\Big) \tag{2.39}$$

2.7.3 Vertical wave excitation force

The vertical wave excitation force is divided into Froude-Kriloff forces and diffraction forces. O. M. Faltinsen (2010) expresses these as

$$f_3^{FK} = \rho g \zeta_a i \big[J_0(kR) + \sum_{n=1}^{\infty} 2 i^n J_n(kR) \cos(n\beta) \big] b_w e^{(-i\omega t)} \tag{2.40}$$

$$f_3^D = -i\omega^2 \zeta_a \big[J_0(kR) a_{33}^0 + \sum_{n=1}^{\infty} 2 i^n J_n(kR) a_{33}^n \cos(m\beta) \big] e^{(-i\omega t)} \tag{2.41}$$

Where $J_n(kR)$ referrers to the Bessel function of first kind for mode n. Multiplying equation (2.42) and equation (2.43) by $\cos n\beta$, integrating from $\beta = 0$ to 2π, and taking its real part the equations becomes.

$$F_{3n}^{FK} = \rho g b_w \zeta_a (3 - \alpha_n) J_n(kR) \operatorname{Re}(i^{n+1} e^{(-i\omega t)}) \tag{2.42}$$

$$F_{3n}^{D} = -\omega^2 a_{33}^{n} \zeta_a (3 - \alpha_n) J_n(kR)\,\mathrm{Re}(i^{n+1} e^{(-i\omega t)}) \tag{2.43}$$

Adding equation (2.42) and equation (2.43) we get the generalized vertical wave excitation forces on the floater.

$$F_{3n}^{wave\ excit} = (\rho g b_w - \omega^2 a_{33}^{n}) \zeta_a (3 - \alpha_n) J_n(kR)\,\mathrm{Re}(i^{n+1} e^{(-i\omega t)}) \tag{2.44}$$

Included into equation (2.39), we get the updatet equation of motion

$$(m + a_{33}^{n})\ddot{a}_n + \left(\rho g b_w + (n^4 - n^2)\frac{EI}{R^2}\right) a_n = F_{3n}^{ex} + \frac{1}{\alpha \pi} \int_0^{2\pi} f_3^{truss} \cos(n\beta) d\beta \tag{2.45}$$

Finally, the mooring line forces from the trusses need to be developed. The truss equation have already been developed based on Marichal (2003). This is further used for including the floater motion into the truss equation.

2.7.4 Coupling of floater and truss: Vertical

When coupling the truss model to the floater numerically, a matching of properties must be done. The matching considers the acceleration of the truss node connected to the floater to include the floater acceleration. These trusses will later be referred to as *mooring-truss* or *floater-truss*, based on whether the trusses are used as mooring lines or as connections between tori. Later, when including multiple tori, the connection elastics between the tori are illustrated as being composed of *floater-truss* and *connective truss*. Note that hydrodynamic forces included for the trusses are neglected in the present case. A simplified illustration of the system with two tori is given in figure 2.8.

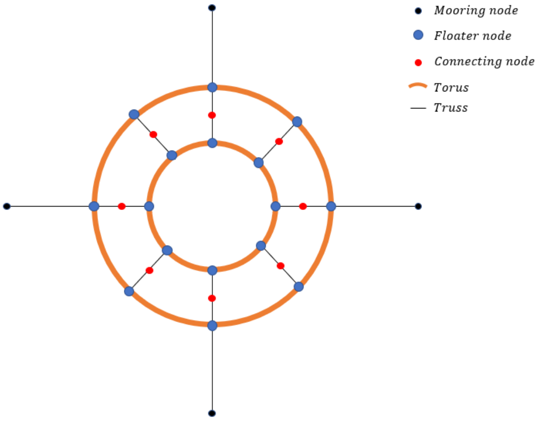

Figure 2.8: Illustration of a possible multi-torus configuration with connected trusses

Since it is the acceleration term that connect the truss and floater equations in the numerical scheme, it is necessary to express the vertical floater acceleration in terms of modal acceleration. Considering that the truss connected to the floater has the indices q, the acceleration of the floater at node q is expressed by a summation of all modes for node q.

$$\ddot{w}_q(\beta_q, t) = \sum_{n=0}^{\infty} \ddot{a}_{n,q}(t) \cos(n\beta_q) \tag{2.46}$$

Expressing $\ddot{a}_{nq}$ in terms of equation (2.45), $\ddot{w}_q$ is now given by.

$$\ddot{w}_q = \sum_{n=0}^{\infty} \left\{ \frac{1}{(m + a_{33}^n)} \left[F_{3n}^{ex} - \left(\rho g b_w + (n^4 - n^2) \frac{EI}{R^2} \right) a_n + \int_0^{2\pi} f_3^{truss} \cos(n\beta) d\beta \right] \cos(n\beta_q) \right\} \tag{2.47}$$

Now, looking at the last term, the integral gives the forces of the truss connected to the floater. This integral is difficult to find analytically. Instead, assuming that each node at the floater covers an equal portion of the floater, it is possible to simplify this integral by taking the sum of all forces at each node. Note that for two or more tori, some floater nodes will have two trusses connected. From this, one can understand that it is necessary to account for the node being the i or j node of a truss. This will indicate whether the force is acting in a positive- or negative direction, with respect to the truss. To account for this, γ_{ft} have been created to give 1 for i nodes and -1 for j nodes. Noting that the vertical motion can be expressed by $w = \vec{x} \cdot \vec{k}$, the following equation for the forces related to the truss tensions are given.

$$\begin{aligned} \int_0^{2\pi} f_3^{truss} \cos(n\theta) d\theta &\simeq \sum_{ft=1}^{N_{ft}} f_{3ft}^{truss} \cos(n\theta) \Delta\theta \\ &= \frac{1}{\Delta s} \sum_{ft=1}^{N_{ft}} \Big(\gamma_{ft} T_{ft} (\mathbf{s}_{ft} \cdot \mathbf{k}) \Big) \cos(n\theta_{ft}) \Delta\theta \\ &= \frac{1}{R} \sum_{ft=1}^{N_{ft}} \Big(\gamma_{ft} T_k (\mathbf{s}_{ft} \cdot \mathbf{k}) \Big) \cos(n\theta_{ft}) \end{aligned} \tag{2.48}$$

where $\theta_{ft} = 2\pi k / N_{ft}$ is the angle between the trusses connected along the floater, and the last equality is obtained by noting that $\Delta s = R\Delta\theta$ is the part of the floater one truss acts upon. N_{ft} is the number of floater trusses connected along the floater. An illustration to show the idea of how the truss forces on the floater are found, is seen in figure 2.9.

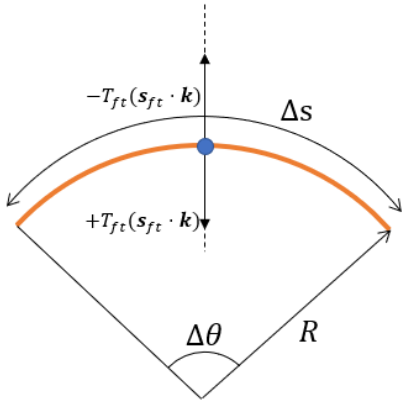

Figure 2.9: Illustration of a floater section. Forces acting on a floater node with one or two trusses connected. It is shown for the vertical component, but the same idea holds for the radial motion, only then considering radial components.

The acceleration of a floater node can be expressed as

$$\begin{aligned}\ddot{w}_q = &\underbrace{\sum_{n=0}^{\infty}\left\{\frac{\cos(n\beta_q)}{\alpha_n\pi R(m+a_{33}^n)}\sum_{ft=1}^{N_{ft}}\Big(\gamma_{ft}T_k(\mathbf{s}_{ft}\cdot\mathbf{k})\Big)\cos(n\theta_{ft})\right\}}_{\ddot{w}_{q,T}}\\ &+\underbrace{\sum_{n=1}^{\infty}\left\{\frac{\cos(n\beta_q)}{(m+a_{33}^n)}\Big[F_{3n}^{exc}-(\rho g b_w+(n^4-n^2)\frac{EI}{R^2})\Big]a_n\right\}}_{\ddot{w}_{q,rest}}\end{aligned} \tag{2.49}$$

where tension relateds part are found in $\ddot{w}_{q,T}$, while the dynamic behaviour is placed in $\ddot{w}_{q,rest}$. The floater node can now be included into the truss model. First the floater node acceleration is made three-dimensional by multiplying with the vertical unit vector $\mathbf{k} = [0, 0, 1]$. Secondly it is inserted as an acceleration $\mathbf{a}_q$ of equation (2.15) being either an i or j-node. Equation (2.50) and equation (2.51) shows the resulting combined equation for the case of a floater node q being an i-node or j-node, respectively.

$$\mathbf{s}_k\cdot(\ddot{w}_{q,T}^n\cdot\mathbf{k}-\mathbf{a}_i^n)+\frac{T^n}{k\Delta t^2}=-\frac{b^n}{2l_k}-\mathbf{s}_k\Big(\frac{\mathbf{c}^n}{\Delta t}-\ddot{w}_{q,rest}^n\cdot\mathbf{k}\Big)-\frac{T^{n-1}}{k\Delta t^2} \tag{2.50}$$

$$\mathbf{s}_k\cdot(\mathbf{a}_j^n-\ddot{w}_{q,T}^n\cdot\mathbf{k})+\frac{T^n}{k\Delta t^2}=-\frac{b^n}{2l_k}-\mathbf{s}_k\Big(\frac{\mathbf{c}^n}{\Delta t}+\ddot{w}_{q,rest}^n\cdot\mathbf{k}\Big)-\frac{T^{n-1}}{k\Delta t^2} \tag{2.51}$$

These are then arranged into the system of equation $\mathbf{A} \cdot T = b$, where all unknown tension related terms are found on the LHS and the others are on the RHS.

2.8 Coupled Model for Single Floater Radial Motion

The vertical motions for a single floater have been described as well as the implementation into the truss equation. The same needs to be done for the lateral motions. These are surge and higher horizontal modes. Sway is assumed negligible due to double symmetry of mooring line configuration and floater configuration. As for the vertical motions, the lateral motions are described by O. M. Faltinsen (2010) and Kristiansen (2012), where the latter combines the floater model with the truss model.

The lateral motions are based on the curved beam model, with the exception of surge motion. This is because the present model cannot account, properly, for the structural inertia forces arising from rigid-body surge motion. Thus, surge will be treated separately by a rigid-body model. In this section, the procedure of treating the surge motion is first presented, followed by the radial motion.

2.8.1 Surge equation of motion

Since the surge motion is a rigid-body motion and can not be described by a curved beam model, it is given as

$$M\ddot{\eta}_1 = R\int_0^{2\pi} f_1(s,t)d\beta \tag{2.52}$$

where the RHS, $f_1(s,t)$ is described similarly as for $f_3(s,t)$ in equation (2.35). $M = 2\pi Rm$ is the 3D mass of the floater, with m being the mass of the floater per unit length. $\ddot{\eta}_1$ considers the surge acceleration of the floater.

The surge properties are not generalised and solved per unit length. Instead, they are found as 3D values. In surge, the radial motion of the floater is given by $\eta_1 \cos(\beta)$. This is used to find the added mass force in surge as well as the wave excitation force.

2.8.2 Surge added mass force

The added mass per unit length for radial motion is given as

$$a_{rr} = \frac{1}{2}\pi\rho c^2 \tag{2.53}$$

With the radial motion in surge, the radial added mass force can be found by

$$f_r^{added\ mass} = -\ddot{\eta}_1 a_{rr}\cos(\beta) \tag{2.54}$$

Taking the x-component of the force, being the surge motion, multiplying by the outer radius and integrating from 0 to 2π one obtain the 3D added mass in surge

$$A_{11} = \frac{1}{2}\rho\pi^2 Rc^2 = \pi R a_{rr} \tag{2.55}$$

The equation of motion in surge is now given as

$$(M + A_{11})\ddot{\eta}_2 = R\int_0^{2\pi} (f_1^{exc} + f_1^{trusses})d\beta \tag{2.56}$$

2.8.3 Surge wave excitation force

The wave excitation force in surge is found by the radial excitation force per unit length of the floater, given in a similar way as for the vertical by O. M. Faltinsen (2011).

$$f_r^{exc} = 2a_{rr}\zeta_a\omega^2 e^{(-i\omega t)}\Big(J_0(kR) + 2\sum_{n=1}^{\infty} i^n J_n(kR)\cos(n\beta)\Big)\cos(\beta) \tag{2.57}$$

with the x-component giving the surge contribution

$$f_1^{exc} = 2a_{rr}\zeta_a\omega^2 e^{(-i\omega t)}\Big(J_0(kR) + 2\sum_{n=1}^{\infty} i^n J_n(kR)\cos(n\beta)\Big)\cos^2(\beta) \tag{2.58}$$

Multiplied by R and integrated from 0 to 2π, the 3D wave excitation force in surge is given as

$$F_1^{exc} = 2A_{11}\zeta_a\omega^2 e^{(-i\omega t)}\Big(J_0(kR) - J_2(kR)\Big) \tag{2.59}$$

The equation of motion in surge is now given as,

$$(M + A_{11})\ddot{\eta}_2 = 2A_{11}\zeta_a\omega^2 e^{(-i\omega t)}\Big(J_0(kR) - J_2(kR)\Big) + R\int_0^{2\pi} f_2^{trusses}d\beta \tag{2.60}$$

2.8.4 Coupling of floater and truss: Surge

The truss forces on the floater in equation (2.60) will be dealt with according to equation (2.48). As the surge motion acts in the x-direction, the truss forces are thus multiplied with the **i** vector. The final equation of motion in surge is

$$(M + A_{22})\ddot{\eta}_1 = 2A_{11}\zeta_a\omega^2 e^{(-i\omega t)}\Big(J_0(kR) - J_2(kR)\Big) + \sum_{ft=1}^{N_{ft}} \gamma_{ft}T_{ft}(s_{ft}\cdot\mathbf{i}) \tag{2.61}$$

Treating the acceleration in a similar manner as for the vertical motion, the acceleration of a floater node q can be expressed in terms of tension-related and non-tension related. This gives the following acceleration in surge for a floater node.

$$\ddot{\eta}_{q,1} = \underbrace{\sum_{ft=1}^{N_{ft}} \left\{ \frac{\gamma_{ft} T_{ft} (s_{ft} \cdot \mathbf{i})}{(M + A_{11})} \right\}}_{\ddot{\eta}_{q,1,T}} + \underbrace{\frac{2A_{11}\zeta_a \omega^2 e^{(-i\omega t)}}{(M + A_{11})} \Big(J_0(kR) - J_2(kR) \Big)}_{\ddot{\eta}_{q,1,rest}} \tag{2.62}$$

As for the vertical motion, we want to couple the floater and trusses by their acceleration. The surge acceleration can be included into the $\mathbf{A} = b$ system for a floater node. This is done in a similar manner as in equation (2.50) and equation (2.51), being either an i node or a j node respectively.

$$\mathbf{s}_k^n \cdot (\mathbf{a}_j^n - \ddot{\eta}_{q,1,T}^n) - \frac{T^n}{k\Delta t^2} = -\frac{b^n}{2l_k} - \mathbf{s}_k^n \left(\frac{c^n}{\Delta t} - \ddot{\eta}_{q,1,rest}^n\right) - \frac{T^{n-1}}{k\Delta t^2} \tag{2.63}$$

$$\mathbf{s}_k^n \cdot (\ddot{\eta}_{q,1,T}^n - \mathbf{a}_i^n) - \frac{T^n}{k\Delta t^2} = -\frac{b^n}{2l_k} - \mathbf{s}_k^n \left(\frac{c^n}{\Delta t} + \ddot{\eta}_{q,1,rest}^n\right) - \frac{T^{n-1}}{k\Delta t^2} \tag{2.64}$$

2.8.5 Radial curved beam equation

The radial motions of the floater are based upon the same curved beam model as for the vertical motions. We denote v as the radial motion of the model, and thus obtain

$$m\frac{\partial^2 v}{\partial t^2} + EI\frac{\partial^4 v}{\partial s^4} + \frac{EI}{R^2}\frac{\partial^2 v}{\partial s^2} = f_2(s,t) \tag{2.65}$$

where the RHS, $f_2(s,t)$ is given in the surge equation of motion.

2.8.6 Radial modal equation of model

As for the vertical motion, the lateral motion of the floater model is described by radial modal components, given by equation (2.32).

From O. M. Faltinsen (2010), the equation requires that there can be no uniform contraction or expansion of the floater. Thus one have excluded mode $n = 0$. Since surge is a rigid-body motions, not suited to be described by the lateral curved beam model, $n = 1$ is treated separately. Equation (2.32) will therefore hold for modes $n \geq 2$.

The radial elastic modes are inserted into the radial curved beam equation (2.65) in the same manner as for the vertical motion. An important notice is that the radial added mass per unit length is the same for all modes and thus given by equation (2.53). This leads to the equation of motion becoming.

$$(m + a_{rr})\ddot{b}_n + \frac{EI}{R^4}(n^4 - n^2)b_n = \frac{1}{\pi}\int_0^{2\pi} f_r(s,t)\cos(n\beta)d\beta\Big) \tag{2.66}$$

2.8.7 Generalised radial wave excitation force

The radial wave excitation force per unit length in the radial direction are given in equation (2.57). This is then generalised in by multiplying $\cos(m\beta)$ and integrating from 0 to 2π. This leads to the generalised wave excitation force, for a given mode n, to be,

$$f_{r,n}^{gen,force} = 2\pi a_{rr}\omega^2\zeta_a e^{(-i\omega t)}(J_{n+1}(kR) - J_{n-1}(kR)) \tag{2.67}$$

The equation of motion can now be given by

$$(m + a_{rr})\ddot{b}_n + \frac{EI}{R^4}(n^4 - n^2)b_n = \frac{1}{\pi}f_{r,n}^{gen,force} + \frac{1}{\pi}\int_0^{2\pi} f_r^{truss}\cos(n\beta)d\beta\Big) \tag{2.68}$$

With the wave excitation force expressed for the radial motion, the last part is now to express the radial components of the truss forces acting on the floater and combine this into the truss equation of motion.

2.8.8 Coupling of floater and truss

When coupling the floater and truss model, a similar procedure as for the vertical motion is followed. Different for the vertical case, is that the radial direction is given by (x, y) coordinates. The idea is to express the lateral, or radial, acceleration of a floater node q on the floater and combine this into equation (2.15). The radial acceleration of the floater is

$$\ddot{v}_q(\beta_q, t) = \sum_{n=2}^{\infty} \ddot{b}_n(t)\cos(n\beta_q) \tag{2.69}$$

Expressing $\ddot{b}$ in terms of equation (2.68), $\ddot{v}_q$ can now be expressed in a numerical version. The radial acceleration of a floater node is then,

$$\begin{aligned}\ddot{v}_q = {} & \frac{1}{(m + a_{rr})}\sum_{n=2}^{\infty}\Big[-\frac{EI}{R^4}(n^4 - n^2)b_n + \frac{1}{\pi}f_{r,n}^{gen,force}\Big]\cos(n\beta_q) \\ & + \frac{1}{\pi(m + a_{rr})}\sum_{n=0}^{\infty}\int_0^{2\pi} f_r^{truss}\cos(n\beta)d\beta\cos(n\beta_q)\end{aligned} \tag{2.70}$$

The radial truss forces are described like that of the vertical truss forces. The integral is simplified as a sum over all trusses connected to the floater. Each with the same division as shown in figure 2.9.

$$
\begin{aligned}
\int_0^{2\pi} f_r^{truss}\cos(n\theta)d\theta &\simeq \sum_{ft=1}^{N_{ft}} f_{r,ft}^{truss}\cos(n\theta)\Delta\theta \\
&= \frac{1}{\Delta s}\sum_{ft=1}^{N_{ft}} \left(\gamma_{ft}T_{ft}\left(\mathbf{s}_{ft,r}\cdot\mathbf{r}\right)\right)\cos\left(n\theta_{ft}\right)\Delta\theta \\
&= \frac{1}{R}\sum_{ft=1}^{N_{ft}} \left(\gamma_{ft}T_k\left(\mathbf{s}_{ft,r}\cdot\mathbf{r}\right)\right)\cos\left(n\theta_{ft}\right)
\end{aligned}
\tag{2.71}
$$

Here $\mathbf{s}_{ft,r}$ is the radial direction of the tangential vector for a floater truss ft, and is defined by,

$$
\begin{aligned}
s_{ft,r} &= \mathbf{s}_{ft}\cdot\mathbf{r} \\
&= \mathbf{s}_{ft}\cdot[\cos(\beta_{ft}),\sin(\beta_{ft}),0] \\
&= s_{ft1}\cos(\beta_k) + s_{ft2}\sin(\beta_{ft})
\end{aligned}
\tag{2.72}
$$

Figure 2.10 illustrates the different components of $\mathbf{s}_{ft}$ for a floater truss.

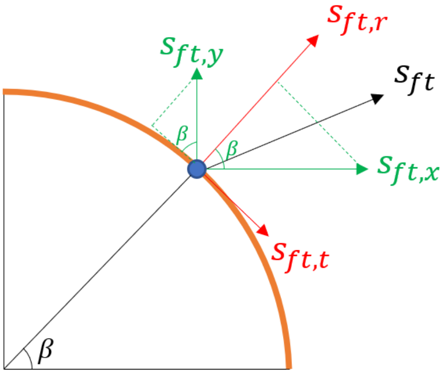

Figure 2.10: Illustration of the different vector components found from a floater truss.

The radial acceleration of a floater node q can thus be given as,

$$\begin{aligned}\ddot{v}(\beta_q, t) = &\underbrace{\frac{1}{\pi R(m + a_{rr})} \sum_{n=2}^{\infty} \sum_{ft=1}^{N_{ft}} \gamma_{ft} T_{ft} s_{ft,r} \cos(n\beta_{ft}) \cos(n\beta_q)}_{\ddot{v}_{q,T}} \\ &+ \underbrace{\frac{1}{(m + a_{rr})} \sum_{n=2}^{\infty} \Big[-\frac{EI}{R^4}(n^4 - n^2) b_n + \frac{1}{\pi} f_{r,n}^{gen,force} \Big] \cos(n\beta_q)}_{\ddot{v}_{q,rest}}\end{aligned} \tag{2.73}$$

The tension related part are found in $\ddot{v}_{q,T}$, while the rest are placed in $\ddot{v}_{q,rest}$. The floater node can now be included into the truss model. The nodeal acceleration is made three-dimensional by multiplying with $\mathbf{r} = [\cos(\theta), \sin(\theta), 0]$. Secondly it is inserted as an acceleration $\mathbf{a}_q$ of equation (2.15) being either an i or j-node. Equation (2.74) and equation (2.75) shows the resulting combined equation for the case of a floater node q being an i-node or j-node, respectively.

$$\mathbf{s}_r \cdot (\ddot{v}_{q,T}^n \cdot \mathbf{r} - \mathbf{a}_i^n) + \frac{T^n}{k\Delta t^2} = -\frac{b^n}{2l_k} - \mathbf{s}_r \Big(\frac{\mathbf{c}^n}{\Delta t} - \ddot{v}_{q,rest}^n \cdot \mathbf{r} \Big) - \frac{T^{n-1}}{k\Delta t^2} \tag{2.74}$$

$$\mathbf{s}_r \cdot (\mathbf{a}_j^n - \ddot{v}_{q,T}^n \cdot \mathbf{r}) + \frac{T^n}{k\Delta t^2} = -\frac{b^n}{2l_k} - \mathbf{s}_r \Big(\frac{\mathbf{c}^n}{\Delta t} + \ddot{v}_{q,rest}^n \cdot \mathbf{r} \Big) - \frac{T^{n-1}}{k\Delta t^2} \tag{2.75}$$

These are then arranged into the system of equation $\mathbf{A} \cdot T = b$, where all unknown tension related terms are found on the LHS and the others are on the RHS.

Now, all necessary theory for implementing the coupled truss-floater model is given. A brief description of how to implement the multi-tori follows. Further, a short section of how to include damping to the floater and the trusses, in order to stabilise the solution is presented.

2.9 Expanding to multi-tori concept

A thorough description of coupling the truss model from Marichal (2003) with a single torus, described by O. M. Faltinsen (2011) and P. Li (2017), has been given. When including several tori, a main difference is that there are now $floater - trusses$ used to create elastic bands or connections between the tori. These can either be be composed of one single truss or several trusses. This implies that one of such truss, can have two of its nodes located on floaters. Thus both of its nodes inhibits the floater properties. Another situation will be to have the truss with on node connected to the floater and the other connected to another elastic truss. This truss will be represented by the combined equations derived earlier, and direct analogy to the mooring-line trusses. These differ only in boundary condition for the non-floater node. Lastly, an elastic band (truss) can have both of its nodes connected to other trusses. Such systems have been derived in section 2.2.1 and with examples in appendix B. These are updated into **A** and b accordingly.

The trusses in the model are numbered in a straight line from the inner torus to outer torus and then continue at a new line rotating anti-clockwise.

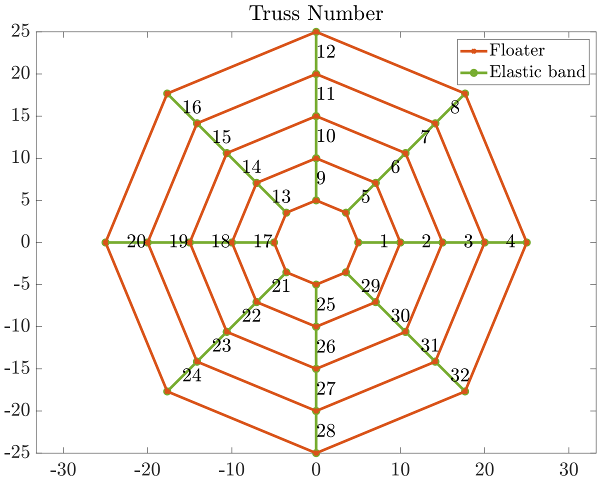

Figure 2.11: Illustration of truss numbering of solar island model with MATLAB. Plot show the systematic numbering of the trusses, used to make up the elastic bands connecting the tori together. Here one elastic band is made from one truss.

Categorising the nodes by their type, we get the following ways of updating the nodal acceleration.

$$\begin{aligned}
\mathbf{a}_q &= \ddot{\eta}_1 \cdot \mathbf{i} + \ddot{v}_q \cdot \mathbf{r} + \ddot{w} \cdot \mathbf{k} \\
\mathbf{a}_{ci} &= T_k \mathbf{s}_k - T_{k-1} \mathbf{s}_{k-1} + \mathbf{g} \\
\mathbf{a}_{cj} &= T_{k+1} \mathbf{s}_{k+1} - T_k \mathbf{s}_k + \mathbf{g} \\
\mathbf{a}_m &= [0, 0, 0]
\end{aligned}$$

Here $\mathbf{a}_q$ is the acceleration of floater node q, $\mathbf{a}_{ci}$ and $\mathbf{a}_{cj}$ is the i-node and j-node acceleration respectively. $\mathbf{a}_m$ is the mooring node acceleration always set to be a zero-vector as it has a fixed boundary condition. The **A**-matrix is updated based on the type of node we study and to which trusses it is connected. Similarly for b-vector.

2.10 Modal damping and truss damping

When using time integration scheme, there is usually a requirement that the time-step is sufficiently low for the solution to converge. For systems experiencing rapid changes, i.e. significant changes in values over time, the solution can diverge and lead to the wrong solution. Both the floater and trusses have frequencies at which they might resonate. For situations where the system is loaded, there is a chance of the load acting as an impulse load. It will excite the natural frequencies and for an undamped system, never decay. In reality, there are structural damping that reducing these vibrations. A way of including such structural damping is to us a Rayleigh damping and calculate the critical damping of a system.

Considering a Rayleigh type of damping, we can define a damping ratio and further find the critical damping of a system. The critical damping depends on the mass and stiffness of the system and is defined in, Larsen et al. (2019), as,

$$c_{cr} = 2m\omega_0 = 2m\sqrt{\frac{k}{m}} = 2\sqrt{mk} \tag{2.76}$$

where $m = (m + a_{nn})$ is the structural mass of the system, including added mass for marine structures, k is the stiffness, and ω_0 is the natural frequency.

A convenient way of defining the damping of a system is as a ratio of the critical damping, at which the response is zero if $c = c_{cr}$. We introduce the damping ratio as,

$$\xi = \frac{c}{c_{cr}} \tag{2.77}$$

Thus, we can define the damping as,

$$c = \xi \cdot c_{cr} = \xi \cdot (m + a_{nn})\omega_0 \tag{2.78}$$

For the vertical motion and a given mode m we get,

$$c_m = \xi \cdot (m + a_{33}^m)\omega_{0,m} \tag{2.79}$$

Knowing that the damping is proportional to the velocity, it can be included into the equation of motion for the floater. For the vertical motion we define $\dot{a}_n$, by estimating $\ddot{a}_n$ from Newton's 2nd law. With the Euler time integration scheme the modal amplitudes are estimated for time instant $n + 1$ for mode m as,

$$\begin{aligned} \ddot{a}_m^n &= \frac{\sum F_{exc}}{(m + a_{33}^m)} \\ \dot{a}_m^{n+1} &= \dot{a}_m^n + \Delta t \cdot \ddot{a}_m^n \\ a_m^{n+1} &= a_m^n + \Delta t \cdot \dot{a}_m^{n+1} \end{aligned} \tag{2.80}$$

The case is similar for surge motion and radial motion. The vertical equation of motion in equation (2.39) can thus be expanded to,

$$(m - a_{33}^{n})\ddot{a}_n + c_n \cdot \dot{a}_n + \Big(\rho g b_w + (n^4 - n^2)\frac{EI}{R^2}\Big)a_n = \frac{1}{\alpha_n \pi}\int_0^{2\pi} (f_3^{exc}) \cos(m\beta) d\beta\Big) \tag{2.81}$$

Chapter 3

Hydrodynamic interaction

In the following chapter, it is decided, with communication with supervisor Prof. Kristiansen, to present a way of accounting for hydrodynamic interaction of a torus due to the presence of other tori. The following theory is based on an ongoing, unpublished paper (2020) of Prof. Kristiansen, using the findings done by O. M. Faltinsen (2011). The same assumptions used for deriving the equation of motion for a torus are used. The ZFT is assumed, we only consider the hydrodynamic interactions to be present for vertical motions and neglect all non-linear loads. A near-field approach and a far-field approach to the problem is derived for a two tori case. This is later generalised for several tori and modes.

3.1 Hydrodynamic interaction

Hydrodynamic interaction occurs as a result of changes in forces acting on an object due to the presence of another object. In our case, there is a coupling between the tori acting through the fluid. The forces occur as a cross-coupled added mass force, as the motion of a torus induces a pressure disturbance throughout the fluid. This, in turn, induces a pressure load on the other tori in a present model. With ZFT considered, these loads are in phase with the motion of the moving torus. An illustration of the zero-frequency limit radiation problem in heave for two tori is given in figure 3.1.

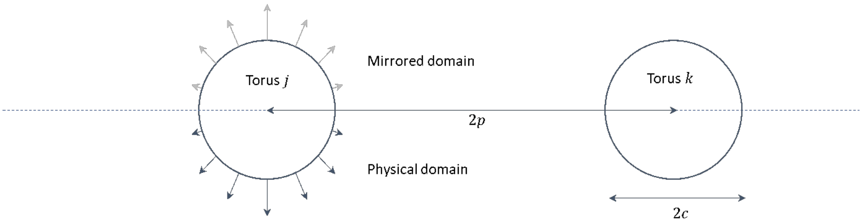

Figure 3.1: Illustration of the zero-frequency limit radiation problem of heave of the left tours j. Torus k is the neighbouring torus with center-to-center distance $2p$. The dashed line represents the still free surface at $z = 0$, of which physical domain is mirrored about.

Imagining the pressure disturbance due to a heave motion of a torus, one could imagine this to induces loads in higher modes for the other tori. This would then lead to a significant number of cross-coupled added mass terms. E.g. a five-tori concept considering ten modes would have a 50×50 system that needed to be solved. This requires much computational power. However, Debernard (2019) found through hydrodynamic analysis in WAMIT, that a torus only seem to induce added mass forces on the other tori with the same mode. This means that for a five-tori concept, a heaving motion of torus 1 only induce cross-coupled added mass in heave. Moreover, the five-tori concept with ten modes can now be solved for ten types of 5×5 systems.

3.2 Equation of motion

Now, for simplicity, considering a two-tori concept. The equation of motion for one single torus is given in equation (2.36). Now introducing the cross-coupled added mass term, we have

$$m_k \ddot{a}_{k,n} + \frac{EI_k}{R_k^4}\left(n^4 - n^2\right) a_{k,n} + b_{kw} a_{k,n} = f_{k,n}^{ex.gen} + \int_0^{2\pi} f_{k,truss} \cos n\beta d\beta - \sum_{j=1}^{K} a_{k,j,n} \ddot{a}_{j,n} \tag{3.1}$$

for $k = 1, 2, \ldots, K$ being the torus considered. K is the total number of tori. $a_{k,j,n}$ is the 2D zero-frequency limit added mass coefficient for torus k, due to motion of torus j, in mode n. For $j = k$, means the vertical added mass of the torus due to itself, already given by equation (2.37). We want to derive an expression for the cross-coupled added mass coefficient generalised for all modes. The near-field approach and a far-field approach is made. The near-field can for heave mode be found in appendix A.2. It will be seen that a far-field approach gives far better results when comparing to WAMIT.

3.3 Far-field approach for modal added mass coefficient

We expect improved accuracy using the pressure provided by the far-field solution. The far-field velocity potential due to forced modal shape of the motion $\cos(n\beta)$ of torus j is

$$\phi_j^F(x,y,z,t) = \frac{Q}{4\pi}\int_0^{2\pi} \frac{\cos(n\beta_0)}{|x - x_0|} R_j \mathrm{d}\beta_0 \tag{3.2}$$

where x_0 is the position of a source point of the circular center axis of torus j. We expand this and say z_0 and study the free surface. Further we state that $x = r\cos(\beta)$ and $y = r\sin(\beta)$ in order to transform the polar coordinates into cylindrical coordinates. We have,

$$\begin{aligned} \phi_j^F(r,\beta,0,t) =& \frac{QR_j}{4\pi}\int_0^{2\pi} \frac{\cos(n\beta_0)}{(r^2 + r_0^2 - 2rr_0(\cos(\beta)\cos(\beta_0 + \sin(\beta)\sin(\beta_0))^{0.5}} \mathrm{d}\beta_0 \\ =& \frac{QR_j}{4\pi}\int_0^{2\pi} \frac{\cos(n\beta_0)}{(r^2 + r_0^2 - 2rr_0\cos(\beta - \beta_0))^{0.5}} \mathrm{d}\beta_0 \end{aligned} \tag{3.3}$$

Assuming constant pressure over the wetted part of torus k, we evaluate $r = R_k$ and $r_0 = R_j$, and get

$$\phi_j^F(R_k,\beta,z,t) = \frac{QR_j}{4\pi}\int_0^{2\pi} \frac{\cos(n\beta_0)}{(r^2 + r_0^2 - 2rr_0\cos(\beta - \beta_0))^{0.5}} \mathrm{d}\beta_0 \tag{3.4}$$

The pressure is given by the linear term in the Bernoulli equation,

$$p_j = -\rho\frac{\partial\phi_j^F}{\partial t} \tag{3.5}$$

We are now interested in finding the vertical load in a mode m on torus k due to a motion in mode n of torus j. The pressure due to the motion in mode n of torus j is found from equation (3.4) and the Bernoulli equation, ref. equation (3.5).The 2D load per unit length on torus k is found by integrating the pressure over the wetted area of the cross-section. This can be written as

$$f_{k,j,n}(\beta,t) = \rho\int_{-\frac{\pi}{2}}^{\frac{\pi}{2}} \frac{\partial}{\partial t}\phi_j^F(R_k,\beta,0,t) n_z c \mathrm{d}\theta'' \tag{3.6}$$

or

$$f_{k,j,n}(\beta,t) = -\ddot{a}_{j,n}\frac{2}{\pi}\rho c^2 R_j \int_0^{2\pi} \frac{\cos(n\beta_0)}{(r^2+r_0^2-2rr_0\cos(\beta-\beta_0))^{0.5}}\mathrm{d}\beta_0 \tag{3.7}$$

here $Q = 4c\dot{a}_{j,n}$ in order to satisfy the boundary-condition of the inner problem in equation (3.6).

3.3.1 Total modal added mass, $A_{k,j,m,n}$

We want to find the total added mass for any mode. First the vertical modal load, of a mode m, on torus k is found from integration of equation (3.7) multiplied by $R_k\cos(m\beta)$, and integrated from 0 to 2π. Thus, the vertical load in mode m on torus k due to a mode n of torus j is given as,

$$F_{k,j,m,n}(\beta,t) = -\ddot{a}_{j,n}\frac{2}{\pi}\rho c^2 R_j R_k \int_0^{2\pi}\int_0^{2\pi} \frac{\cos(n\beta_0)}{(r^2+r_0^2-2rr_0\cos(\beta-\beta_0))^{0.5}}\mathrm{d}\beta_0\cos(m\beta)\mathrm{d}\beta \tag{3.8}$$

Further the corresponding added mass is found to be,

$$A_{k,j,m,n}(\beta,t) = \frac{2}{\pi}\rho c^2 R_j R_k \int_0^{2\pi}\int_0^{2\pi} \frac{\cos(n\beta_0)\cos(m\beta)}{(r^2+r_0^2-2rr_0\cos(\beta-\beta_0))^{0.5}}\mathrm{d}\beta_0\mathrm{d}\beta \tag{3.9}$$

For convenience we want to express the non-dimensional added mass. This is found from dividing by the structural mass of torus k, i.e $M_k = 2\pi R_k \times 0.5\rho\pi c^2$. We finally have that,

$$\frac{A_{k,j,m,n}(\beta,t)}{M_k} = \frac{2}{\pi^3}R_j \int_0^{2\pi}\int_0^{2\pi} \frac{\cos(n\beta_0)\cos(m\beta)}{(r^2+r_0^2-2rr_0\cos(\beta-\beta_0))^{0.5}}\mathrm{d}\beta_0\mathrm{d}\beta \tag{3.10}$$

3.3.2 Added mass coefficient, $a_{k,j,m,n}$

Finding the modal added mass coefficient, equation (3.7) is further used.. The hydrodynamic forces per unit length acting on torus k can be represented as a sum over all hydrodynamic load contributions from the other tori, i.e a sum of equation (3.7). Thus,

$$f^I_{k,n} = \sum_{j=1}^{K} f_{k,j,n} \tag{3.11}$$

Inserting equation (3.7) into equation (3.11) we get,

$$f^I_{k,n} = -\sum_{j=1}^{K} \ddot{a}_{j,n} \Big[\frac{2}{\pi}\rho c^2 R_j \int_0^{2\pi} \frac{\cos(n\beta_0)}{(r^2 + r_0^2 - 2rr_0\cos(\beta - \beta_0))^{0.5}} \mathrm{d}\beta_0 \Big] \tag{3.12}$$

Returning to the vertical beam equation of motion and neglecting truss forces, we can describe the cross-coupled added mass forces. Multiplying by $\cos(n\beta)$ and integrating from 0 to 2π we get,

$$m_k \ddot{a}_{k,n} + \frac{EI_k}{R_k^4}\left(n^4 - n^2\right) a_{k,n} + b_{kw} a_{k,n} = f^{ex,gen}_{k,n} + \frac{1}{\alpha_n \pi} \int_0^{2\pi} \sum_{j=1}^{K} f_{k,j,n} \cos n\beta \mathrm{d}\beta \tag{3.13}$$

$\alpha = 2$ for $n = 0$ and $\alpha = 1$ for $n \geq 1$. From equation (3.11) and equation (3.7) we can now express the cross-coupled added mass coefficient for $j \neq k$ as,

$$a_{k,j,n} = \frac{2}{\alpha_n \pi^2} \rho c^2 R_j \int_0^{2\pi} \int_0^{2\pi} \frac{\cos n\beta_0 \cos m\beta}{\left(R_k^2 + R_j^2 - 2R_k R_j \cos\left(\beta - \beta_0\right)\right)^{0.5}} \mathrm{d}\beta_0 \mathrm{d}\beta \tag{3.14}$$

which leads to the final equation of motion for mode n of a torus k,

$$m_k \ddot{a}_{k,n} + \sum_{j=1}^{K} a_{k,j,n} \ddot{a}_{j,n} + \frac{EI_k}{R_k^4}\left(n^4 - n^2\right) a_{k,n} + b_{kw} a_{k,n} = f^{ex,gen}_{k,n} \tag{3.15}$$

We have now introduced the cross-coupled added mass coefficient, and how it is included into the equation of motion. Looking closer to the wave excitation force, we understand that there will be additional wave excitation forces on a torus, due to the presence of other tori.

3.4 Wave excitation

The wave excitation force for a torus is presented in section 2.7. We understand that the wave excitation force is divided into Frodue-Kriloff forces and diffraction forces. The Froude-Kriloff part for a torus k will, for a multi tori case, be the same as for a single torus. The diffraction force by the torus k due to itself, is found similarly as for a single torus. However, in addition, the diffraction force has a BVP of linear type, with the body velocity equal to minus incident wave velocity. Thus, a load due to hydrodynamic interaction from the other tori is present. This is similarly for the radiation problem.

The Froude-Kriloff force is defined by equation (2.42), while equation (2.43) is changed slightly. Solving the boundary value problem of the torus k, we have that the added mass term in equation (2.43) now is defined as the sum over all tori, i.e

$$f_{k,n}^{\text{ex.gen}} = \zeta_a \Big(2\rho g c J_n\left(kR_k\right) - \omega^2 \sum_{j=1}^{K} a_{k,j,n} J_n\left(kR_j\right)\Big) \left(3-\alpha_n\right) \mathrm{Re}(i^{n+1} e^{-i\omega t}) \tag{3.16}$$

3.5 Solving the system

Solving a system with several tori where hydrodynamic interaction are included is now presented. Each torus has its own equation of motion, where the hydrodynamic interaction couples them. For instance, a two tori case leads to two equation of motions as,

$$\begin{aligned} \left(m + a_{1,1,n}\right)\ddot{a}_{1,n} + a_{1,2,n}\ddot{a}_{2,n} + \tfrac{EI_1}{R_1^4}\left(n^4 - n^2\right) a_{1,n} + 2b_{w1}a_{1,n} = f_{1,n}^{\text{ex.gen}} \\ \left(m + a_{2,2,n}\right)\ddot{a}_{2,n} + a_{2,1,n}\ddot{a}_{1,n} + \tfrac{EI_1}{R_1^4}\left(n^4 - n^2\right) a_{2,n} + 2b_{w2}a_{2,n} = f_{2,n}^{\text{ex.gen}} \end{aligned} \tag{3.17}$$

These can be arranged on matrix form as,

$$\begin{aligned} &\begin{bmatrix} \left(m + a_{1,1,n}\right) & a_{1,2,n} \\ a_{2,1,n} & \left(m + a_{2,2,n}\right) \end{bmatrix} \begin{bmatrix} \ddot{a}_{1,n} \\ \dot{a}_{2,n} \end{bmatrix} \\ +&\begin{bmatrix} \tfrac{EI_1}{R_1^4}\left(n^4 - n^2\right) + 2\rho g b_{w1} & \\ & \tfrac{EI_1}{R_2^4}\left(n^4 - n^2\right) + 2\rho g b_{w2} \end{bmatrix} \begin{bmatrix} a_{1,n} \\ a_{2,n} \end{bmatrix} \\ =&\begin{bmatrix} f_{1,n}^{\text{ex.gen}} \\ f_{2,n}^{\text{ex.gen}} \end{bmatrix} \end{aligned} \tag{3.18}$$

The matrices on the left-hand side of the equation are merged using the assumption that we have a steady state condition, i.e $a_{k,n} = \tilde{a}_{k,n}e^{(-i\omega t)}$, with $\tilde{a}_{k,n}$ being the forced amplitude of the mode. The time dependence are thus removed for the wave excitation force, and we finally get,

$$\begin{aligned} &\begin{bmatrix} -\omega^2\left(m + a_{1,1,n}\right) + \tfrac{EI_1}{R_1^4}\left(n^4 - n^2\right) + 2\rho g c & -\omega^2 a_{1,2,n} \\ -\omega^2 a_{2,1,n} & -\omega^2\left(m + a_{2,2,n}\right) + \tfrac{EI_1}{R_2^4}\left(n^4 - n^2\right) + 2\rho g c \end{bmatrix} \\ \cdot &\begin{bmatrix} \tilde{a}_{1,n} \\ \tilde{a}_{2,n} \end{bmatrix} = \begin{bmatrix} \tilde{f}_{1,n}^{\text{ex.gen}} \\ \tilde{f}_{2,n}^{\text{ex.gen}} \end{bmatrix} \end{aligned} \tag{3.19}$$

These creates a linear system of equations $\mathbf{A} \cdot x = b$ that are solved for x, being $\tilde{a}_{k,n}$.

Chapter 4

Verification: Implementation towards floating solar model

As part of modelling the multi-tori, verification studies have been made along the way to ensure correct implementation of theory with MATLAB. The model is made from the bottom up. A verification study of elastic trusses was performed during the project thesis, of which two cases are presented in appendix B. These are free-hanging truss system and a single pre-tension truss. The solar island model have been solved for one torus only. The model parameters used are full-scale values, mostly gathered from the experiment of Sigstad (2019) and is seen in table 4.1.

The verification study of the single torus has been a long process, consisting of much trial and error, with systematic testing the effect of different parameters. The model was made for vertical-, surge and radial motion, separately, as a different set of equations defines these, it was decided to be the best approach. It was thus possible to isolate different problems for each motion. Finally, all three motions were combined into a final single torus model. The verification studies are presented in chronological order as they were investigated during the semester. Lastly, the theory regarding hydrodynamic interaction of multi-tori model is compared with results found in WAMIT by Debernard (2019).

It is by all means not a complete verification of the single torus for the solar model. The choice has been to consider central topics of known issues regarding numerical implementations. The main goal has always been to implement a numerical code for the full solar island model. A flowchart describing the main steps of the code follows.

4.1 Flow chart

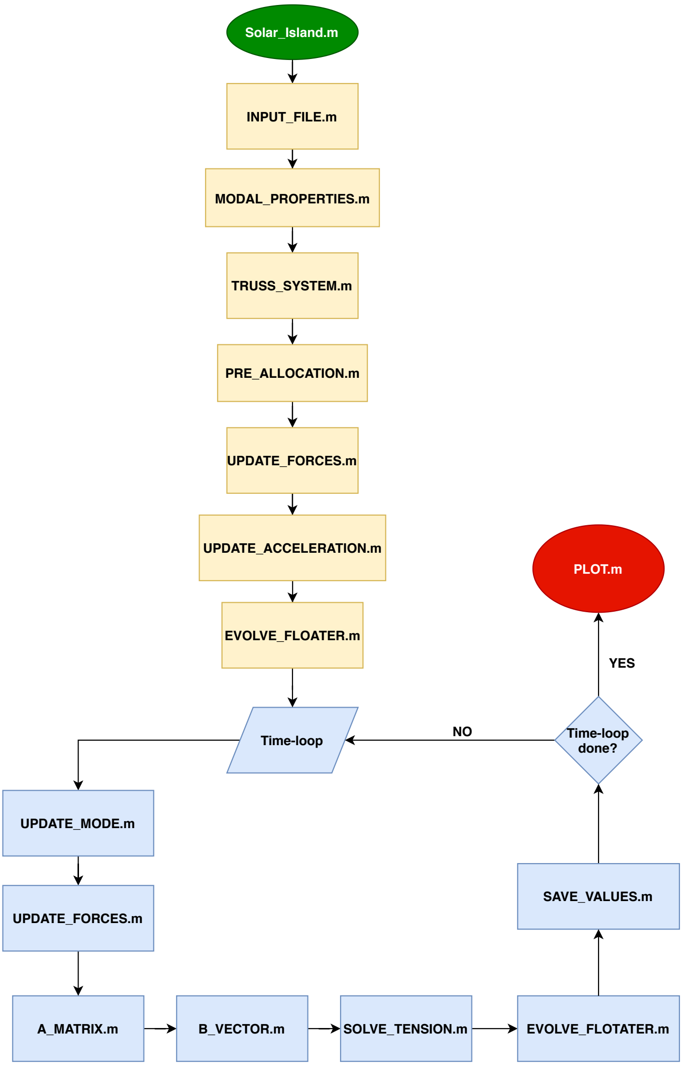

Figure 4.1: Flowchart for solar island model code $Solar\_Island.m$.

The flowchart in figure 4.1 describes the process of solving the solar island model. A short summary of function for each code is given.

- $INPUT\_FILE.m$: This is the input-file where all relevant parameters are given. It is divided into two sections: user input and automatically generated. Geometrical properties, such as numbers of tori, trusses and mass of torus. Wave parameters and numerical parameters for time integration is given. These are all given by the user. Automatic generated parameters are made based on these.
- $MODAL\_PROPERTIES.m$: Calculates the added mass for all modes, for vertical-, surge- and radial motion.
- $TRUSS\_SYSTEM.m$: Creates the geometry. Allocates what nodes are located on the floater, and which are located on the elastic bands or mooring-line. Defines floater trusses, elastic-band trusses and mooring-line trusses. Assigns corresponding stiffness to trusses and lumps mass into node.
- $PRE\_ALLOCATION.m$: Pre-allocates variables. Among these are, modal amplitude, acceleration matrix and velocity matrix. The pre-allocation is to save computational time.
- $UPDATE\_FORCES.m$: Calculates the external forces on the system. These are the wave excitation forces for the different motions and modes.
- $UPDATE\_ACCELERATION.m$: Calculates the 3D acceleration for each node.
- $EVOLVE\_FLOATER.m$: Uses the nodal acceleration and Euler time integration scheme to evaluate the nodal velocity and finally, the nodal displacement for the next time-step. The tangential unit vector is updated as well as the length of the trusses.
- $UPDATE\_MODE.m$: Updates the modal amplitudes for each motion. Uses the Euler time integration scheme to evaluate the modal velocity and finally, the modal amplitude.
- $A\_MATRIX.m$: Updates the $\mathbf{A}$-matrix and add the tension contributions from different type of nodes and trusses.
- $B\_VECTOR.m$: Updates the b-vector and add the non-tension contributions from different type of nodes and trusses.
- $SOLVE\_TENSION.m$: Solves the linear system of equations $T = \mathbf{A} \setminus b$. Terminates code if tension is negative, as trusses should not take compression.
- $SAVE\_VALUES.m$: Saves all relevant data used to plot later. These are saved for each time-step.
- $PLOT.m$: The final code that plots all relevant data such as, modal amplitude and tension in trusses.

4.2 Introducing Single torus

Verification study on a single torus has been done considering with and without mooring lines. In this section, the procedure of verifying the single torus is given. The vertical-surge and radial motion are presented separately as this was the case during implementation. The reader will get an overview of the challenges and factors needed to be considered during the implementation, which will result in a multi-torus, full solar island.

Table 4.1: General full scale parameters of floater that are kept constant. Most parameters are gathered from Sigstad (2019)

Description	Parameter	Full scale
Cross-sectional diameter of torus	b_w	1.6m
Torus mass per unit length	m_t	1030.4kg/m
Torus bending stiffness	EI	$2.65 \times 10^8\text{Nm}^2$
Radius of outer torus	R	25m
Centre-to-centre distance between connecting torus	$2p$	5m
Number of mooring lines	N_M	4

Table 4.1 show the general full scale parameters gathered, where most are from Sigstad (2019). The mass per unit length of the torus is not. We assume the torus to be semi-submerged and found by taking the density of seawater multiplied with the submerged area, i.e. $m = 0.5\rho g\pi c^2$. An illustration of the single torus is given in figure 4.2, where the mooring-lines are modelled in a perfectly horizontal extent at the mean free-surface level.

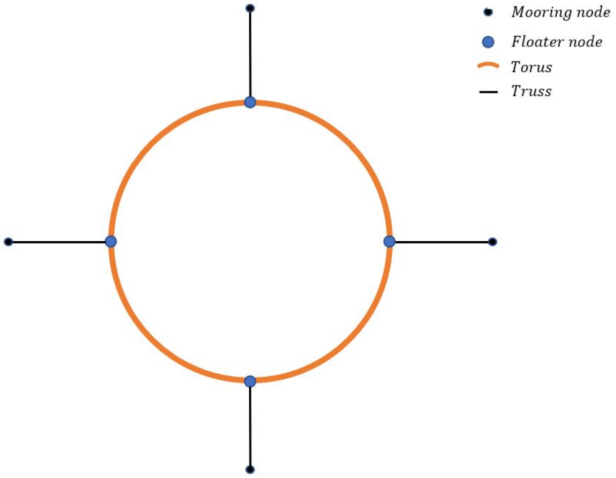

Figure 4.2: Bird view: Illustration of single torus(orange) with mooring lines(black line). Floater nodes(blue) and mooring nodes(black dot).

In the verification study, several parameters are changed. These are listed in table 4.2, and is referred to when presenting the different cases.

Table 4.2: Additional parameters, that are changed between verification cases.

Description	Parameter	Unit
Non-dimensionalised wave number	kR	[-]
Wave period	$\mathrm{T_w}$	s
Number of ramping periods	$\mathrm{N_{ramp}}$	
Time step	$\Delta\mathrm{t}$	s
End time	$\mathrm{t_{end}}$	s
Stable time	$\mathrm{t_{stab}}$	s
Mooring-line length	$\mathrm{l_m}$	m
Mooring-line pre-tension	$\mathrm{T_{p,m}}$	N
Mooring-line stiffness	$\mathrm{k_m}$	kN/m
Wave amplitude	ζ_a	m

The process of verifying the implementation of the single torus model, have consisted of first looking at the vertical motion of the floater. Later studying surge separately, then radial motion, and finally the combined motion of the single floater. These are presented in chronological order in terms of when they were studied.

4.3 Vertical motion of single torus

The implementation of the vertical motion consists of several verification steps in order to obtain a valid and satisfactory model. Note that case numbering is based on headline section for will be reused after been discussed.

Ramping

The vertical motion of the single torus is found considering the four lower modes. The test runs are given in table 4.3.

Table 4.3: Parameters for the first verification test for vertical motion of single floater. Two cases are used to see effect of ramping on the system. Length of mooring line, $l_m = 1000m$.

Case	kR $[-]$	ζ_a $[m]$	k_m $[N/m]$	$T_{p,m}$ $[N]$	Δt $[s]$	ξ_damp $[\%]$	N_ramp $[-]$	t_end $\cdot T_w[s]$
1	1.01	0.1	$36 \cdot 10^3$	78125	0.005	0	0	40
2	1.01	0.1	$36 \cdot 10^3$	78125	0.005	0	10	40

For the present cases a Fast-Fourier Transform (FFT) is used in MATLAB to find the frequencies present in the response, with and without ramping. The sample is taken to be from N_{ramp} to t_{end} in order to get a range little affected by the ramping. One should expect that system with zero damping should inhibit the natural frequencies of each mode activated as well as the incident wave frequency. The z-position of the four nodes on the floater are plotted in time.

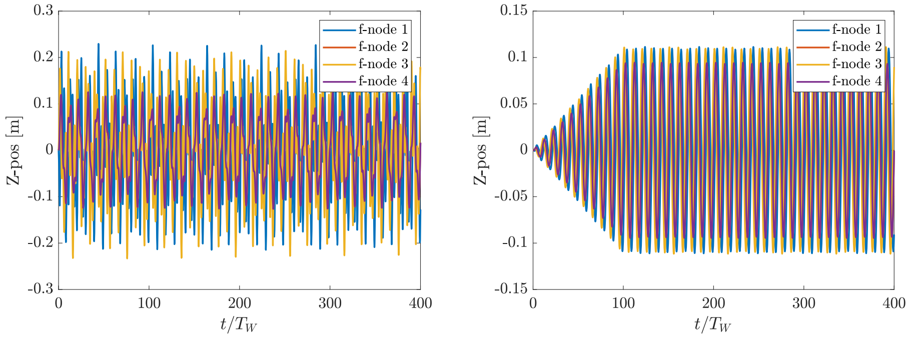

(a) No ramping **(b)** Ramping

Figure 4.3: Ramping effect of Z-position for vertical response of a single floater, with the first four modes activated

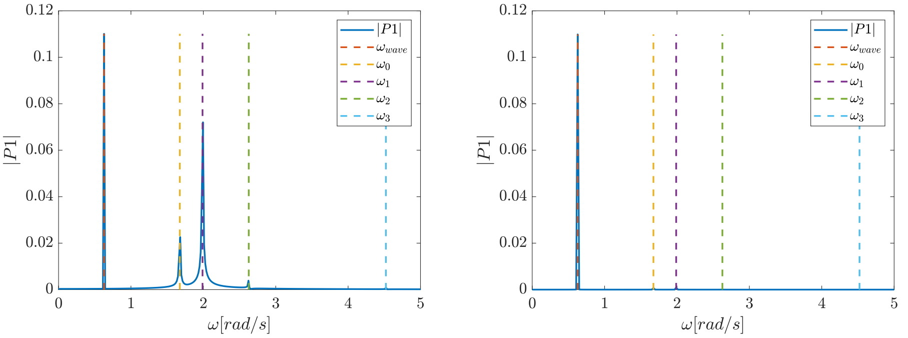

(a) No ramping **(b)** Ramping

Figure 4.4: Ramping effect of FFT for vertical response of a single floater, with the first four modes activated

From figure 4.4 it is clear that the natural modal frequencies are highly damped when ramping is included. This is the desired behaviour, as it is expected that the frequencies are triggered due to an impulse kind of loading, when ramping is not included. Figure 4.3 show how the disturbances in z-position is affected by the ramping.

Rayleigh damping

As we see, the system is strongly affected by the natural frequency of the modes included if not ramped. It is believed that including Rayleigh damping also can reduce this behaviour. For the cases above, Rayleigh damping is now included. We study the effect of the response, including structural damping. The damping is $\xi = 2\%$ and included into the model according to the theory presented above, ref section 2.10.

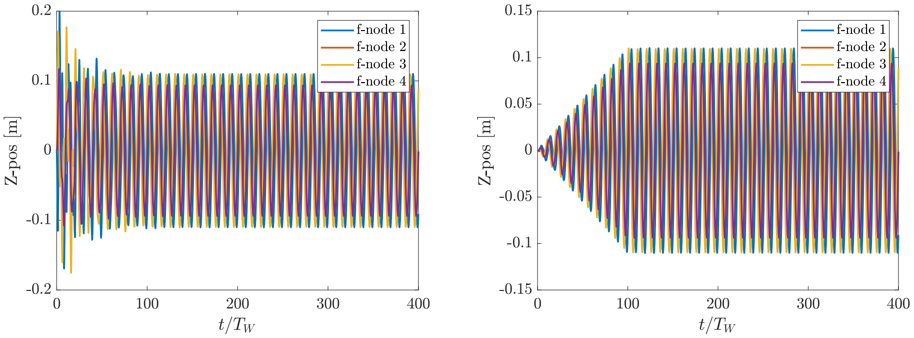

(a) No ramping **(b)** Ramping

Figure 4.5: Ramping effect of Z-position for vertical response of a single floater, with the first four modes activated

From the z-position in figure 4.5 it is clear that with Rayleigh damping, the effect of the modal frequencies are reduced. Although both being harmonically in behaviour, it is seen that the first time instant for section 4.3 there is an impulse kind of behaviour, which is not desired. Thus also including ramping, the loading of the model is gradually, and impulse loads does not seem to be present.

Time-step study

The time-step above have not been chosen thoroughly. A time-step study must be investigated to get a sense of the sensitivity of the model. Thus, a set of time-steps have been used to plot the RAO for the heave motion, not considering the mooring-lines. This is done to easier compare the floater response to the RAO from ZFT. The RAO is solved for a set of non-dimensional wave numbers kR values, according to the natural frequency of the mode. A time series analysis of each kR is done, with coarser step chosen towards the ends. Using FFT for each time series, the amplitude of the frequency is found and can be divided by the wave amplitude ζ_a, as described in section 2.5. The result is presented in figure 4.6.

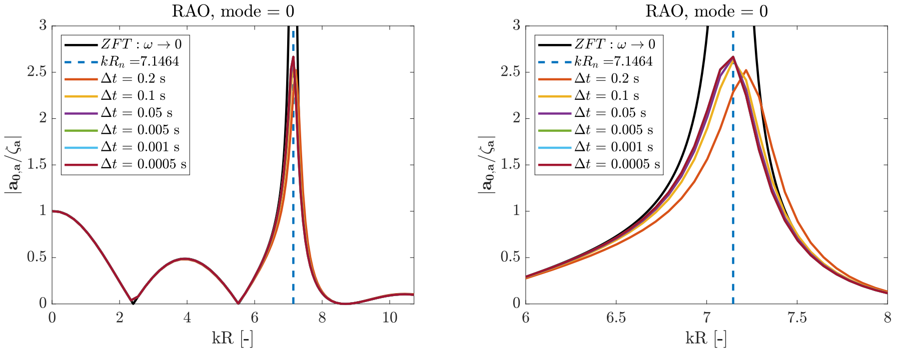

Figure 4.6: RAO in heave for different time-step compared with ZFT(black). Overview(left) and detailed RAO(right). Natural kR marked as blue dotted line. Damping is set to $\xi = 1\%$.

Figure 4.6 show the effect of changing the time-step. As for the damped RAO, the lower and higher kR are predicted perfectly. Near natural frequency $\Delta t = 0.2s$ has a peak at resonance shifted to the right. This is not favourable and indicates a too coarse time-step. However, it is surprising how fast the model seems to converge for lower time-steps. Even $\Delta t = 0.1s$ gives a good representation. A choice in time-step should, however, be lower as a later coupling will prove a more complex system and hence more sensitive to numerical errors. The vertical motion has been studied and can be included into the combined system. The previous cases were done with the time-step of $\Delta t = 0.005s$, which can be seen as a decent choice.

By studying the overall effect of including a Rayleigh damping to the model, it is interesting to find the RAO for different damping ratios and compare. This is done for the 10th lowest vertical modes using the properties given in table 4.4. The mooring-lines are not included for the same purpose as mentioned above.

Table 4.4: Parameters for RAO: vertical modes with damping.

Case	kR $[-]$	ζ_a $[m]$	k_m $[N/m]$	$T_{p,m}$ $[N]$	Δt $[s]$	ξ_{damp} $[\%]$	N_{ramp} $[-]$	t_{end} $\cdot T_w[s]$
1		0.1			0.005	[1, 2, 3]	100	200

Note that the number of ramping periods are increased. This is the case for stable time and end time, and is due to some wave periods requiring longer ramping in order to stabilise the system. T_W is decided based on the chosen kR.

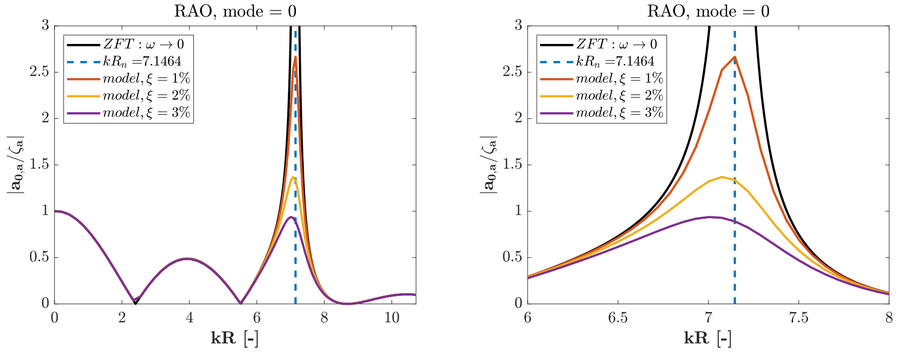

Figure 4.7: RAO in heave for different damping ratio compared with ZFT(black). No mooring-lines. Overview(left) and detailed RAO(right). Natural kR marked as blue dotted line.

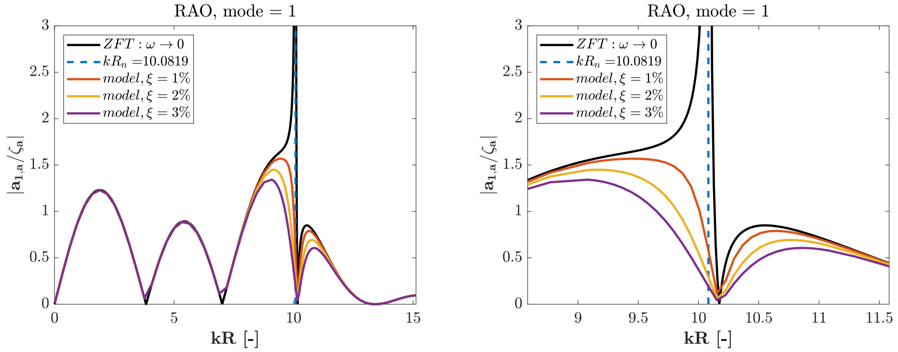

Figure 4.8: RAO in pitch for different damping ratio compared with ZFT(black). No mooring-lines. Overview(left) and detailed RAO(right). Natural kR marked as blue dotted line.

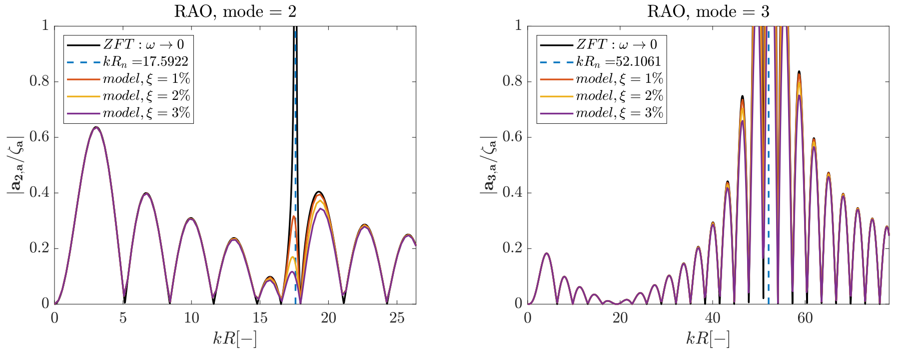

Figure 4.9: RAO for first- and second flexible vertical mode for different damping ratio compared with ZFT(black). No mooring-lines. Overview(left) and detailed RAO(right). Natural kR marked as blue dotted line

The RAO in heave and pitch is affected by the choice of damping ratio around resonance frequency of $kR \approx 7.15$ and $kR \approx 10.1$, respectively. For lower, and higher, kR values, the model seems to match the ZFT well. In general, it is seen that a higher damping ratio reduces the amplitude. For heave the peak shifts towards lower kR. This shift is consistent with Larsen et al. (2019). The reduction is somewhat considerable for a relatively small damping ratio of $\xi = 3\%$. However, this will not be studied any further, but a general trend is that the model follows ZFT for most kR values. Plots of RAO of different modes are found in appendix C.

4.4 Surge motion of single torus

Like for the vertical motion, there are several steps included for the surge motion in order to verify its potential. The surge motion is a rigid motion, where mooring-lines are mainly intended as station-keeping systems, O. M Faltinsen (1990).

Time-step study

The time-step study in surge uses the same properties as for the vertical study, now with mooring line configuration.

Table 4.5: Parameters for time-step study of surge motion. Mooring-line length of $100m$.

Case	kR $[-]$	ζ_a $[m]$	k_m $[N/m]$	$T_{p,m}$ $[N]$	Δt $[s]$	ξ_{damp} $[\%]$	N_{ramp} $[-]$	t_{end} $\cdot T_w[s]$
1	[0.1-3]	0.1	$36 \cdot 10^3$	78125		1	40	125

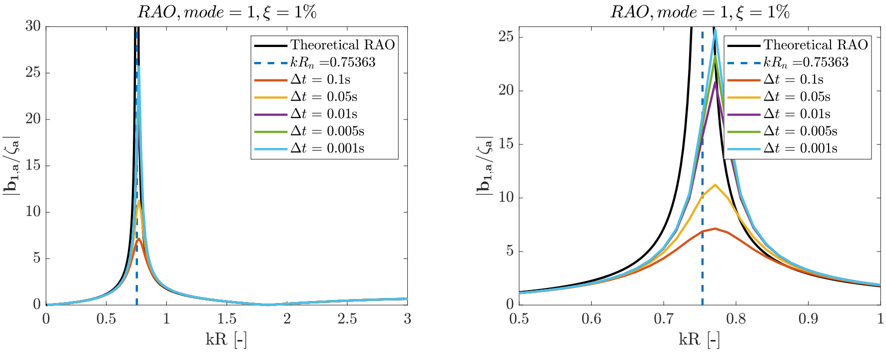

Figure 4.10: RAO in surge for different time-step compared with theoretical RAO(black). Overview(left) and detailed RAO(right). Natural kR marked as blue dotted line. Rayleigh damping is set to $\xi = 1\%$.

The RAO is seen to increase in amplitude as the time-step is decreased. It is, however, not seen to completely converge. For $\Delta t = 0.005s$ and $\Delta t = 0.001s$ the difference has decreased. The choice is to use $\Delta t = 0.005s$ to reduces the computational time. The choice of damping ratio is found from figure 4.11, with properties according to table 4.6.

Table 4.6: Parameters for damping study of surge motion. Mooring-line length of $100m$.

Case	kR $[-]$	ζ_a $[m]$	k_m $[N/m]$	$T_{p,m}$ $[N]$	Δt $[s]$	ξ_{damp} $[\%]$	N_{ramp} $[-]$	t_{end} $\cdot T_w[s]$
1	[0.1-3]	0.1	$36 \cdot 10^3$	78125	0.005		40	125

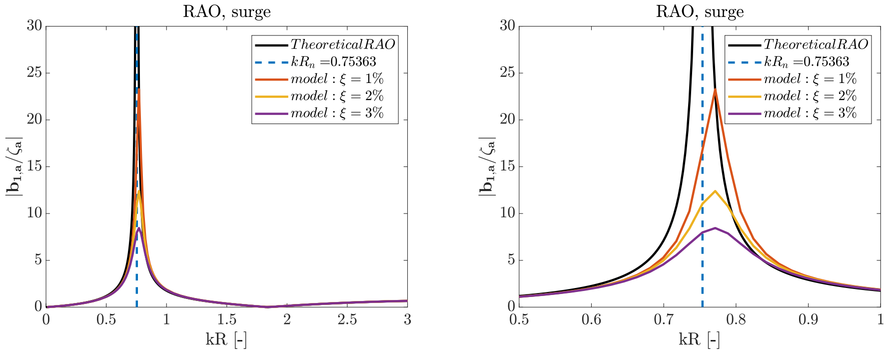

Figure 4.11: RAO in surge for different damping ratio ξ compared with theoretical RAO(black). Overview(left) and detailed RAO(right). Natural kR marked as blue dotted line. $\Delta t = 0.005s$.

It is seen that the choice of damping ratio has a direct effect on the response. $\xi = 3\%$ reduces the response by almost three times, compared to $\xi = 1\%$. The shift is towards lower kR, which is in accordance to Larsen et al. (2019). Later the choice is to use $\xi = 3\%$, as it is believed to stabilise the response better.

Mooring-lines

The surge motion can be studied looking at the tension occurring in the mooring lines. It is a rigid-body motion, and all points on the floater moves only in the x-direction and with the same magnitude. The tensions should oscillate about pre-tension for the mooring-lines being parallel to the incident wave, while the one perpendicular is never expected to not end up below pre-tension. These will experience an elongation of the mooring-line regardless of moving in positive or negative x-direction.

The mooring lines can also be represented as a stiffness term in the equation of motion. O. M Faltinsen (1990) (equation 8.26) gives the stiffness term of a structure with a spread mooring system.

$$C_{11} = \sum_{i=1}^{n} k_i \cos^2(\psi_i) \tag{4.1}$$

where ψ_i is the angle of mooring-line i, and k_i is its stiffness. In our model there are only two contributions due to the mooring configuration, i.e $C_{11} = 2k_M$. This will be included in the equation of motion with the modal amplitude, and thus replacing the truss forces.

Truss model vs Stiffness term C_{11}

Table 4.7: Parameters for surge motion case, comparing mooring forces. Case 1 uses the truss model derived in this paper, and case 2 uses the stiffness term given in O. M Faltinsen, 1990. Mooring-line length of $100m$.

Case	kR $[-]$	ζ_a $[m]$	k_m $[N/m]$	$T_{p,m}$ $[N]$	Δt $[s]$	ξ_{damp} $[\%]$	N_{ramp} $[-]$	t_{end} $\cdot T_w[s]$
1	1.572	0.1	$36 \cdot 10^3$	78125	0.005	3	40	125
2	1.572	0.1		78125	0.005	3	40	125

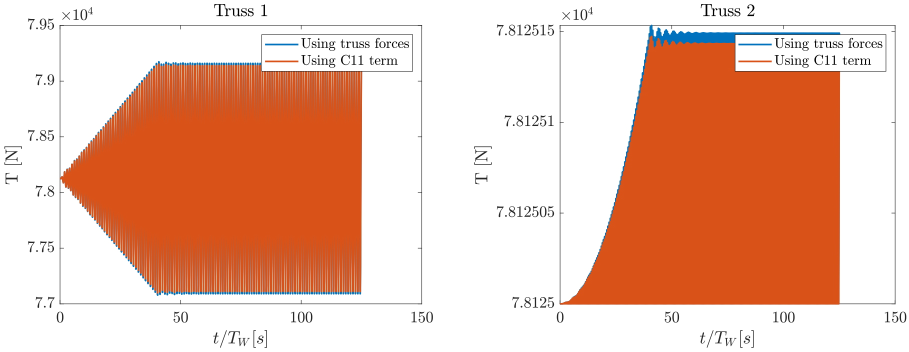

Figure 4.12: Time-seres of truss length for truss 1 (left) and truss 2 (right). Plot show comparison between developed truss model with stiffness term given by O. M Faltinsen, 1990.

Figure 4.12 show that the truss model accurately represent the trusses. Trusses in parallel with the incident wave oscillate about pre-tension. The ones being perpendicular are never below T_p, which is as expected. The comparison with including a stiffness term for representing mooring-lines are in good agreement. It should be noted that the deviation for truss 2 is negligible, and not necessarily a bad comparison. For truss 1, the change in tension is also small, but a higher tension is expected, and there are no apparent deviation between the two approaches. This indicates that the truss model, thus far, is modelled in a proper way for surge.

Mooring

The RAO in surge for the single torus model is compared with the theoretical RAO, without mooring lines. As the stiffness of the system determines the natural frequency in surge, we know that the natural frequency is 0 without mooring lines. This is seen by the equation of motion in surge not having any stiffness due to its own body.

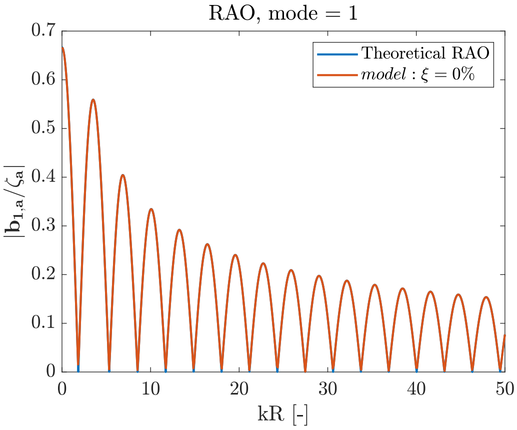

Figure 4.13: RAO in surge for single torus without mooring. No damping.

From figure 4.13 it can be seen that the model without mooring lines predicts the RAO precisely. The maximum response occurs at $\omega \rightarrow 0$, which is expected. The periodical cancellation is due to the global geometry of the floater, at which some wave-lengths cancel the global surge motion.

Next step is to include the mooring-lines for the RAO. Two values for the stiffness are used. Sigstad (2019) used $k_M = 36 \cdot 10^3 N/m$ during her experiments. The fact that her model is a five-tori model means that the total mass is greater and will result in a lower natural frequency. It is desired that the natural frequency is at low frequencies, making it rare to encounter conditions triggering resonance. For the single torus we check $k_M = 5325 N/m$, corresponding to a natural frequency of about $\omega_n = 0.21 rad/s$, or $kR_n \approx 0.11$. These are given in figure 4.14 below.

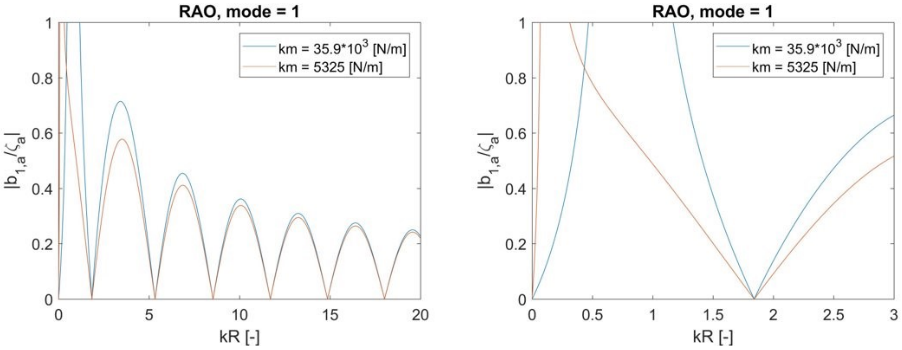

Figure 4.14: RAO in surge for different k_M. Showing the difference RAO and shift of natural frequency.

For $k_M = 5325 N/m$ it is seen that the general response is reduced, and the natural frequency is shifted towards the left, compared to $k_M = 36 \cdot 10^3 N/m$. The model respond to the changes satisfactorily. Theoretically for one floater, these should have resonance at $kR \approx 0.11$ and $kR \approx 0.75$, respectively. Looking at the right figure in figure 4.14 these seems to match quite good.

4.5 Radial motion of single torus

The last motion to be included into the model is the radial motion. The initial step has been to perform a time-step study for the first flexible mode, $n = 2$. It was decided to use the $k_M = 5325 N/m$, as it best represents the wanted natural frequency of the single floater. The properties used for the time-step study are given in table 4.8.

Table 4.8: Parameters for time-step study RAO for radial motion: 1st. flexible. Mooring-line length of $100m$.

Case	kR $[-]$	ζ_a $[m]$	k_m $[N/m]$	$T_{p,m}$ $[N]$	Δt $[s]$	ξ_{damp} $[\%]$	N_{ramp} $[-]$	t_{end} $\cdot T_w[s]$
1		0.1	5325	78125		1	100	200

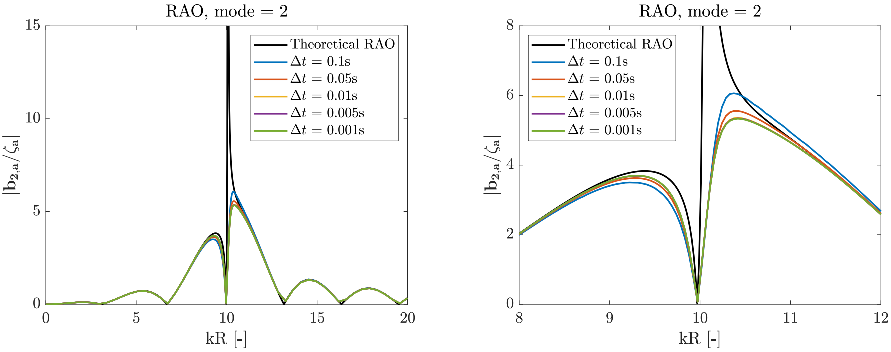

Figure 4.15: RAO in 1. flex radial for different time-step compared with theoretical RAO(black). Overview(left) and detailed RAO(right). Natural kR marked as blue dotted line. Damping ratio is set to $\xi = 1\%$.

The results clearly show a fast convergence in RAO for lower time-step. It indicates a time-step between $\Delta t = 0.005s$, and $\Delta t = 0.001s$ to be a good choice. Further, the damped RAOs are found for modes up to 10, in the range of kR from 0 to 50. The results of the four first modes are presented below, while the rest of the modes up to 10 are presented in appendix C.2.

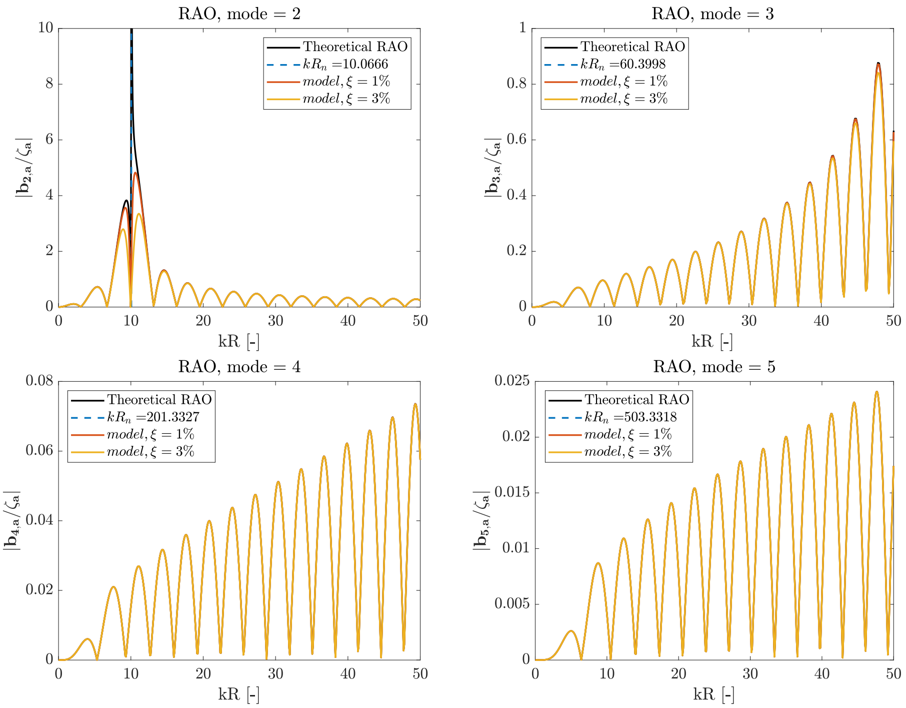

Figure 4.16: RAO for radial modes 2-4 for different damping ratio(yellow and purple), compared with theoretical RAO(black). Natural kR marked as blue dotted line. No mooring-lines. $\Delta t = 0.005s$.

Similarly, for the time-step, the damping does not seem to have much effect outside the zone of natural frequency. The model matches the theory well when mooring-lines are not considered. Including mooring lines is of interest, as the radial modes will utilise the horizontal tension component of the mooring-lines.

Including mooring-lines

The RAO with and without mooring-lines attached, are compared with theory and given for mode 2-4, in figure 4.17. The properties are the same as in table 4.8 with a time-step of $\Delta t = 0.005s$ and $\xi = 1\%$.

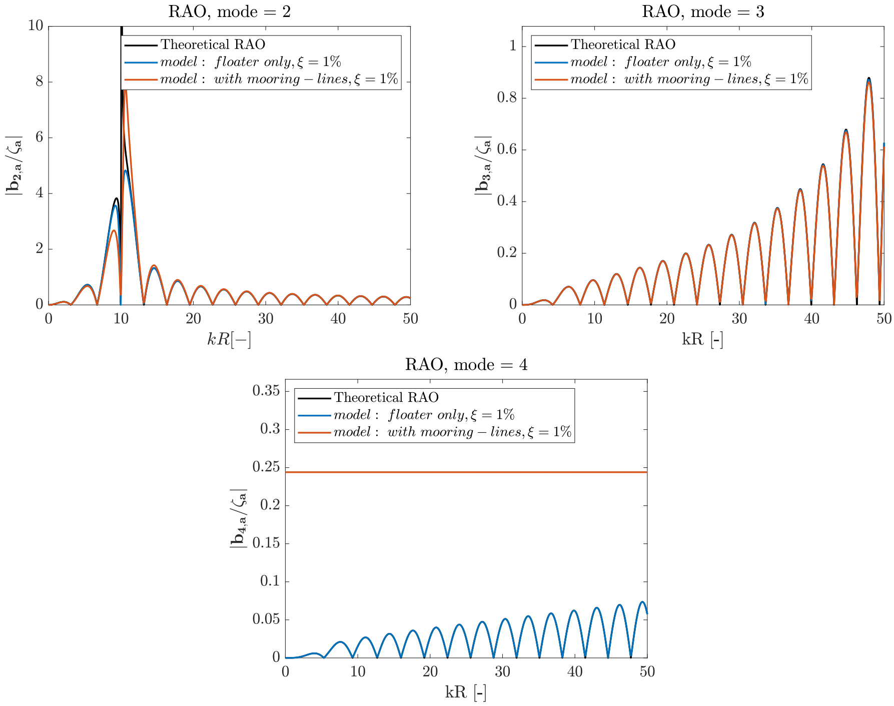

Figure 4.17: RAO for radial modes 2-4 with (orange) and without (blue) mooring-lines. $\Delta t = 0.005s$.

Figure 4.17 show interesting results. For radial mode 2 and 3, the floater response is more or less consistent with theory. At resonance, the response has a higher peak when mooring-lines are included. For radial mode 4, an interesting finding is that the response of the floater with mooring-lines have a large deviation from theory. It seems to give a more or less constant response, independent of kR. This is an indication that the implementation of the radial motion is not ideal for all modes. As the RAO for vertical modes have not been found with mooring-lines included, these were later controlled. It was found that the response had no influence of the mooring-lines for mode 4. A reason for this can be that the horizontal mooring-line configuration, giving a small vertical tension component.

Further study shows that every four radial mode encounters this issue, i.e. mode 4, 8, 12. A time series for the floater with eight radial modes are tested, where the modal amplitude is studied. A further study near the initial position is studied with a lower time-step. The parameters used are found in table 4.9.

Table 4.9: Parameters for time series with 8 radial modes activated. Mooring-line length of $100m$.

Case	kR $[-]$	ζ_a $[m]$	k_m $[N/m]$	$T_{p,m}$ $[N]$	Δt $[s]$	ξ_{damp} $[\%]$	N_{ramp} $[-]$	t_{end} $\cdot T_w[s]$
1	25.152	0.1	5325	78125	0.005	1	15	40

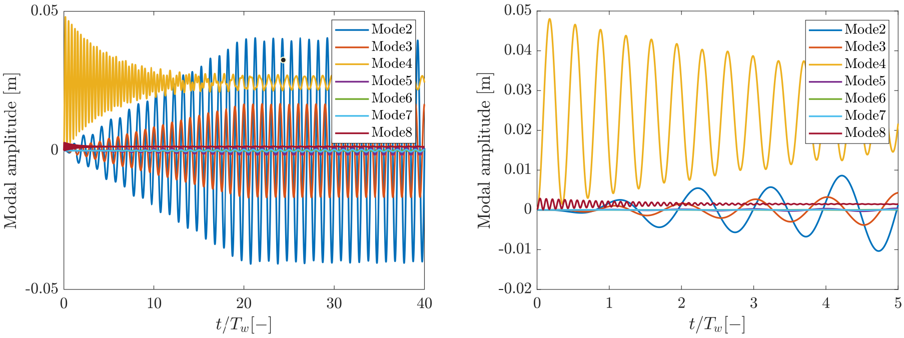

(a) $\Delta t = 0.005s$, $\xi = 1\%$

(b) $\Delta t = 0.005s$, $\xi = 1\%$

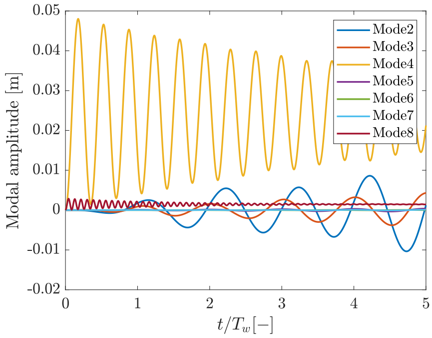

(c) $\Delta t = 0.00005s$, $\xi = 1\%$

Figure 4.18: Time series modal amplitude of floater with radial modes 2-8 activated (upper left), with mooring-lines. Close-up of time series during ramping for $\Delta t = 0.005s$ (upper right) and $\Delta t = 0.00005s$ (bottom). All with $\xi = 1\%$.

It is clear that mode 4 and 8 induce an impulse type of response, and do not oscillates about zero. In comparison, this was never observed for the vertical modes. These modes will make the response of the floater moving about a non-zero position. This is not what we want. The response is not much affected by the time-step, indicating there to be another issue present. It is decided to study the integral representing the truss-forces.

Truss-forces

From section 2.7, equation (2.71) show how the truss integral is simplified to be a sum of truss-forces on the floater. This means that the number of connections on the floater represents the number of sections, of which the floater is divided. The floater forces are lumped into the nodes connected to the trusses. It is therefore interesting to look at how these forces vary along the floater for different modes. Mode 2 is first studied, followed by mode 4.

From equation (2.70) it is seen that with the present mooring configuration we have $\theta_{ft} = [0, \pi/2, \pi, 3\pi/2]$. With $\cos(n\theta_{ft})$, this gives $[1, -1, 1, -1]$ for $n = 2$ and $[1, 1, 1, 1]$ for $n = 4$, for the respective θ_{ft}. The pattern for $n = 4$ repeats every 4 mode. This indicates that the truss-forces have a maximum contribution at all time for these modes. Looking at the modal amplitude it is observed that this creates an impulse load.

It is unclear at this point how to solve this issue, and the best option would be to exclude these modes. The choice has been only to consider the first two radial modes, as the contribution from the higher modes are of low magnitude, ref. figure 4.18a.

Further findings

With all motions verified separately, the last step is to combine these motions into a single torus model. Along the way, some notable findings have occurred. The time-step have especially been of interest. The used time-step has, for the most part, given good agreement for the verification cases. However, after studying the higher radial modes, it was discovered that the higher modes gave larger deviations between model and theory. The time-step was changed, and it clearly showed the importance of lower time-steps. The results are given in figure 4.19.

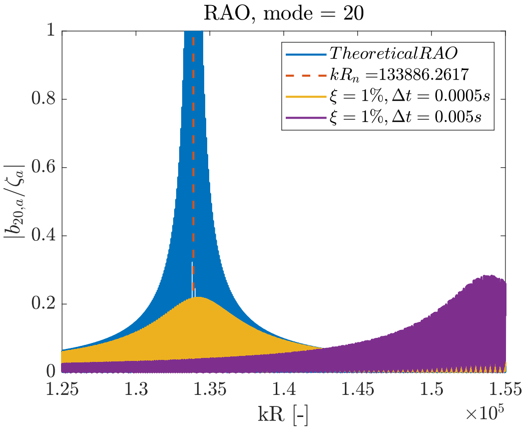

Figure 4.19: Time-step study for radial mode 20. Theoretical RAO (blue) plotted against mode 20, with $\Delta t = 0.005s$(purple) and $\Delta t = 0.0005s$ (yellow). Intended as illustration.

It should be noted that the result is only meant as an example to describe the importance of having a low enough time-step. Radial mode 20 has its natural frequency at $\omega_n = 229[rad/s]$, or $kR_n \approx 133886$. This means that the $\Delta t = 0.005s$ captures about one sample for each period. Such high frequencies are not realistic to operate in this range. So in light of these results, the time-step used later on is $\Delta t = 0.0025s$, also giving reasonable computational time.

4.6 Combined motion for single-torus model

At this point, all three motions have been verified separately. The last step towards expanding the single-torus into a full solar island model, is to combine all three motions. This was done quite straight forward, following the flowchart in figure 4.1. It was decided to perform three cases for the combined system. Three frequencies of the incident wave was varied, two of which are the natural kR_n of heave and first flexible radial. These being $kR_n = 7.146$ and $kR_n = 10.070$, respectively. Lastly a realistic wave period of $T_w = 9s$ was included, corresponding to $kR = 1.242$. These are given in table 4.10. Mooring-lines are included.

Table 4.10: Parameters for cases study of combined model for single torus, with mooring-lines. Heave, surge and first flexible radial mode are the ones included. Mooring-line length of $100m$.

Case	kR $[-]$	ζ_a $[m]$	k_m $[N/m]$	$T_{p,m}$ $[N]$	Δt $[s]$	ξ_{damp} $[\%]$	N_{ramp} $[-]$	t_{end} $\cdot T_w[s]$
1	10.070	0.1	$36 \cdot 10^3$	$333.1 \cdot 10^3$	0.0025	1	70	140
2	7.146	0.1	$36 \cdot 10^3$	$333.1 \cdot 10^3$	0.0025	1	70	140
3	1.242	0.1	$36 \cdot 10^3$	$333.1 \cdot 10^3$	0.0025	1	70	140

Case 1 is the one corresponding to the wave period from the first flexible radial, Case 2 corresponds to heave natural period, and Case 3 is the realistic wave period. The nodal position in (x, y, z) for node 1 and 2 are plotted for each case.

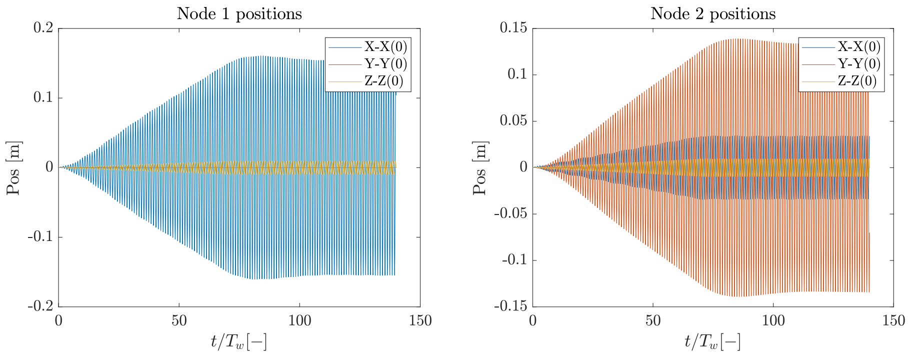

(a) Case 1 **(b)** Case 1

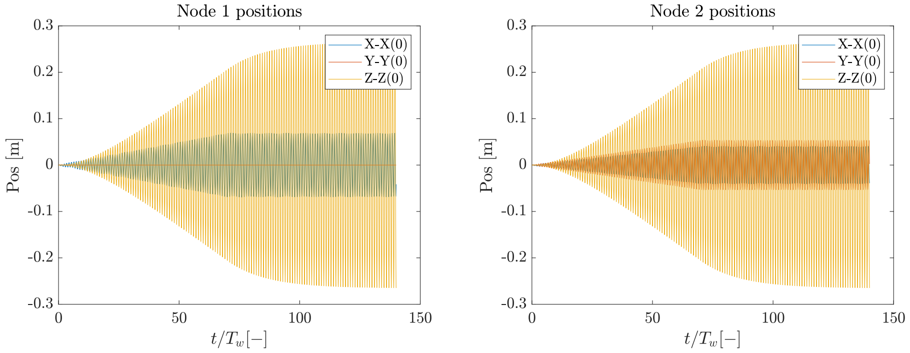

(c) Case 2 **(d)** Case 2

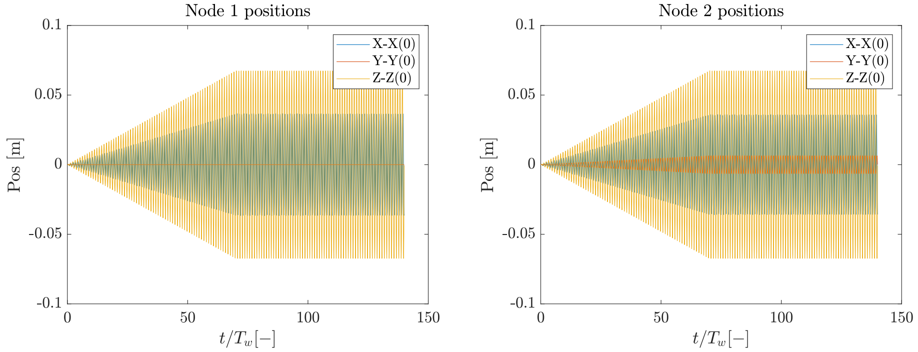

(e) Case 3 **(f)** Case 3

Figure 4.20: Time series for combined motion single torus. Three periods, all with $\xi = 1\%$.

Figure 4.20 show the response for the (x, y, z) position for node 1 and 2. To verify the results, these should be compared to the different RAOs found for each motion, with the respective $\xi = 1\%$. Figure 4.20a and figure 4.20b show the response for Case 1. With incident wave having the same kR as kR_n of the first flexible radial mode, it is expected that the $x-$motion is dominant for node 1 and $y-$motion for node 2. Looking at the figures, it is clear that it is the radial motions that are dominating.

The amplitude of the motion in figure 4.20b is approximately $0.14m$, while being about $0.16m$ for figure 4.20a. With $\zeta_a = 0.1m$ this corresponds to an RAO value of 1.4 and 1.6, respectively. Comparing to figure 4.17, the RAO near $kR = 10.06$ change value rapidly from 0 to about 2. The measured RAO for the combined case lies within. The increased value in node 1 is most likely due to the added motion from surge, which is seen from x-position in node 2. Figure 4.14 show that for $kR \approx$ 10, the RAO is about 0.36 for the current k_M, giving an additional response of $\approx 0.04m$. This is a bit more than expected, but satisfactory.

From figure 4.20, Case 2 show $z-$motion to be most dominating. Both nodes have an amplitude of $\approx 0.27m$, correspond to RAO value of 2.7. This is in accordance with figure 4.7. The x-position is present for both nodes while the y-position is only considerate for node 2. Figure 4.17 and figure 4.14 show that surge and first flex. radial mode gives similar contribution.

Case 3 show dominating z-motion. An amplitude of about 0.7 corresponds well with figure 4.7 at $kR \approx 1.2$. The radial motion is seen to be almost zero, while surge having a response of about $0.05m$, matching good with figure 4.14.

These are the concluding verification studies done on the single floater, resulting in the implementation of the full solar island with multiple tori. The last topic to be studied is the hydrodynamic interaction.

4.7 Hydrodynamic interaction

The solar island model described above does not account for hydrodynamic interactions between the tori. It is interesting to see the possible effect it has on response of the system. Debernard (2019) performed a WAMIT study on a multi-torus floater with the same geometrical properties as the ones used in this thesis. She plotted the non-dimensional added mass for different modes against p/c, where p is the distance between each tori. A comparison between the results from WAMIT, and the theory described in chapter 3, is shown in figure 4.21 and figure 4.22.

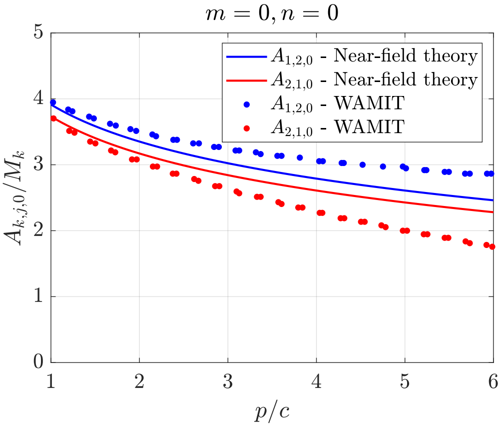

Figure 4.21: Results of non-dimensional cross-term heave added mass using near-field approach. $R_1 = 25m$, $R_2 = 20m$, and $c = 0.8m$. WAMIT results are digitised.

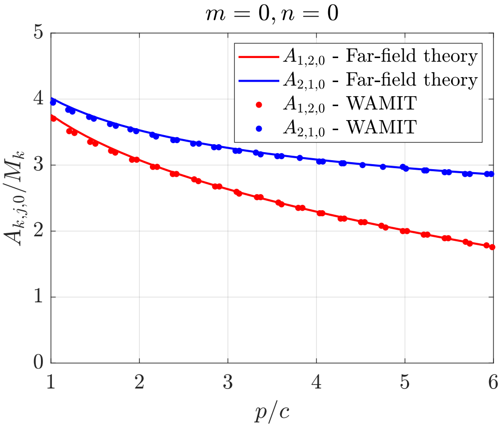

Figure 4.22: Results of non-dimensional cross-term heave added mass using far-field approach. $R_1 = 25m$, $R_2 = 20m$, and $c = 0.8m$. WAMIT results are digitised.

The numerical integration of equation (3.10) is performed with a lowest order, basic numerical integration scheme in Matlab. The results compare well with WAMIT. The near-field approach tends to deviate from WAMIT for larger p/c. There is a definite improvement between the near-field and far-field approach, where the latter matches WAMIT almost perfectly.

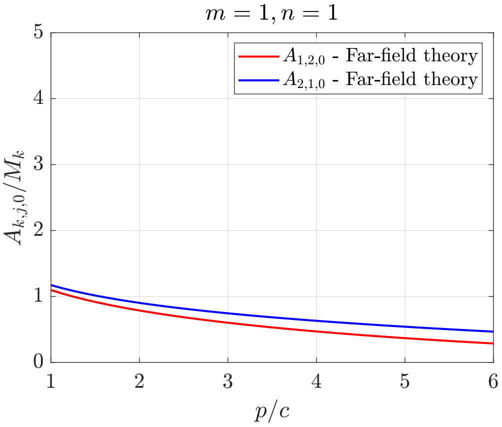

Figure 4.23: Results of non-dimensional cross-term pitch added mass using far-field approach. $R_1 = 25m$, $R_2 = 20m$, and $c = 0.8m$

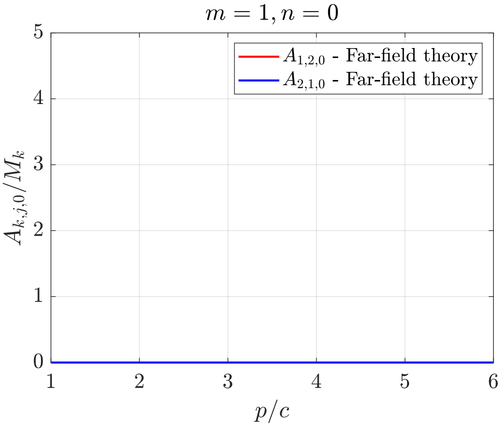

Figure 4.24: Results of non-dimensional cross-term added mass of $m = 1$ and $n = 0$ using far-field approach. $R_1 = 25m$, $R_2 = 20m$, and $c = 0.8m$

Figure 4.23 show reduction in the cross-coupled added mass for higher modes. Thus hydrodynamic interaction will have less coupling-effect for higher modes. From figure 4.24, $m \neq n$ gives zero cross-coupling, which is in agreement to results from WAMIT and the presented theory. The developed theory can account for the hydrodynamic interactions well, and can estimate these effects.

4.8 Final remarks on verification study

The implementation of the single floater has been a time-consuming process. For the verification study, it is clear that each section that is covered should be studied even further. However, it was not a possible scenario in this thesis, as the ultimate goal always was to implement the full solar island model. This lead to a shortage in time for conducting further verification. With the positive results obtained for the coupled motion, the decision was to move over to implement the final model.

It was later found that the use of a constant wave amplitude ζ_a is not a good definition of waves. This was corrected and from now on the waves are defined based on the wave steepness H/λ. The damping ratio have also been kept constant at $\xi = 1\%$. Later it is found that a damping ratio of $\xi = 3\%$ or more increase the stability of the model for a wider range of frequencies. This will be necessary for the complete solar island model. Lastly, N_{ramp} has for some cases been as high as $100 \cdot T_w$. This was done to ensure stable solutions for several frequencies, being especially important for solving the RAO. Later, this is reduced to save computational time.

Chapter 5

Results & Discussion

This chapter presents the results obtained from the full solar island. These are in turn compared and discussed with theory already given in chapter 2 and chapter 3. Main results from Sigstad (2019) and Windsvold et al. (2019)(Unpublished) are also presented, intended to be used for the discussion and comparison of results. The results for the multi-tori model are presented for two cases, a two-tori floater and a five-tori floater, both without mooring-lines. Elastic bands connect them are made up by only one single truss. This was done to simplify the problem and to more closely look at the possible structural interaction between the tori, due to the elastic bands. Wave steepness is kept constant $H/\lambda = 1/200$. Additional results for different configurations for the RAO are presented in appendix D.

Further, the hydrodynamic interaction is studied for the five-tori case, without mooring and no elastic bands. That way, only hydrodynamic interaction can create influence on one tori by the other. The results are discussed and compared to experiments to understand the influence of such effects better. For all results, the discussion will follow naturally.

5.1 Summary of performed experiment by previous students

This section is devoted to give a summary and present the main results obtained by the master thesis of Sigstad (2019) and an unpublished paper by Windsvold et al. (2019). The latter is based on the masters thesis of Windsvold (2018) accompanied by Prof. Kristiansen. It includes results of experiments done with the solar island model and the RAO for vertical modes are given for the three outermost tori.

The results presented are the three vertical RAO for the outer tori of a five-tori solar island model by Sigstad (2019), and for the three outermost tori from Windsvold et al. (2019).

The set-up for both experiments was done in *Lilletanken* at the Department of Marine Technology at NTNU, and is illustrated in figure 5.1.

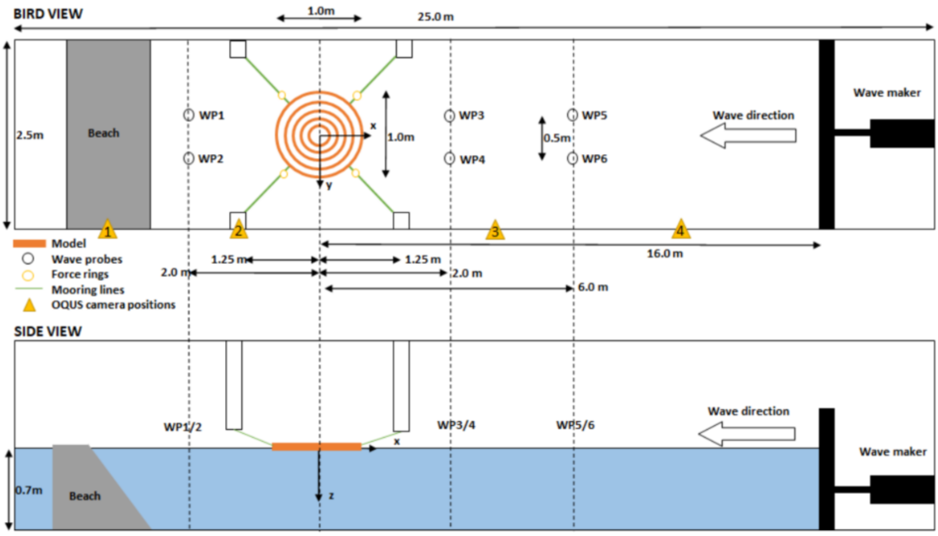

Figure 5.1: Illustration of the set-up of model in the basin Lilletanken. Description of equipment used are also given. Illustration made by Sigstad (2019)

The two experiments uses some different parameters, of which we are using the ones given by Sigstad (2019). The properties use by Windsvold et al. (2019) are given in section 5.1,

Table 5.1: Main parameters of both models and the corresponding full scale structure, used by Windsvold et al. (2019)

Description	Parameter	Model scale	Full scale
Cross-sectional diameter of tori	$2c$	32mm	1.6m
Torus mass per unit length	m	0.257kg/m	642.5kg/m
Torus bending stiffness	EI	0.8467Nm^2	2.65×10^8
Mooring-line spring stiffness	k_s	25.9N/m	64.8kN/m
Truss spring stiffness	k_t	45N/m	112.5kN/m

and for Sigstad (2019) we have,

Table 5.2: Main parameters of multi-torus in model scale and full scale used by Sigstad (2019).

Description	Parameter	Model scale	Full scale
Cross-sectional diameter of torus	2c	32mm	1.6m
Torus mass per unit length	m	0.257kg/m	642.5kg/m
Torus bending stiffness	EI	0.8467Nm^2	$2.65 \times 10^8\text{Nm}^2$
Mooring-line spring stiffness	k_s	14.0N/m	35.9kN/m
Truss spring stiffness	k_c	57.9N/m	148.4kN/m
Cross-sectional diameter of truss	d_c	3mm	0.15m

5.1.1 Results

The figures below are presented for $H/\lambda = 1/30$, for the three lowest vertical modes. Note that vertical amplitudes in the following three plots are denoted by b. Local peaks and trough are marked.

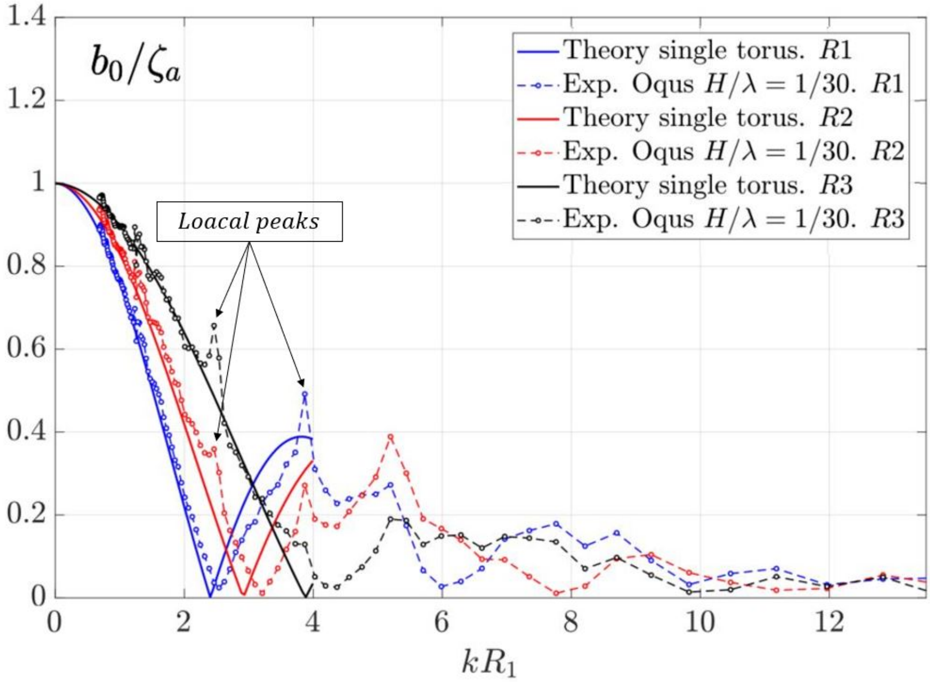

Figure 5.2: RAO in heave for the three outermost tori. Comparison between theory and experimental results. Figure from Windsvold et al. (2019). Additional comment boxes have later been added.

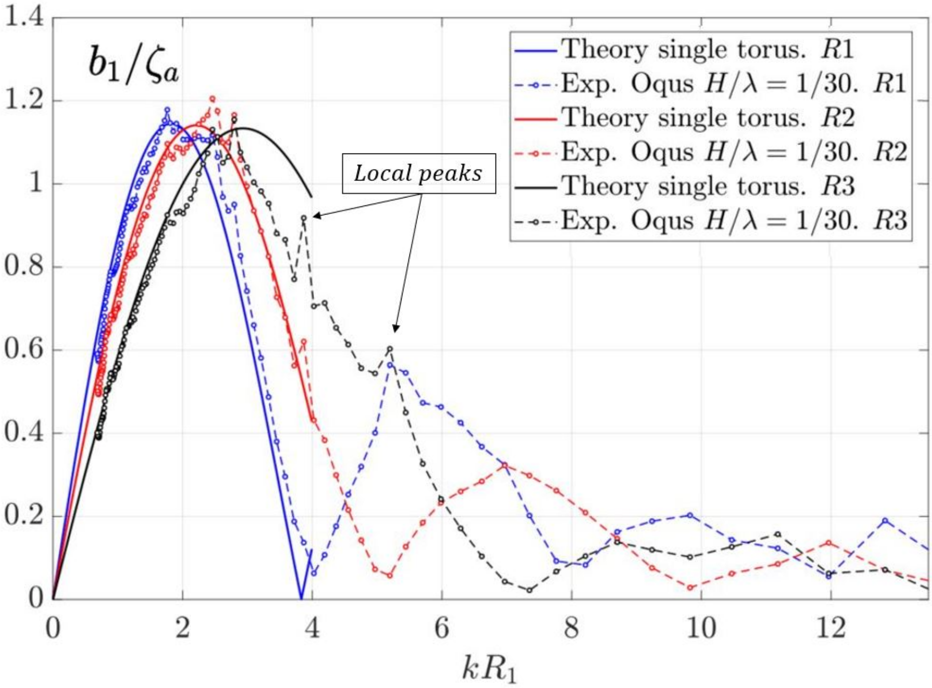

Figure 5.3: RAO in pitch for the three outermost tori. Comparison between theory and experimental results. Figure from Windsvold et al. (2019). Additional comment boxes have later been added.

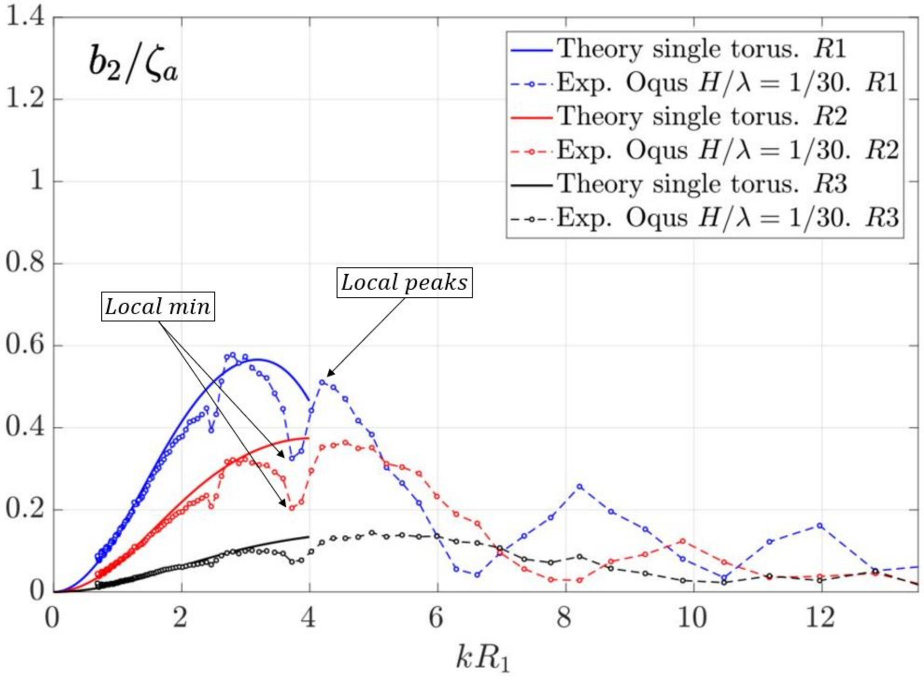

Figure 5.4: RAO in first flexible for the three outermost tori. Comparison between theory and experimental results. Figure from Windsvold et al. (2019). Additional comment boxes have later been added.

From the figures above, we see how the experimental results match ZFT. The experiments match the ZFT quite well for low kR-values. This seems to be the case, regardless of tori and mode. It is, however, observed local peaks and troughs for all three tori and all three modes. Interestingly it is seen from figure 5.2 that tori 2 and 3 have a local peak at $kR \simeq 2.2$. At this point we have cancellation of the response for tori 1. This is seen to happen for $kR \simeq 3.8$. Here torus 3 has cancellation and torus 1, and 2 have a local peak. Similar effects can be seen in figure 5.3 and figure 5.4, where the experiments are deviating from ZFT.

A possible explanation to these disturbances can be due to structural interactions between the tori, as they are connected to each-other through elastic bands. As ZFT only considers a single floater, effects of other tori present are not taken into account. It might also be that the hydrodynamic interactions between the tori have a significant influence on the response of the floater.

Lastly, it must be mentioned that experiments always have sources of error. One that might prove significant is the wall effect of the wave tank. P. Li, 2017 studied the wall effect of a wider tank (*MC-lab*) and found there to be some wave radiations near the wall. These were, however, considered to be small in amplitude and strongly frequency-dependent. The distance between the model and tank wall in *Lilletanken* is about half of that of the experiment done in the *MC-lab*. One can imagine the possibility of waves reflecting from the wall and thus influencing the response of the model. The magnitude of this effect will not be quantified for the present study.

Results for the same modes are also found from Sigstad (2019). The data have been gathered and plotted again.

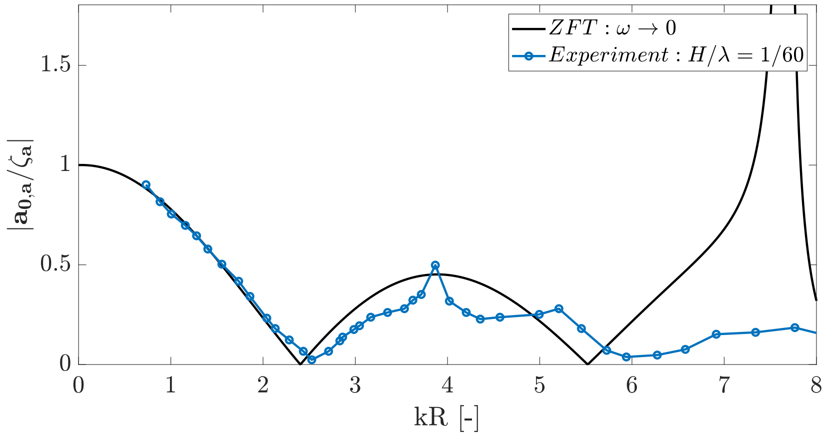

Figure 5.5: RAO in heave for the outermost tori. Comparison between theory and experimental results. Data points are gathered from Sigstad (2019)

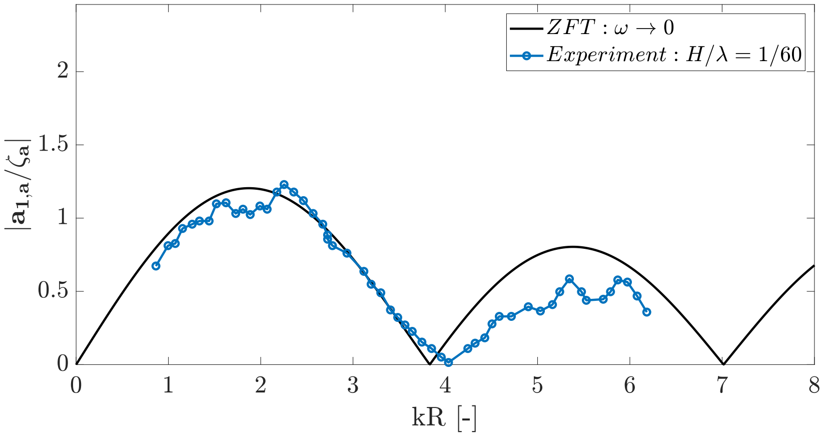

Figure 5.6: RAO in pitch for the outermost tori. Comparison between theory and experimental results. Data points are gathered from Sigstad (2019)

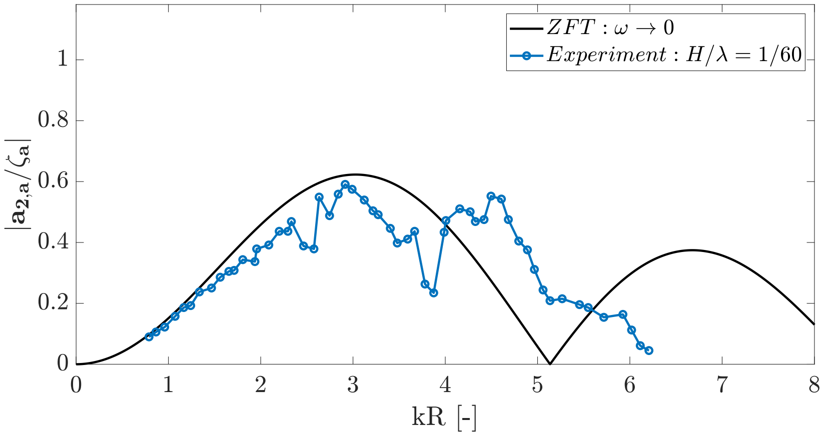

Figure 5.7: RAO in first flexible for the outermost tori. Comparison between theory and experimental results. Data points are gathered from Sigstad (2019)

The overall comparison of the results from Windsvold et al. (2019) and Sigstad (2019) indicate that there are differences between the experiments and ZFT. Both experiments have the peaks and troughs at the same time, which clearly implies that both models are influenced by the same effects. The following results are from the implemented solar island model.

5.2 RAO for two- and 5-tori model

This section presents the results of the two cases tested for the full solar island model. Table 5.3 presents the relevant parameters used for the specific cases. The RAO for different modes are presented, and some are compared to show similarities and differences. Additional results and plots are given in appendix D. Further, the trends in the RAO are discussed along with computed wave forces, stiffness forces, truss forces and damping forces on the floater. These are found for selective kR values. An illustration of the different system can be seen in figure 5.8 and figure 5.9 below.

Table 5.3: Parameters used for the different cases. N_{tori} gives the number of tori. kR is the non-dimensional wave number with wave number k and R being the radius of the outer tori. N_{ramp} is the number of wave periods used for the ramping sequence, and t_{end} is the end-time defined by number of wave periods.

Case	N_{tori} $[-]$	kR_5 $[-]$	H/λ $[-]$	k_t $[N/m]$	$T_{p,t}$ $[N]$	Δt $[s]$	ξ_{damp} $[\%]$	N_{ramp} $[-]$	t_{end} $\cdot T_w[s]$
1	2	[0.3-10]	1/200	$148.4 \cdot 10^3$	37100	0.0025	3	10	30
2	5	[0.3-10]	1/200	$148.4 \cdot 10^3$	37100	0.0025	3	10	30

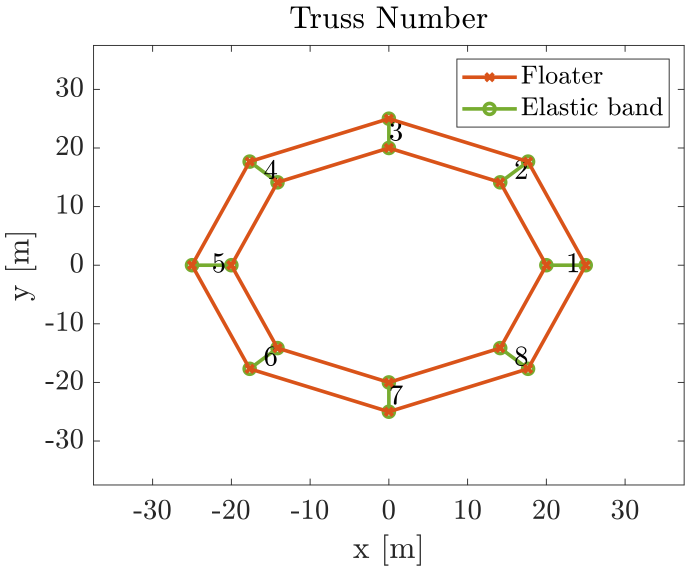

Figure 5.8: Illustration of the model for the 2-tori case with 8 elastic bands, numbering the trusses. Torus(orange) and elastic bands(green) that are modelled by trusses.

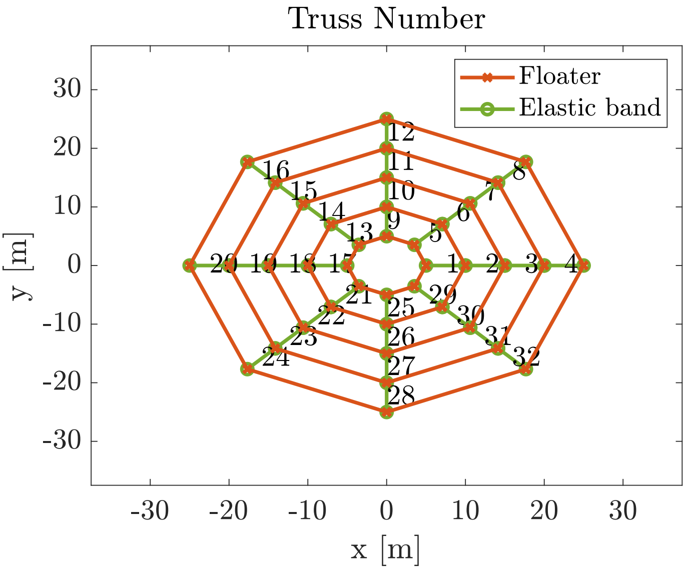

Figure 5.9: Illustration of the model for the five-tori case with 8 elastic bands, numbering the trusses. Torus(orange) and elastic bands(green) that are modelled by trusses.

5.3 Case 1: two-tori

The RAO for the inner and outer torus are presented in the same plot for comparison.

5.3.1 Vertical modes

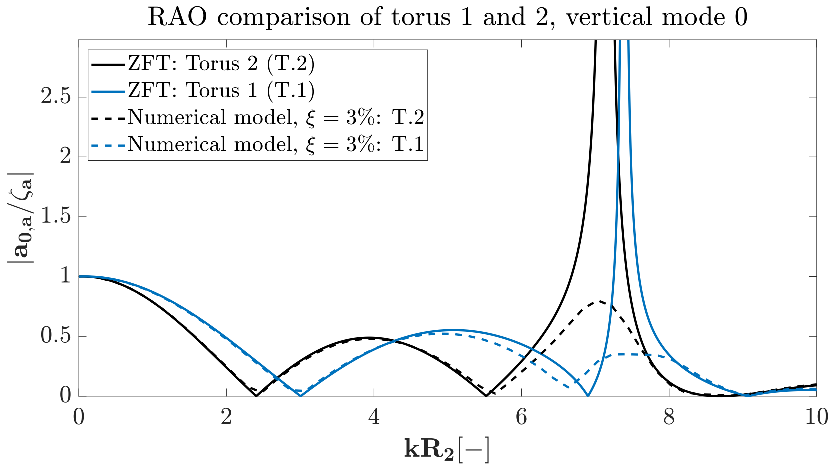

Figure 5.10: RAO for heave of the inner(left) and outer torus(right)

In heave, it is seen that the two-tori case follows the ZFT perfectly for both tori up to $kR \simeq 5$. The outer torus is seen only to be affected by its damping, ref figure 4.7. As for the inner torus, a slight shift to the left is observed for $kR \geq 5$.

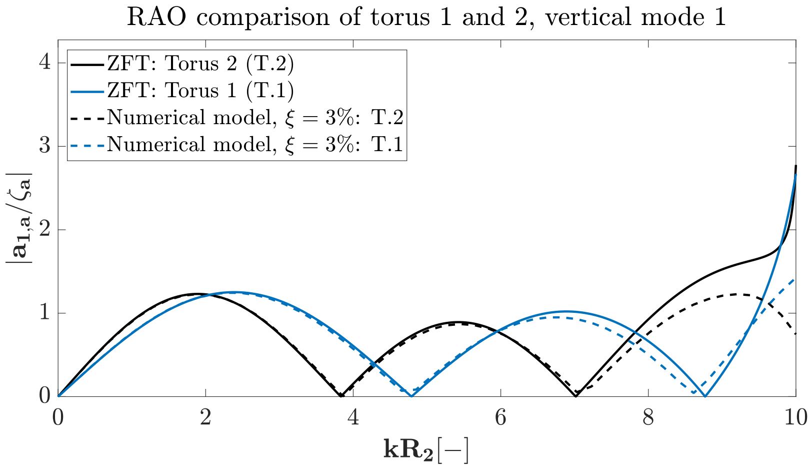

Figure 5.11: RAO for pitch of the inner(blue) and outer(black) torus. Numerical model with $\xi = 3\%$

A similar trend, as for heave, can be seen for the pitch mode. The outer tori experience a strong damping around $kR \simeq 9$. This is to be expected as $kR_n \approx 10$. As for heave, the inner tori also tends to shift towards the left after $kR \simeq 6.2$. The shift is towards the RAO of the outer tori, and may imply that there are structural interactions between the tori which is more present at higher kR. The possible interaction can make the inner torus more influenced by the motion of the outer torus. This can be due to the larger size of the outer torus. Another reason might be that the damping of the tori when connected are stronger than for the single torus.

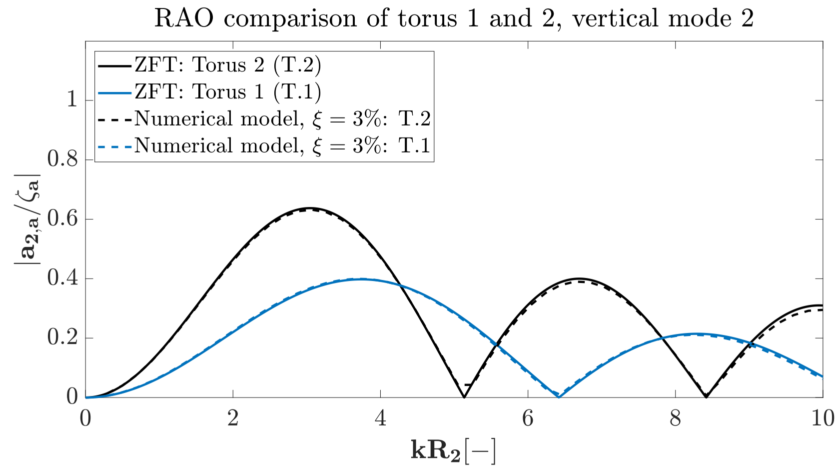

Figure 5.12: RAO for first flexible vertical of the inner(blue) and outer(black) torus. Numerical model with $\xi = 3\%$

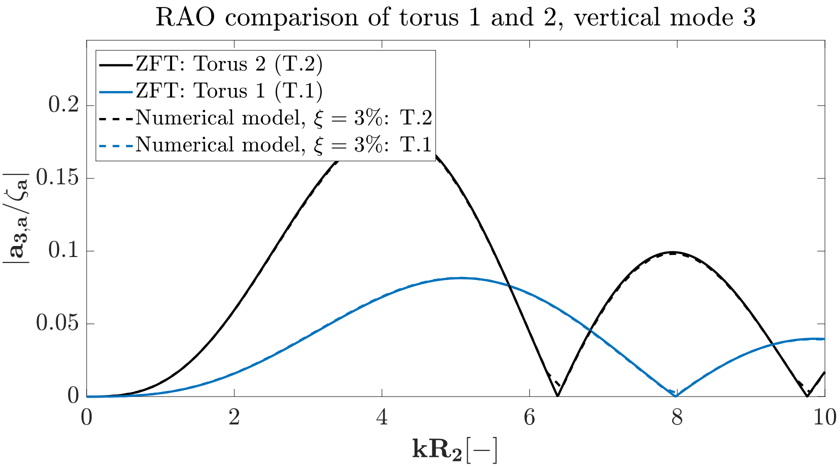

Figure 5.13: RAO for second flexible vertical of the inner(blue) and outer(black) torus. Numerical model with $\xi = 3\%$

Figure 5.12 and figure 5.13 show the RAO for first and second flexible vertical mode of the inner and outer torus, respectively. The numerical model is seen to fit ZFT mor or less perfectly for all kR in the presented range.

5.3.2 Radial modes

The first and second flexible radial mode is presented below for the two-tori.

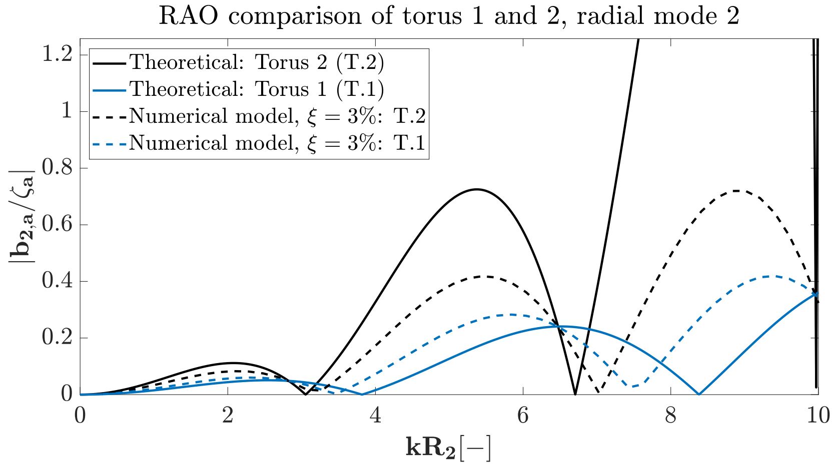

Figure 5.14: Comparison of the RAO for first flexible radial mode of the inner(blue) and outer(black) torus. Numerical model with $\xi = 3\%$

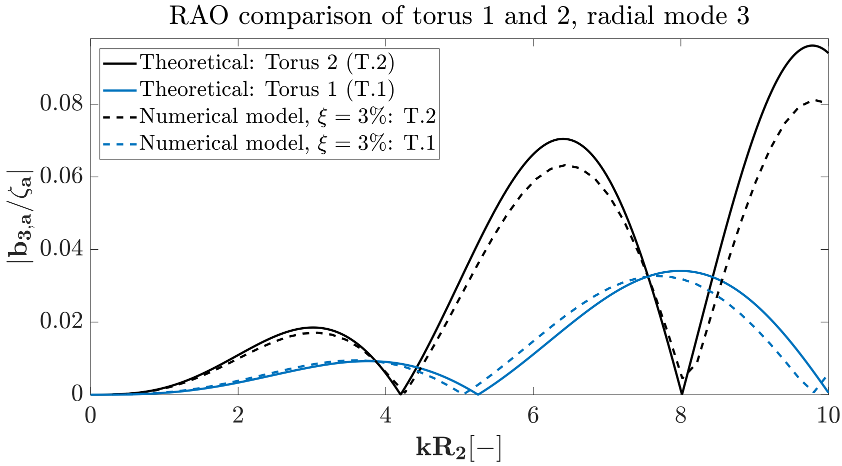

Figure 5.15: Comparison of the RAO for second flexible radial mode of the inner(blue) and outer(black) torus. Numerical model with $\xi = 3\%$

Figure 5.14 and figure 5.15 clearly show the deviation from the theoretical RAO for both torus, and more present for the first flexible mode. The deviation starts after the first cancellation at about $kR \simeq 3.5$. The outer torus experiences a reduced response and a little shift, while the response is more or less unchanged for the inner torus, though there is a shift to the left. For the second flexible, only a small reduction in response is observed for the outer torus, and a small shift to the left for the inner torus.

5.3.3 Surge

The RAO in surge is plotted for the outer torus and compared with the inner torus. The surge motion of the floater has been damped based on mooring-line properties given by Sigstad (2019) in table 5.2.

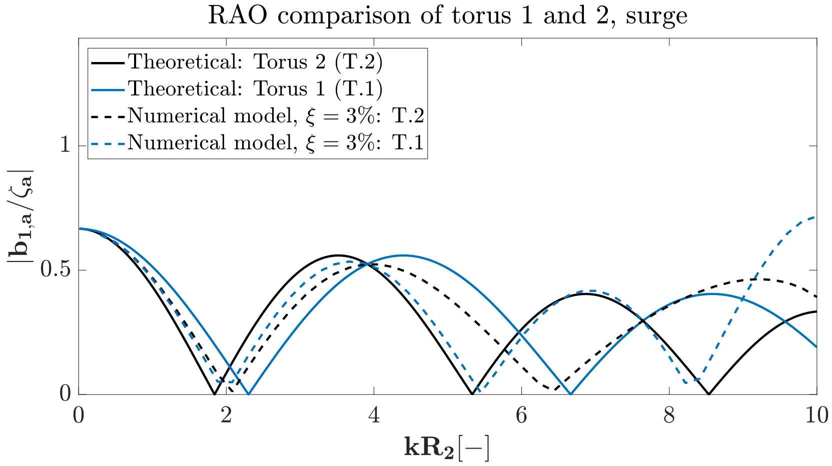

Figure 5.16: Comparison of the RAO in surge for the inner(blue) and outer(black) torus. Numerical model with $\xi = 3\%$

The results show that the surge motion of torus 2 has a strong deviation from theory after the first cancellation at $kR \simeq 2$. The shift is towards the right, with an increase in peak response after $kR \simeq 9$. From comparison of torus 1 and 2, the response of torus 1 shifts towards the left after $kR \simeq 1.8$. Interestingly, at $kR \simeq 3.8$ both tori experience a response peak, which can indicate that both tori move together. This can be understood by the fact that for both radial modes, the response is close to zero for both tori. Thus surge is the dominating lateral motion. These findings can suggest that there are in fact, structural interactions between the tori which are causing this deviation.

5.3.4 Time-serie study, $kR = 8$

The truss forces acting on each torus are studied. These are given along with the generalised wave force, stiffness and damping force for each torus and each mode. Looking at the time-series of the tension in the elastic bands, we want to check how the tension develops over time. It is observed that the diagonal trusses are the ones with the most unstable oscillations for two tori. Truss 2 is plotted, along with the forces in surge. $kR = 8$ is chosen as the torus are observed to have significant deviations from theoretical RAO for both modes.

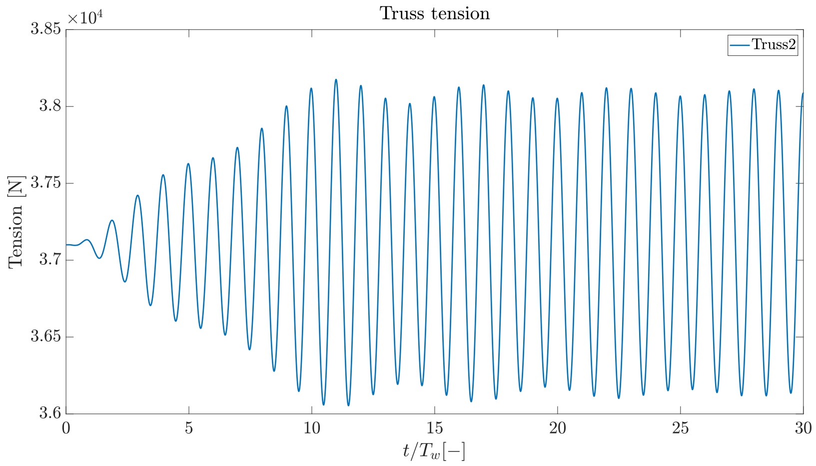

Figure 5.17: Time series for $kR = 8$ for heave the heave mode of torus 1. $\xi = 3\%$.

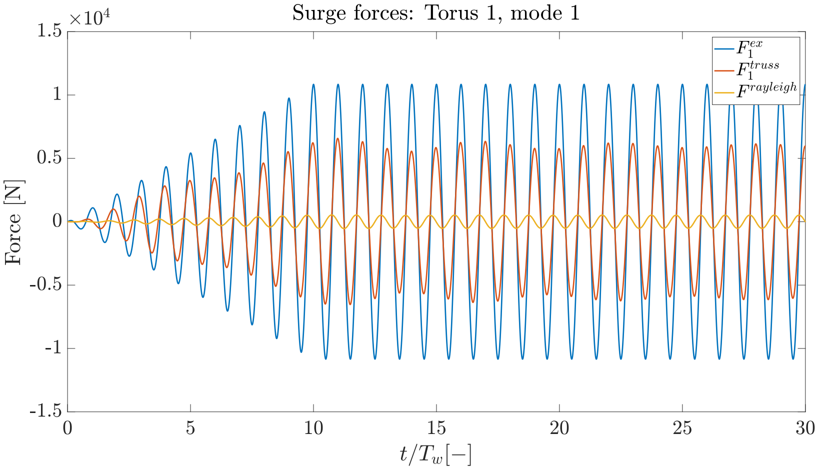

Figure 5.18: Surge forces on torus 1 for $kR = 8$. $\xi = 3\%$. No mooring.

From figure 5.17 the tension is not completely stable after ramping, $t/T_w = 10$. However, there are no sign to deviations from oscillating about pre-tension. The surge forces are stable, and the total truss force on torus 1 is oscillating about the mean value of zero. As the truss forces are stable, it can thus be suggested that the deviation in figure 5.16 is of structural nature.

It is observed that vertical mode 3 for torus 1 have a truss force, which after $t/T_w \approx 10$, follows a linearly increasing value of oscillation. The same is observed for the stiffness force but with a linearly decrease, see figure 5.19.

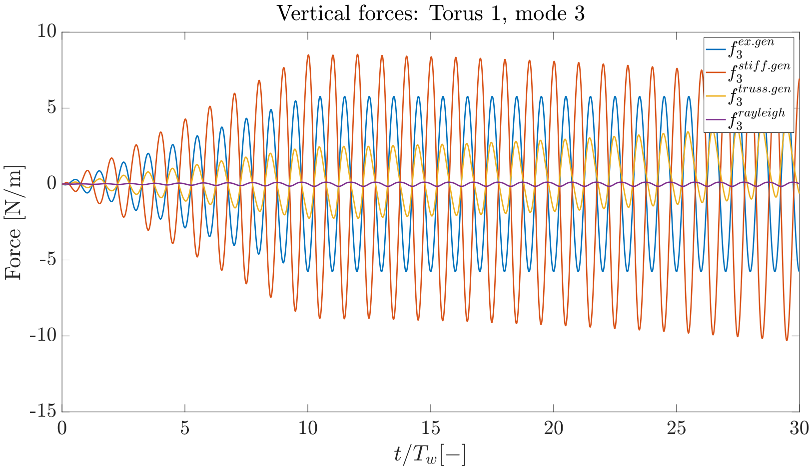

Figure 5.19: Second flexible vertical mode forces on torus 1 for $kR = 8$. $\xi = 3\%$. No mooring.

It is unclear what causes this deviation as there is no obvious sign observed from the RAO, ref figure 5.13. From the magnitude of the force, it can be discussed whether it will greatly affect the response of the tori. By comparison, surge creates a truss force oscillating about $\approx 100N$, compared to vertical mode 3 having an oscillating truss force reaching $\approx 5N$ at $t/T_w = 30$.

5.4 Case 2: five-tori case, full solar island model.

The full solar island model is tested for a wave period $T_w = 8s$, to see its behaviour in long waves, where ZFT is valid. The properties are that of Case 2 in table 5.3.

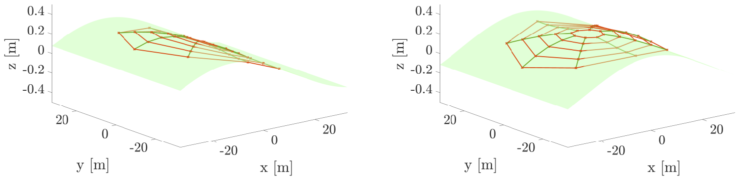

(a) $t + \frac{1}{8}T_w$ **(b)** $t + \frac{2}{8}T_w$

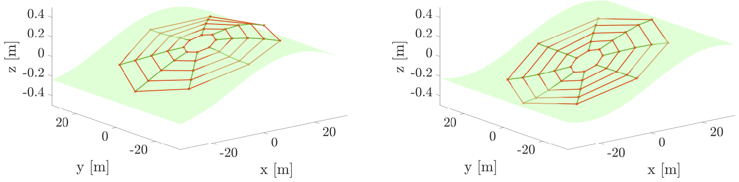

(c) $t + \frac{3}{8}T_w$ **(d)** $t + \frac{4}{8}T_w$

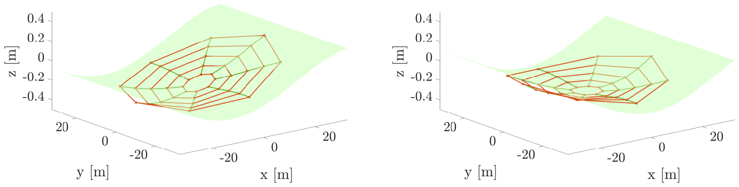

(e) $t + \frac{5}{8}T_w$ **(f)** $t + \frac{6}{8}T_w$

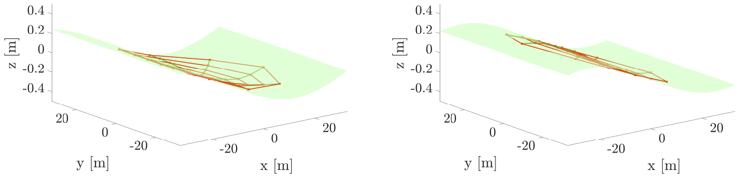

(g) $t + \frac{7}{8}T_w$ **(h)** $t + \frac{8}{8}T_w$

Figure 5.20: Plot of full solar island, with incident wave of $T_w = 8s$, $H/\lambda = 1/200$. Orange lines are drawn between floater nodes on the same torus to illustrate the torus. Green lines are drawn between floater nodes on different tori but same direction in (x, y) space. Transparent green, represent a sinusoidal incident wave with $\zeta_a = 0.25m$.

Figure 5.20 show that the floater follows the wave quite accurate. Appendix D.4 illustrates the movement for a lower wave period, $T_w = 3s$. The five-tori case represent the full solar island model. Results are given for the three first vertical modes, surge and the first radial mode. The model is damped in surge by considering the Rayleigh damping. As there are no mooring, a choice has still been to use the mooring-line stiffness of that of Sigstad (2019), ref table 5.2. With the relation given by O. M Faltinsen (1990), the stiffness term is $2k_m$ and the mass and added mass is considered for the whole structure. A comparison of the RAO in surge without damping of the surge motion is also given. Additional results for five-tori model are found in appendix D.2 and appendix D.3.

5.4.1 Vertical and radial modes

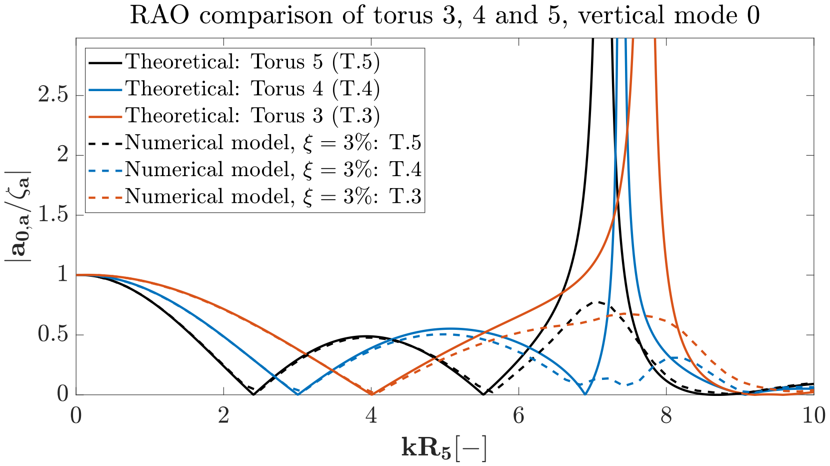

Figure 5.21: RAO for heave for torus three(orange), four(blue) and five(black)

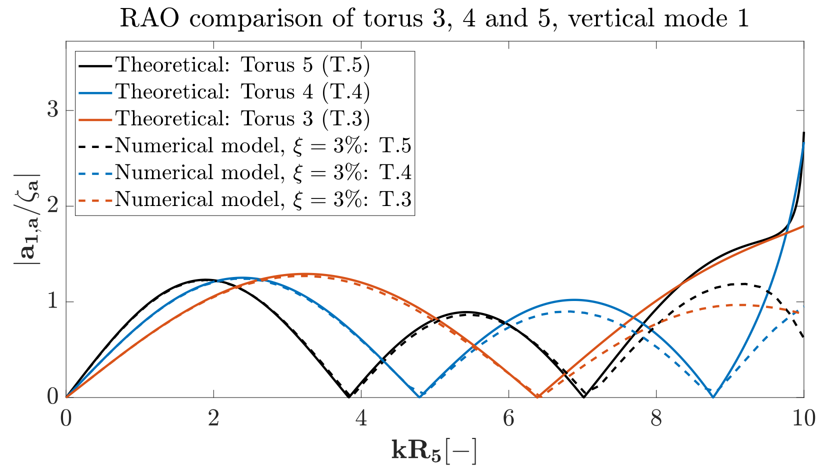

Figure 5.22: RAO for pitch for torus three(orange), four(blue) and five(black)

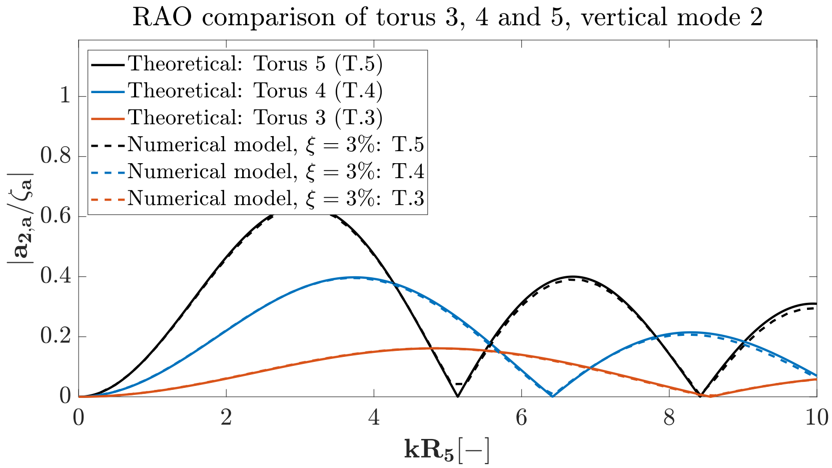

Figure 5.23: RAO for first flexible vertical mode for torus three(orange), four(blue) and five(black)

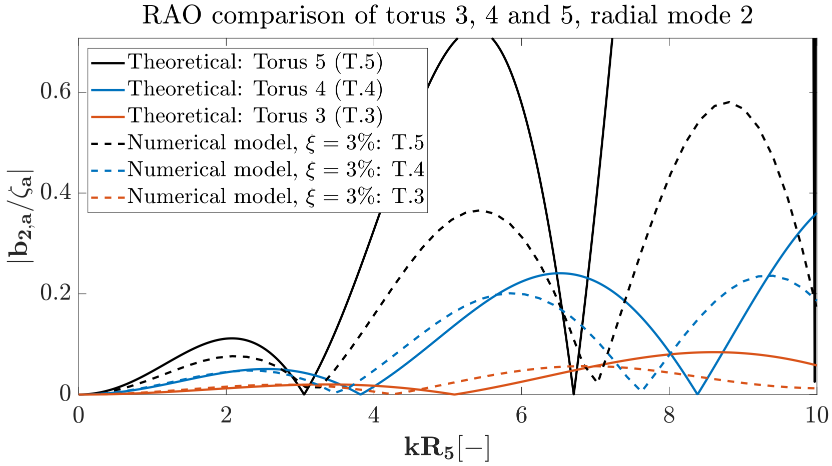

Figure 5.24: RAO for first flexible radial mode for torus three(orange), four(blue) and five(black)

Figures above show the comparison between the three outermost tori. There are obvious similarities to that of the two-tori case. For heave, torus three and four can be seen to deviate from ZFT at $kR > 4.5$. The response for torus four are more damped than torus one in the prior case. Torus three is also seen to be influenced by the damping. Again it is not known whether structural interaction or damping is the leading cause of this deviation. Comparing the above results with experimental results in section 5.1, the deviations to theory observed for the numerical model are not in agreement to that of the experiments.

The first flexible vertical mode is close to identical to ZFT for the whole kR-range. It is in accordance to the two-tori case. Further, it is seen from the first flexible radial mode that torus five is strongly damped and shifted towards the right, while torus three and four are slightly damped, shifted to the left. One interesting finding is that the shift in response leads to the peaks of the different tori to move towards a common kR.

5.4.2 Surge

The RAO in surge are plotted for the three outermost tori, for two cases; with and without damping of the surge mode.

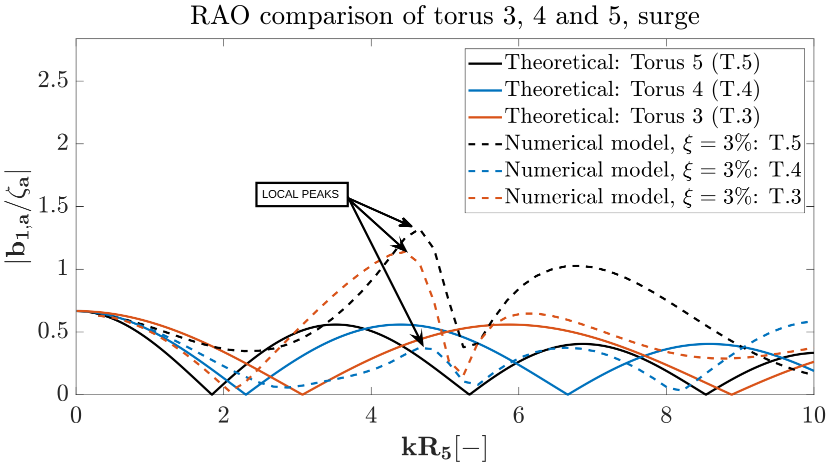

Figure 5.25: RAO for surge for torus three(orange), four(blue) and five(black). Arrows show local peaks in the RAO. No mooring. Damping in surge. $H/\lambda = 1/200$.

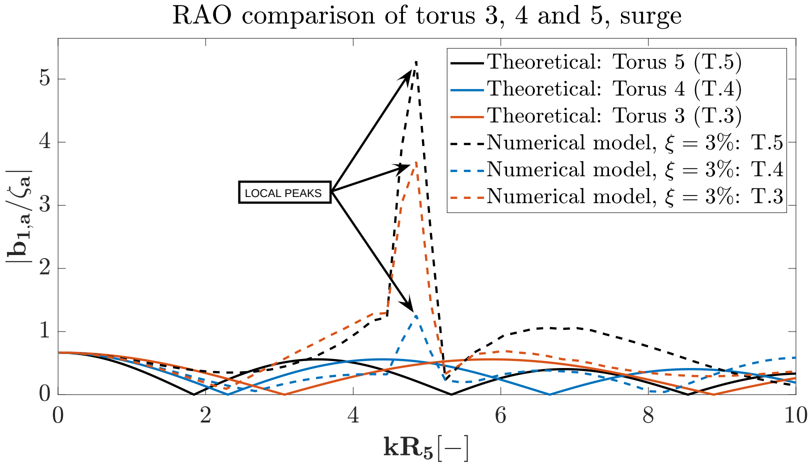

Figure 5.26: RAO for surge for torus three(orange), four(blue) and five(black). Arrows show local peaks in the RAO. No mooring. No damping in surge. $H/\lambda = 1/200$.

Similarly to that of the two-tori case, surge is seen to deviate greatly from the theoretical RAO. Already at low kR, torus five deviates from theory. At theoretical cancellation, $kR_5 \approx 1.8$, the numerical model find $|b_{1,a}/\zeta_a| \simeq 0.45$. Torus four shifts to the right while torus three shifts towards the left, when compared to theory. For all tori a resonance peak is observed at $kR \simeq 4.6$. A more distinct resonance peak is observed when damping of surge motion is not included. The peak are all located at $kR \simeq 5$, and is also observed for the two innermost tori, ref appendix D.2. For both higher and lower kR, the damping seems to have little effect on the overall response for each torus.

5.4.3 Time-serie study, $kR = 5$

A time-serie of $kR = 5$ have been studied. The surge force for torus one is given in figure 5.27. The tension force of truss 9, connected between torus one and two is given in figure 5.28 and the first flexible vertical force of torus one is given in figure 5.29.

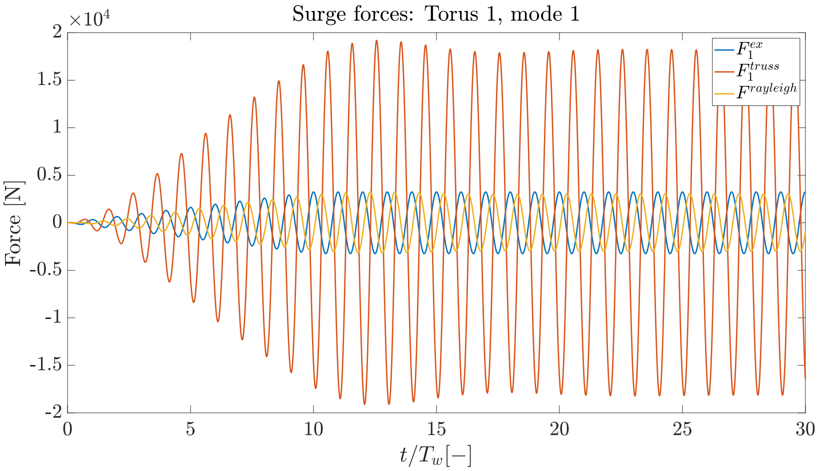

Figure 5.27: Surge forces on torus 1 for $kR = 5$. $\xi = 3\%$. No mooring. F_1^{exc}(blue), F_1^{truss}(orange) and $F_1^{rayleigh}$(yellow).

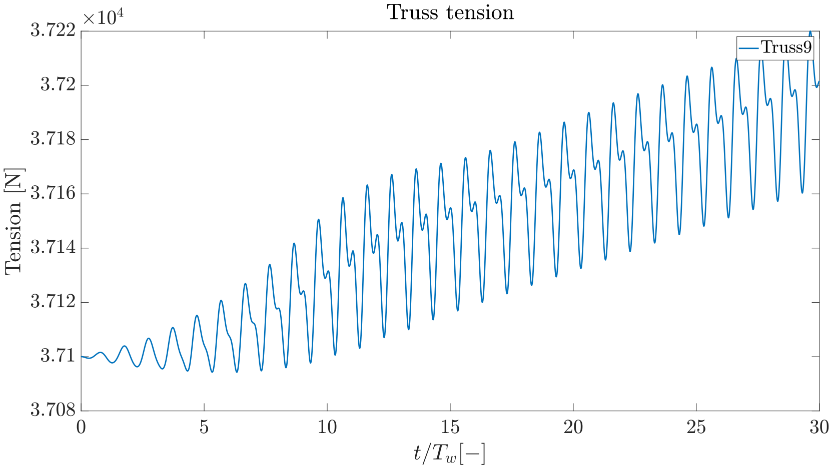

Figure 5.28: Tension force on truss 9 for $kR = 5$. $\xi = 3\%$. No mooring.

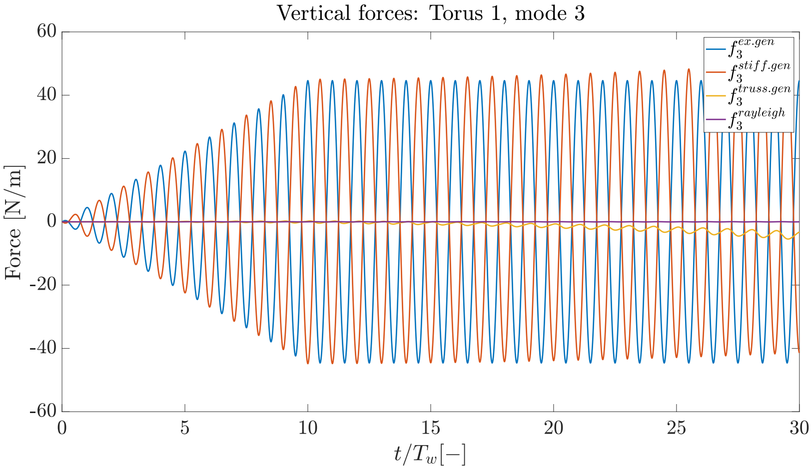

Figure 5.29: First flexible vertical forces on torus 1 for $kR = 5$. $\xi = 3\%$. No mooring. f_3^{exc}(blue), f_3^{stiff}(orange), f_3^{truss}(yellow) and $f_3^{rayleigh}$(purple).

From the surge forces, we can see that the main contributing forces on the torus are from the trusses. It is about 500% larger than the wave forces and damping forces from Rayleigh damping. In general the oscillation are seen to be stable after $t/T_w \simeq 17$.

The tension in truss 9 show a surprising result. With increasing time, the oscillation in the tension is seen to follow a linear trend. Such deviation is not wanted, and will have a negative impact on the result if being too large. For all trusses in the system, it is found that only truss 9, 10, 25 and 26 have this trend. From figure 5.9 these trusses are seen to lay on the y-axis, being perpendicular to the direction of the incident wave. A possible explanation is that these trusses experiences large surge motions in the $x-$direction as well as radial motions in the y-direction.

Figure 5.29 show that the truss forces for the first flexible vertical mode deviates, from mean oscillation about zero, and approach a negative value of oscillation. The stiffness force can, in turn, be seen to deviate and approach a positive value of oscillation. However, looking at the similar forces on the other tori, there are no significant deviations. Nor considering the tension in the trusses. It should be mentioned that the magnitude of the surge forces are in general, dominating for the present kR. None of which are seen to deviate from oscillation about zero.

Based on these results, it is believed that the linearly increasing tension observed for the two inner trusses, parallel to the y-direction, does not explain the significant peaks and deviations in the surge RAO for $kR = 5$, ref figure 5.25 and figure 5.26. The peak is believed to be due to a global resonance occurring between the tori. This is in accordance with the results found from the effect of including damping to the system, in the verification study. An increase in damping is expected to be most prominent at resonance. We have not been able to calculate this resonance theoretically, and it is unsure what exactly causes this. However, the elastic bands are the most likely source. No natural frequency of the modes correspond to the $kR = 5$. Thus structural interaction can not be excluded.

To summarise, the deviations can be due to structural interactions, but are, however, not in good agreement with those of the experiment. A possible explanation for the difference can be the modelling of the trusses. The numerical model only considers the elastic bands to be made up by one single truss. In reality, these are supposed to be elastic bands and be able to hang freely. The simplification of modelling these elastic bands might be wrong. Appendix E presents a test performed for the elastic bands used in the model of Sigstad (2019). It is believed that the bands have strong non-linear elastic effects.

5.5 Errors in numerical model

Several error sources can occur during the implementation of a code; wrong sign for equations, to large time-step, or an error of coding. As Hooke's law models the elastic bands we would expect them to oscillate about pre-tension value. However, it is observed that for the five-tori case, the elastic bands connected to the inner torus tends to oscillate about a linearly increasing line.

With successful verification of the trusses during the project thesis, and thorough debugging of the code, it is believed that the error might be a numerical error. This error can be of such kind that it is added to the tension. For some cases, the tension during ramping is seen to be increasing non-linearly. A possible reason for the error in tension is that this non-linear increase excites the tension and thus leading it not to stabilise, ref figure 5.28

The debug of the code has been a central part of finding the error source. There have not been found any obvious error from the coding point of view, considering the implementation of theory. It is, however, possible that the theory has been derived wrongly, although the procedure has been repeated several times. Another important fact is the observation done during the verification study. It was seen that the simplified method for calculating the truss integral might not be good enough, and lead to a wrong representation of the trusses in the model.

Although experiencing errors from the numerical model, it is not considered to be a reason for discard the created model. As the comparison between the forces show, it is not believed that these errors have too significant impact. It should, however, be studied further, and other methods for modelling the trusses might prove successful. Nonetheless, the numerical model that has been implemented can in general be considered a success.

5.6 Hydrodynamic Interaction

The hydrodynamic interaction have been tested for the three lowest modes of the full five-tori model. The floater properties are the same as for Sigstad (2019), using the full-scale values. The radii of the tori are $R_1 = 5m$, $R_2 = 10m$, $R_3 = 15m$, $R_4 = 20m$ and $R_5 = 25m$. The ratio of the cross-sectional of a torus and the distance between two tori are $p/c = 3.125$. Mooring-lines are ignored as well as elastic bands connecting the tori.

The three lowest vertical RAO for the outermost torus, torus 5, are plotted against the RAO based on ZFT.

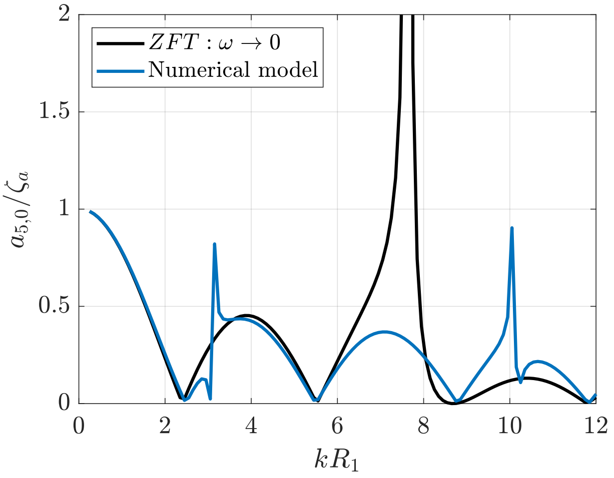

Figure 5.30: Heave mode RAO of the outer torus 5 as predicted by the presented theory (blue), compared with ZFT (black)

Looking at figure 5.30, there are similarities to the experimental results. For $kR < 8$ it is seen that there is a peak at $kR \simeq 3.2$ which is similar to the experiment, $kR \simeq 3.8$. The experiments also have a small peak at $kR \simeq 5.2$, which are not predicted in the presented theory. For higher kR, $kR \geq 8$, the experiments seems to deviate more strongly from the ZFT. One should keep in mind that large experimental errors might occur. This range is thus of less interest for comparison.

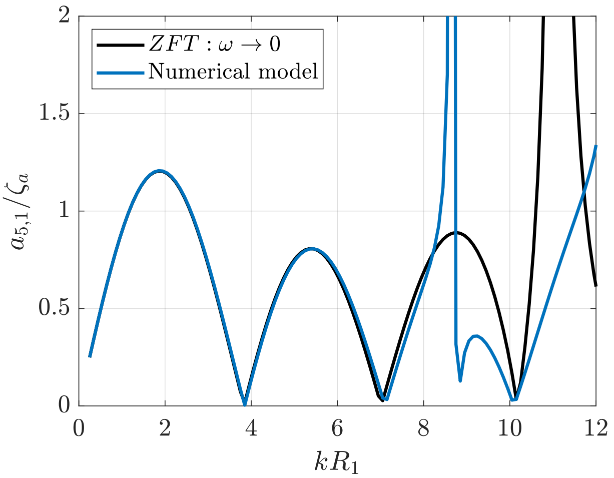

Figure 5.31: Pitch mode RAO of the outer torus 5 as predicted by the presented theory (blue), compared with ZFT (black)

For pitch, the presented theory shows good agreement with ZFT, up to $kR = 8.$, indicating no significant influence of hydrodynamic interactions between tori. Both experiments have several local peaks in the range $kR = 2$ and $kR = 6$. None of these are present in figure 5.31. The experimental results deviate from ZFT already after the first cancellation, $kR \simeq 4.1$.

Figure 5.32 show a positive match between the proposed theory and ZFT. Only small deviations are seen for $kR < 8$. Compared to the experiment, there are no obvious irregularities.

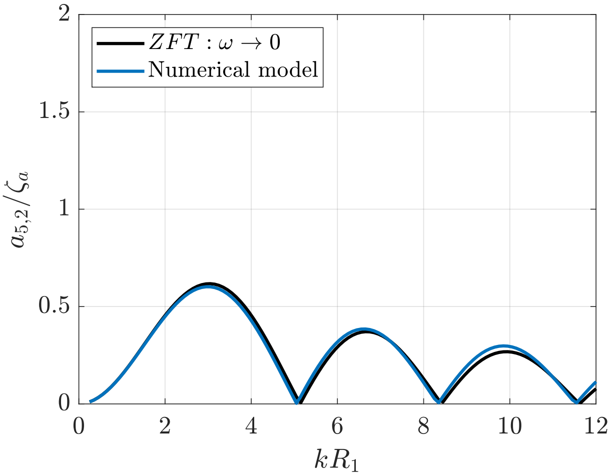

Figure 5.32: First flexible mode RAO of the outer torus 5 as predicted by the presented theory (blue), compared with ZFT (black)

A possible explanation of the differences between the presented theory and experiments can be that there are other more prominent effects dominating the behaviour of the system, like that of structural interaction. The theory for hydrodynamic interactions is based on ZFT and assumes zero wave radiated damping. It can be seen that the approximation is suitable for small kR values, but might be too coarse of an estimate with increasing kR. Thus these effects may be more present for higher kR. However, it is not believed to be the primary source for the difference between experiments and ZFT.

Chapter 6

Conclusion & Recommendations for further work

A semi-submerged multi-torus model is numerically implemented to investigate the response of such structure. The model is successfully generalised to take any number of tori, and elastic band. The verification study show promising results for each motion of a single-torus, indicating correct implementation.

The experimental results obtained by Sigstad (2019) and Windsvold et al. (2019) show in general good agreement with ZFT for the low range of kR. Both experiments show similar deviations from ZFT at higher kR. From the numerical model created, cases with two- and five-tori have been tested. The resulting RAOs show deviations from ZFT for the inner tori, while the outermost torus follows the ZFT for most vertical modes.

Interestingly, the five-tori model show that the deviation seems to be stronger for the innermost torus. Radial motions, including surge, are found to be the ones with significant deviations. With a perfectly horizontal mooring configuration, it is reasonable to believe that these motions are subjected to the largest tension. By studying the generalised forces of the system for different kR values, it is believed that the deviations can partly be explained by structural interactions between the tori through the elastic bands. It has been discovered that the numerical model experiences a linear type of increase in tension of the elastic bands.

The presented theory for calculating the RAO when only considering hydrodynamic interactions, does not alone explain the irregularities seen from the experiment. Although showing effects to some extent, it is not believed to be the main contributor to the difference in response. It is thus not believed that the strong irregularities between theory and experiment is due to hydrodynamic interactions alone, but might be due to an increase in experimental error with increasing kR.

Neither structural- or hydrodynamic interactions found by the numerical model, answer the deviation between theory and experiment. As found in the laboratory test, ref. appendix E, it was seen that the elastic bands from the experiment did not behave according to Hooke's law, and might not be well represented by the use of the modelled trusses.

The effect of the error present in the numerical code is uncertain. Countless tries were done to resolve, but without luck. Nonetheless, the overall numerical implementation of the model is considered a success. Further work is required to develop the model further, and possibly resolve the bug.

6.1 Recommendations for further work

Based on the experimental work done by the previous students and the present work, the following recommendations for further work can be summarised as:

- Sigstad (2019) mention that additional work is needed to be done with the experiment to investigate several phenomena, like over-topping and mooring-line dependency. Another important topic might be to investigate the wall effects in the experiments. Further experimental study might give new answers to the deviations in response compared to theory.
- For the present study, the numerical model should further be generalised to specify parameters to given tori. It is believed that a larger cross-sectional diameter of the outer torus is beneficial in terms of stability of the structure.
- A parametric study can give indications on the optimal structure. This is of great interest in order to realise the concept. The membrane deck, intended to support the solar panels, can be modelled by the use of trusses. These can be attached in a cross-way manner between the floaters to simulate a flexible upper deck.
- Last but most important. The error observed from the numerical model should be investigated further. The following students should investigate different ways of defining the truss forces acting on the tori. As the present combined floater-truss model is rather complex, supervisor Prof. Kristiansen has suggested a pragmatic way of including the truss forces. This may simplify the model and prove to be successful. Appendix A.3 briefly describes the proposed way of including these truss forces.

Bibliography

Bruce, D. P. et al. (2019). “Renewable CO2 recycling and synthetic fuel production in a marine environment”. In: *Proceedings of the National Academy of Sciences*.

Debernard, E. (2019). “Numerical investigation of hydrodynamic interactions of a multi-torus in waves”. In: *Research Internship (PRE)*.

Faltinsen, O. M (1990). *Sea loads on ships and offshore structures*. Cambridge ocean technology series. Cambridge: Cambridge University Press.

— (2010). “Current and wave loads on floating fish farms”. In: *CeSOS, UNPUBLISHED*.

— (2011). “Hydrodynamic aspacts of a floating fish farm with circular collar”. In: *CeSOS*.

FCCC (2016). “Report of the Conference of the Parties on its twenty-first session, held in Paris from 30 November to 13 December 2015”. In: *Framework Convention on Climate Change*.

IEA (2019a). *Explore energy data by category, indicator, country or region*. URL: `https://www.iea.org/data-and-statistics/data-tables?country=WORLD&energy=Balances&year=2017` (visited on 12/15/2019).

— (2019b). *Key energy statistics, 2018*. URL: `https://www.iea.org/countries/Norway` (visited on 12/15/2019).

Kristiansen, T. (2012). “Linearized hydroelastic theory of circular floater in ”fishFarm” Fortran code”. In: *Post-Doc, UNPUBLISHED*.

Kristiansen, T. and O. M. Faltinsen (2014). “Experimental and numerical study of an aquaculture net cage with floater in waves and current”. In: *Journal of Fluids and Structures* 54, pp. 1–26.

Larsen, C. M. et al. (2019). “TMR 4128 Marine dynamics (Compendium)”. In: *Department of Marine Technology, NTNU*.

Li, P. (2017). “A Theoretical and Experimental Study of Wave-induced Hydroelastic Response of a Circular Floating Collar”. In:

Li, P and O. M. Faltinsen (2012). “Wave induced response of an elastic circular collar of a floating fish farm”. In: *Proceedings of 10th International Conference on Hydrodynamics* 2, pp. 58–64.

Marichal, D. (2003). “Cod-end numerical study.” In: *Third International Conference on Hydroelasticity in Marine Technology*.

Marino, E., J. Kiendl, and L. De Lorenzis (2019). “Explicit isogeometric collocation for the dynamics of three-dimensional beams undergoing finite motions”. en. In: *Computer Methods in Applied Mechanics and Engineering* 343, pp. 530–549.

Sigstad, M. V. (2019). “A Numerical and Experimental Study of a Multi-torus Floating Solar Island Concept”. In: *Master’s thesis NTNU*.

Windsvold, J. (2018). “An Experimental Study on the Wave-Induced Hydroelastic Response of a Floating Solar Island. Master’s thesis NTNU”. In: *Master’s thesis NTNU*.

Windsvold, J. and J. Kristiansen (2019). “Investigation of a Flexible Multi-torus Solar Island. Draft (not submitted)”. In: *NOT SUBMITTED*.

Appendix A

Additional theory

A.1 Truss length derivation

Single rigid truss

A rigid truss is the purest form of trusses. The idea is that the kinematic constraint of zero elongation is satisfied, i.e. the length is kept constant.

$$l_k^{n+1} = l_k^n \tag{A.1}$$

where l is the length of truss k, and n is the time step.

The length of the truss can further be represented by the nodal positions of node i and j.

$$l_k = ||\mathbf{x}_j - \mathbf{x}_i|| \tag{A.2}$$

where $\vec{x}$ is the three-dimensional (3D) vector of the nodes. Further using equation (A.1) with equation (A.2) and taking its square we get.

$$||\mathbf{x}_j^{n+1} - \mathbf{x}_i^{n+1}||^2 = ||\mathbf{x}_j^n - \mathbf{x}_i^n||^2 \tag{A.3}$$

Inserting the third line of equation (2.8) into the left-hand side(LHS), the expression becomes.

$$\begin{gathered} ||\mathbf{x}_j^n + \Delta t\mathbf{v}_j^n + \Delta t^2\mathbf{a}_j^n - \mathbf{x}_i^n - \Delta t\mathbf{v}_i^n - \Delta t^2\mathbf{a}_i^n||^2 = ||\mathbf{x}_j^n - \mathbf{x}_i^n||^2 \\ ||(\mathbf{x}_j^n - \mathbf{x}_i^n) + \Delta t(\mathbf{v}_j^n - \mathbf{v}_i^n) + \Delta t^2(\mathbf{a}_j^n - \mathbf{a}_i^n)||^2 = l_k^2 \end{gathered} \tag{A.4}$$

The latter expression in equation (A.4) can with change of variables, some algebraic manipulations and remembering the cosine formula for vectors, be simplified to,

$$\begin{aligned}
&||\alpha + \underbrace{\beta + \gamma}_{\tau}||^2 = l_k^2 \\
&||\alpha + \tau||^2 = ||a||^2 + ||\tau||^2 + 2\alpha\tau \\
&\underbrace{||a||^2}_{=l_k^2} + ||\tau||^2 + 2\alpha\tau = l_k^2 \\
&||\beta + \gamma||^2 = -2\alpha\tau \\
&\underbrace{||\beta||^2}_{\mathcal{O}(\Delta t^2)} + \underbrace{||\gamma||^2}_{\mathcal{O}(\Delta t^4)} + \underbrace{2\beta\gamma}_{\mathcal{O}(\Delta t^3)} = - \underbrace{2\alpha\tau}_{\mathcal{O}((\Delta t + \Delta t^2))}
\end{aligned} \tag{A.5}$$

Excluding the term of $\mathcal{O}(\Delta t^4)$ and $\mathcal{O}(\Delta t^3)$, and moving all terms on the RHS, the latter expression of A.4 is given as

$$\Delta t^2 \underbrace{||\mathbf{u}_j^n - \mathbf{v}_i^n||^2}_{b^n} + 2 \underbrace{(\mathbf{x}_j^n - \mathbf{x}_i^n)}_{l_k \mathbf{s}_k}(\Delta t \underbrace{(\mathbf{v}_j^n - \mathbf{v}_i^n)}_{c^n} + \Delta t^2 (\mathbf{a}_j^n - \mathbf{a}_i^n)) = 0 \tag{A.6}$$

Expressing equation (A.6) in terms of the simplified variables given, the equation can be expressed more compact. The acceleration terms are kept on the LHS while the other terms are moved to the right-hand side (RHS).

$$\mathbf{s}_k \cdot (\mathbf{a}_j^n - \mathbf{a}_i^n) = -\frac{b^n}{2l_k} - \frac{1}{\Delta t} c^n \mathbf{s}_k \tag{A.7}$$

Recall that the acceleration can be expressed in terms of gravity and tension.

$$\mathbf{a}_j = \frac{1}{m_j} \sum_l T_{jl} \mathbf{s}_{jl} + \mathbf{g} \tag{A.8}$$

Here l denotes the nodes that are parts of the trusses connected to the node considered. This is done as a node can lie between two trusses and thus have two tension components. Note that **g** depends on the initial conditions of the system.

A.2 Hydrodynamic interactions: near-field approach

As described in chapter 3, the hydrodynamic interaction on a body is due to an induced flow from another body. The flow is nearly horizontal, and no vertical diffraction problem is present. Thus, we only have to find the Frodue-Kriloff load by integrating the induced ambient pressure. The derivation have been initially done by supervisor Prof. Kristiansen (Unpublished).

If we now consider heave motion, the near-field approach gives an outer expansion for the near-field solution of torus j is given by O. M. Faltinsen (2011),

$$\phi_j^N \simeq \dot{a}_{j,0}\Big\{\frac{2c}{\pi}\Big[\log\Big(\frac{8Rj}{r'}\Big)\Big]\Big\} \tag{A.9}$$

This can further be evaluated at the centre-axis of torus k, which is

$$\phi_j^N = \dot{a}_{j,0}\Big\{\frac{2c}{\pi}\Big[\log\Big(\frac{8Rj}{\Delta R}\Big)\Big]\Big\} \tag{A.10}$$

where $\Delta R = |R_j - R_k|$. The ambient pressure on the body is found by the linear term in the Bernoulli equation,

$$p_j = -\rho\frac{\partial \phi_j^N}{\partial t} = -\rho\ddot{a}_{j,0}\frac{2c}{\pi}\Big[\log\Big(\frac{8Rj}{\Delta R}\Big) \tag{A.11}$$

Further, the force per unit length is found by integrating the pressure over the whetted area of torus k,

$$\begin{aligned} f_{k,j} = -\int_{-\frac{\pi}{2}}^{\frac{\pi}{2}} p_j n_z c \mathrm{d}\theta'' &= \rho c\ddot{a}_{j,0}\frac{2c}{\pi}\log\Big(\frac{8Rj}{\Delta R}\Big)\int_{-\frac{\pi}{2}}^{\frac{\pi}{2}}(-\cos(\theta'')\mathrm{d}\theta'' \\ &= -\ddot{a}_{j,0}\frac{4}{\pi}\rho c^2\log\Big(\frac{8R_j}{\Delta R}\Big) \end{aligned} \tag{A.12}$$

$n_z = -\cos(\theta'')$. Integrating over the circumference of torus k we get the heave force,

$$F_{k,j,0} = \int_0^{2\pi} f_{k,j,0}R_k\mathrm{d}\beta = -\ddot{a}_{j,0}\Big[2\pi R_k\frac{4}{\pi}\rho c^2 log(\frac{8R_j}{\Delta R})\Big] \tag{A.13}$$

which in turn gives the heave added mass,

$$A_{k,j,0} = 8R_k\rho c^2\log\Big(\frac{8R_j}{\Delta R}\Big) \tag{A.14}$$

It is interesting to define the non-dimensional added mass. This is used when comparing results in WAMIT, ref Debernard (2019). It is found by dividing the added mass by the structural mass of torus k. Thus we get,

$$\frac{A_{k,j,0}}{M_k} = \frac{8}{\pi^2} \ln\left(\frac{8R_j}{\Delta R}\right) \tag{A.15}$$

A.3 Simplified model for elastic band between tori

The lab test presented in appendix E clearly show that the elastic bands used in the experiment is not well modelled by Hooke's law. The combined model have proved to be complex and sensitive to time-steps, thus leading to motivation for a simplified model. This is based on unpublished notes by Prof. Kristiansen.

We only consider the vertical motions, neglecting all horizontal motions (radial, surge and sway). Furthermore, assuming the elastic bands to obey Hooke's law, ref. equation (2.9), the vertical component of the tension in the elastic band T_z, can be expressed by,

$$T_z(\beta, t) = T_p(w_2(\beta, t) - w_1(\beta, t))^3 \tag{A.16}$$

where T_p is the pre-tension of the elastic band, w_1 and w_2 is the vertical displacement of torus 1 and 2, respectively. An illustration of the system can be seen in figure A.1 and figure A.2.

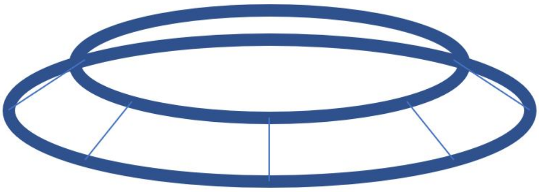

Figure A.1: Illustration of vertical heave motion of two-torus model, connected by elastic bands. Courtesy to Trygve Kristiansen.

Figure A.2: Side view of the vertical tension component of two-torus model, connected by elastic bands. Courtesy to Trygve Kristiansen.

Recalling equation (2.36) we can express the truss forces in terms of the simplified vertical tension component in equation (A.16) as,

$$f_{k,truss} = \sum_{p} \sum_{i=1}^{N_p} T_p(w_p(\beta, t) - w_k(\beta, t))^3 \tag{A.17}$$

where p is the index of the neighbouring torus, $k-1$ or $k+1$. N_p is the number of elastic bands around the floater. We have a non-linear expression for the unknown tensions, due to the cubed terms. Including this into equation (3.13) and multiplying by $\cos(m\beta)$ and integrating from 0 to 2π we get,

$$\begin{aligned} & m_k \ddot{a}_{k,n} + \frac{EI_k}{R_k^4}\left(n^4 - n^2\right) a_{k,n} + 2c_k a_{k,n} \\ & = f_{k,n}^{\text{ex.gen}} + \int_0^{2\pi} \sum_p \sum_{i=1}^{N_p} T_p \left(w_p(\beta,t) - w_k(\beta,t)\right)^3 \cos n\beta \mathrm{d}\beta \\ & - \sum_{j=1}^{K} a_{k,j,n} \ddot{a}_{j,n} \end{aligned} \tag{A.18}$$

Here we need to find a smart way of solving the unknowns. One way would be to use the vertical motions from the previous time-step.

Appendix B

Verification of elastic truss

All studies that are tested are based on the truss model given in equation (A.7). Each case have their own specific value for the variables $A(1,1)$, $A(N,N)$, $B(1,1)$ and $B(N,N)$ based on their boundary conditions. To easier understand which **boundary conditions (BC)** that are used, and what the resulting variables are in the **A**-matrix and b-vector, table B.1 gives the input values for the variables. It is stressed to the reader to use this table when the different cases are presented.

Table B.1: Value for variables in **A**-matrix and b-vector for different BC, for $turss = 1$ and $truss = N_{truss}$

Boundary condition (BC)	A(1,1)	A(N,N)	B(1,1)	B(N,N)
Free	$\frac{1}{m_1} + \frac{1}{m_2}$	$\frac{1}{m_N} + \frac{1}{m_{N+1}}$	0	0
Fixed	$\frac{1}{m_2}$	$\frac{1}{m_N}$	-$\hat{s}_1\vec{g}$	+$\hat{s}_N\vec{g}$
Oscillating	-	-	-$\hat{s}_1(\vec{g} + \vec{a}_1)$	+$\hat{s}_N(\vec{g} + a_{\vec{N}+1})$

Here $(-)$ means that the **A**-matrix is not affected by the **oscillation BC** and thus only given by either **fixed BC** or **free BC**. Factors like pre-tension and equation of oscillation motion are given individually when the cases are presented.

The rigid- and elastic truss model was verified in the project thesis. The following cases show the verification for the elastic trusses. Two cases are presented, being a flexible compound truss horizontally elongated and released and a single vertical truss subjected to a pre-tension before released.

B.1 Flexible compound truss

The flexible compound truss is modelled with the elastic truss model. Marino et al. (2019) performed a test case for a flexible swinging pendulum, using a flexible beam model. Being a flexible beam, it can thus be subjected to shear deformations. This is not the case for the present truss model. The verification is as a comparison of the pendulum motion related to time and the vertical tip deformation. Some deviations are to be expected.

The flexible compound truss is modelled being fixed in node $n = 1$ and free in node $n = N_{truss} + 1$. As mentioned in section 2.1 the tension related terms occurring when including elasticity are included in the system, see equation (2.15). The elasticity and material properties are given in Marino et al. (2019). These properties and the initial conditions are given in table B.2

Table B.2: Material and geometrical properties of flexible compound truss with initial conditions.

Description	Symbol	Value
Number of trusses	nT	30
Total length	l	$1m$
Cross-section diameter	d	$0.01m$
Material density	ρ	$1100kg/m^3$
Youngs modulus	E	$5 \times 10^6 N/m^2$
Spring stiffness	k	$11.8e4kN/m$
Pre-tension	T_p	$0N$
Initial angle	θ_0	$90°$
Time step	Δt	$10^{-5}s$

Results

The flexible compound truss is compared with results from Marino et al. (2019).

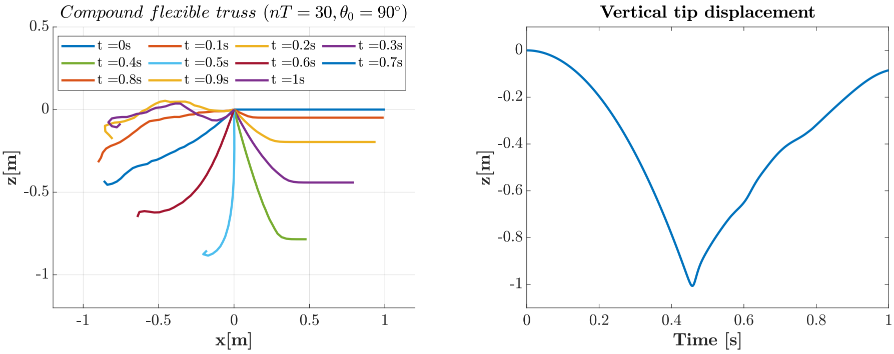

(a) Position is pace in time

(b) Vertical displacement for point mass in time

Figure B.1: Position of flexible compound pendulum, and tip displacement in time with $\theta_0 = 90°$

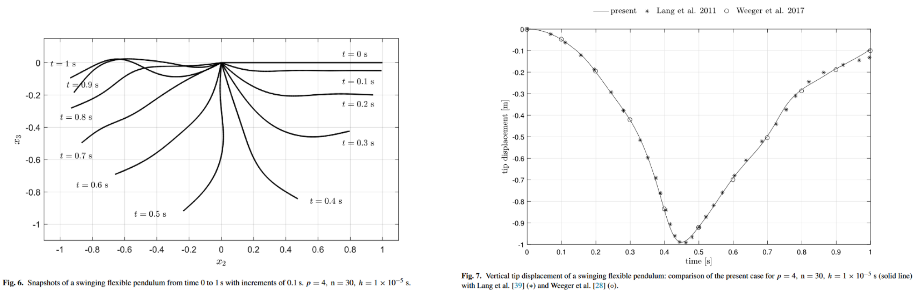

Fig. 6. Snapshots of a swinging flexible pendulum from time 0 to 1 s with increments of 0.1 s. $p = 4$, $n = 30$, $h = 1 \times 10^{-5}$ s.

Fig. 7. Vertical tip displacement of a swinging flexible pendulum: comparison of the present case for $p = 4$, $n = 30$, $h = 1 \times 10^{-5}$ s (solid line) with Lang et al. [39] (∗) and Weeger et al. [28] (○).

(a) Position is pace in time

(b) Vertical displacement for point mass in time

Figure B.2: Position of flexible compound pendulum, and tip displacement in time with $\theta_0 = 90°$. Test case perfomred by Marino et al. (2019).

From the comparison between figure B.1 and figure B.2 the main characteristics as the position in time and the vertical tip displacement can be seen to have strong similarities. Both pendulums have more or less the same trajectory and have similar characteristics at the different time steps plotted. For the truss model, it is seen that the lower part of the truss buckle out as the pendulum passes the lowest point. There are no local deformations seen from figure B.2a. It is due to the difference between the models in terms of having the ability to take shear deformations. As the truss model can not locally bend, such forces are compensated by buckling in the nodes of the trusses. The verification case can bend and thus have a smoother geometry. Besides this, the truss model seems to model the pendulum good, with satisfactory results.

The vertical tip displacement is a good fit. The first 0.6 seconds are close to identical, where there occurs to be a plateau between 0.6 and 0.8 seconds for the elastic truss model. This is in correspondence with the local tip deformations observed in figure B.1a. Both models have the same trend in general, and it seems as though the truss model implemented manages to replicate the results adequately.

B.1.1 Pre-tensioned truss free to oscillate

A pre-tensioned truss is created to test the elasticity of the truss model. The single truss is fixed in node $n = 1$, hanging vertically down, pre-tensioned then released. Figure B.3 illustrates the system.

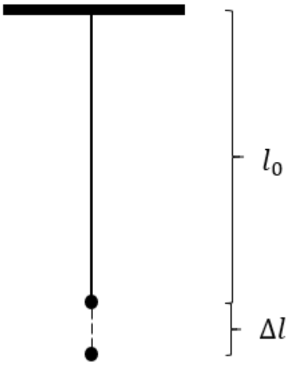

Figure B.3: Illustration of the single pre-tensioned truss

The geometric and material properties, as well as the initial conditions, are given in table B.3.

Table B.3: Material and geometrical properties of flexible compound truss with initial conditions.

Description	Symbol	Value
Number of trusses	nT	1
Original length	l_0	$1m$
Mass	m	$1kg$
Spring stiffness	k	$1000N/m$
Pre-tension	T_p	$105N$
Initial angle	θ_0	0°
Time step	Δt	$[10^{-3}s,\ 10^{-4}s,\ 10^{5}s\ 10^{-6}s]$

The pre-tension is specified as $T_p = mg - k\Delta l$. This elastic truss will be able to take compression since the elasticity truss model is still a rigid truss only able to elongate in one direction. As mentioned, the model was created using the theory of Hook's law. For more trusses, negative compression in truss elements leads to buckling.

Results

The purpose of the pre-tensioned single truss case was to check the stability of the elastic truss model. For constant pre-tension, four different time steps were tested and compared.

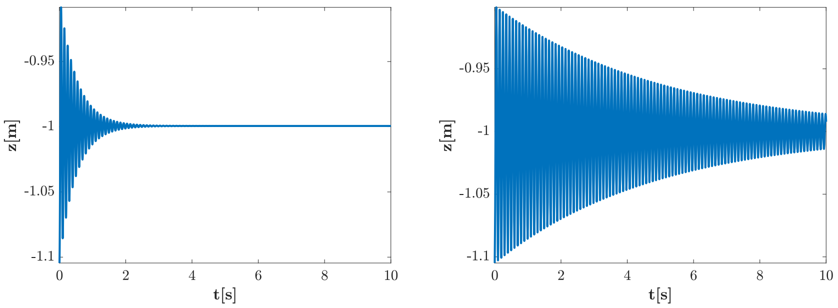

(a) $\Delta t = 0.001s$ **(b)** $\Delta t = 0.0001s$

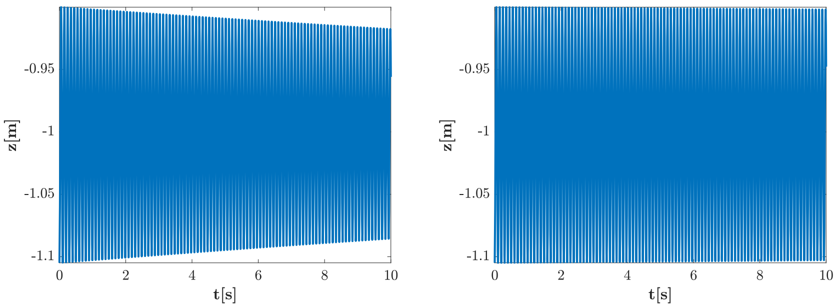

(c) $\Delta t = 0.00001s$ **(d)** $\Delta t = 0.000001s$

Figure B.4: Vertical tip displacement for free hanging truss with pre-tension $T_p = 40N$

As shown in figure B.4, the mean displacement of the truss is at $z \approx -1m$, which is the initial length. The positive and negative oscillation indicates that the system imposes a spring-like behaviour. This finding is consistent with the Hook's law which was implemented in the elastic truss model, suggesting that the model represents the physical behaviour in a proper way.

The results shown in figure B.4, indicate that the displacement of the truss over time is strongly correlated with the choice of time-step. Interestingly there is a significant damping present in the system for lower time-steps. As there are no damping terms included in the code, these results are likely to be related to numerical damping in the code. The present truss model is still used, but caution to the time-step must be taken.

Appendix C

RAO of single torus

C.1 Vertical modes

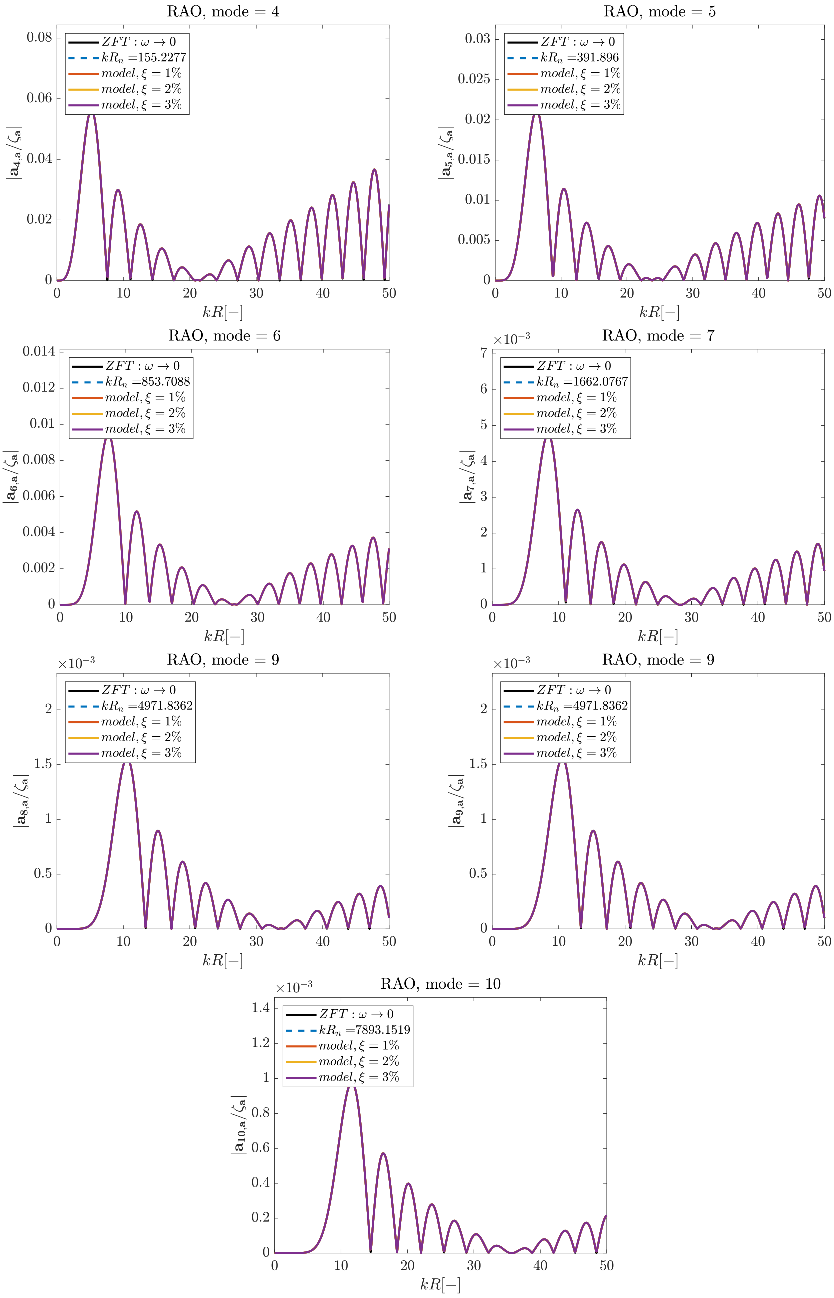

Figure C.1: RAO for higher vertical modes. Model with $\xi = 1\%, 2\%$ and 3% compared with ZFT RAO.

C.2 Radial modes

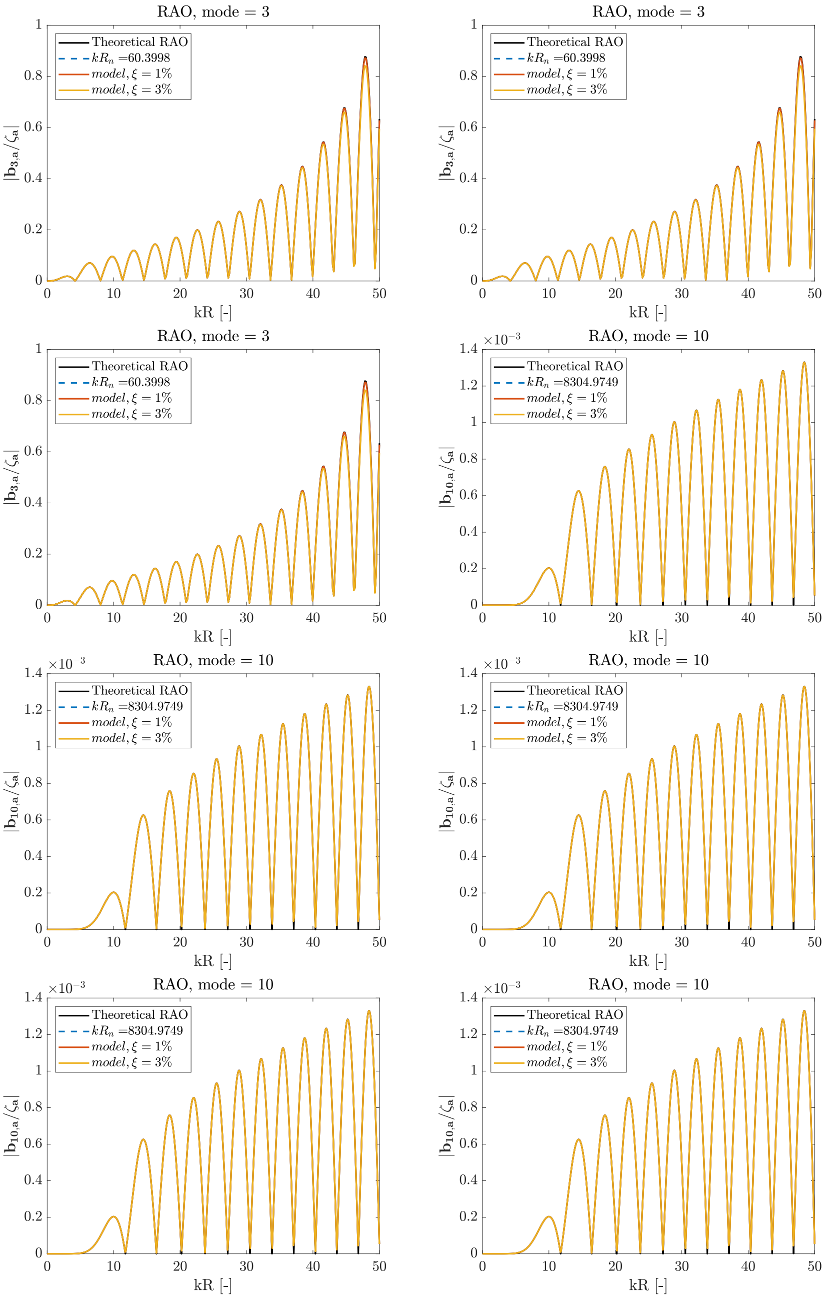

Figure C.2: RAO for higher radial modes. Model with $\xi = 1\%$ and 3% compared with theoretical RAO.

Appendix D

Additional results: two-tori and five-tori model

Table D.1 gives the properties used for the cases. These are the same to that in section 5.2. For the cases without damping of the surge mode, the properties are the same, only setting the damped surge value to zero.

Table D.1: Parameters used for the different cases. N_{tori} gives the number of tori. kR is the non-dimensional wave number with wave number k and R being the radius of the outer tori. N_{ramp} is the number of wave periods used for the ramping sequence, and t_{end} is the end-time defined by number of wave periods.

Case	N_{tori} $[-]$	kR_5 $[-]$	H/λ $[-]$	k_t $[N/m]$	$T_{p,t}$ $[N]$	Δt $[s]$	ξ_{damp} $[\%]$	N_{ramp} $[-]$	t_{end} $\cdot T_w[s]$
1	2	[0.3-10]	1/200	$148.4 \cdot 10^3$	37100	0.0025	3	10	30
2	5	[0.3-10]	1/200	$148.4 \cdot 10^3$	37100	0.0025	3	10	30

D.1 Case 1: No surge modal damping

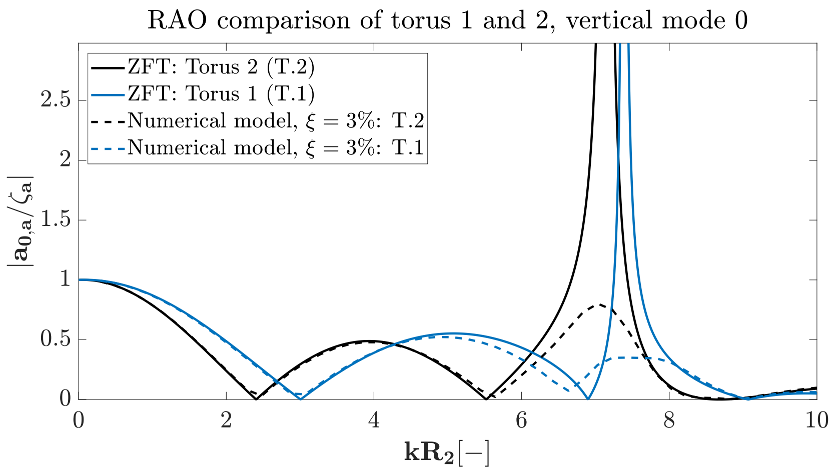

Figure D.1: RAO for heave of the inner(blue) and outer(black) torus. Numerical model with $\xi = 3\%$. No damping in surge.

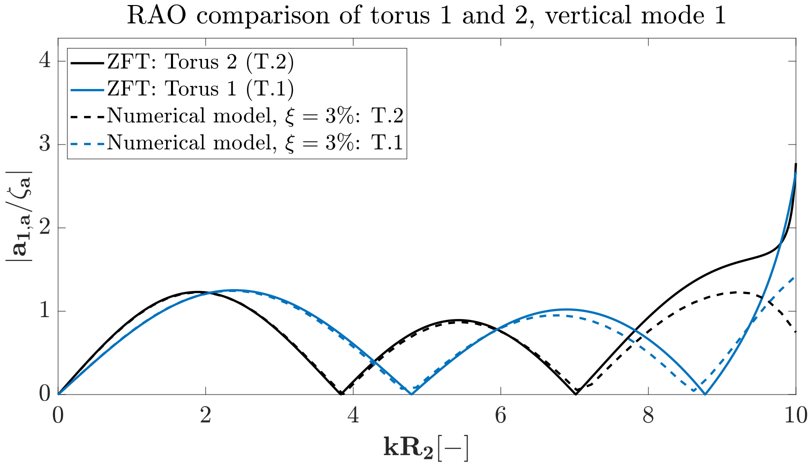

Figure D.2: RAO for pitch of the inner(blue) and outer(black) torus. Numerical model with $\xi = 3\%$. No damping in surge.

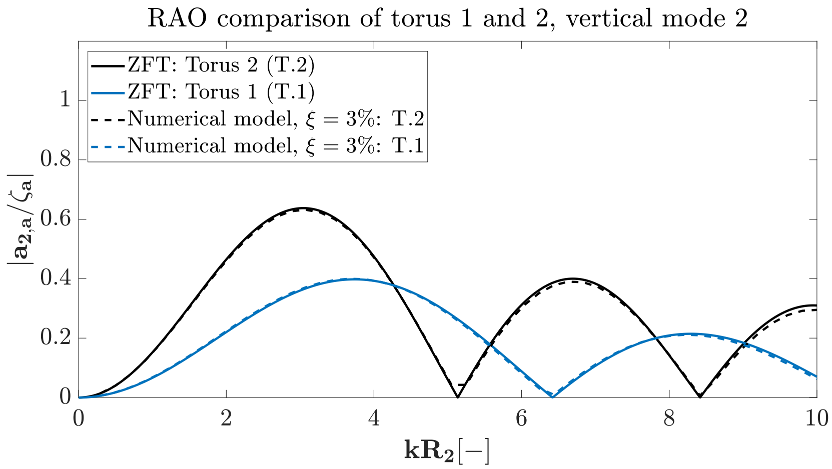

Figure D.3: RAO for first flexible vertical mode of the inner(blue) and outer(black) torus. Numerical model with $\xi = 3\%$. No damping in surge.

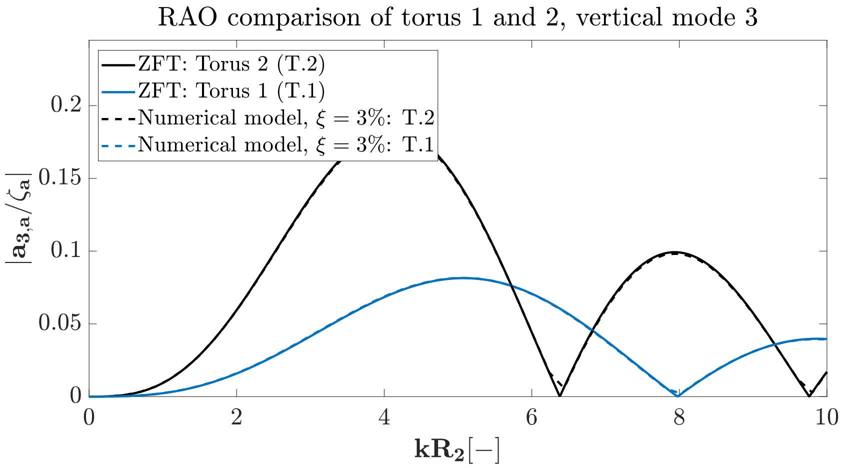

Figure D.4: RAO for second flexible vertical mode of the inner(blue) and outer(black) torus. Numerical model with $\xi = 3\%$. No damping in surge.

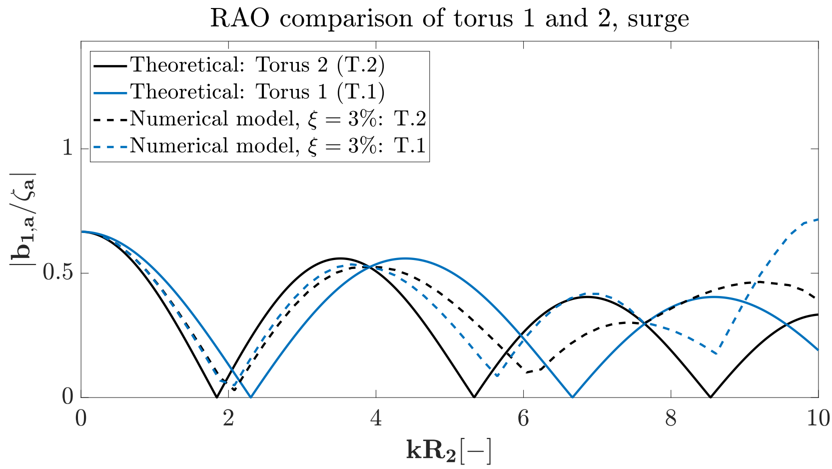

Figure D.5: RAO for surge mode of the inner(blue) and outer(black) torus. Numerical model with $\xi = 3\%$

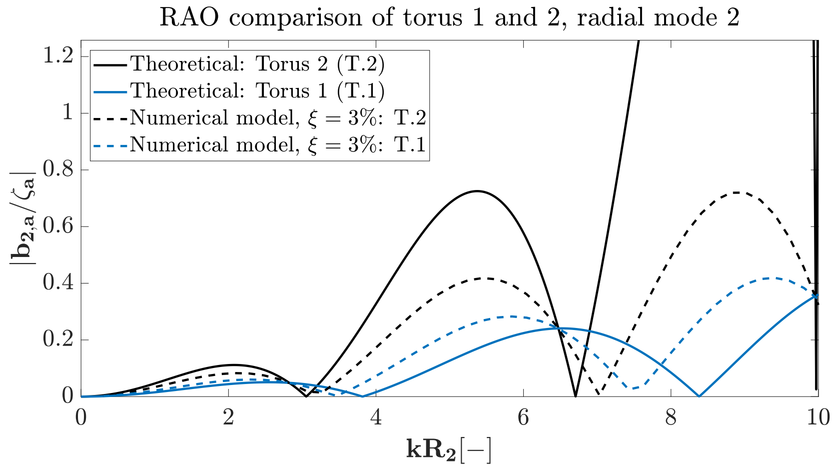

Figure D.6: RAO for first flexible radial mode of the inner(blue) and outer(black) torus. Numerical model with $\xi = 3\%$. No damping in surge.

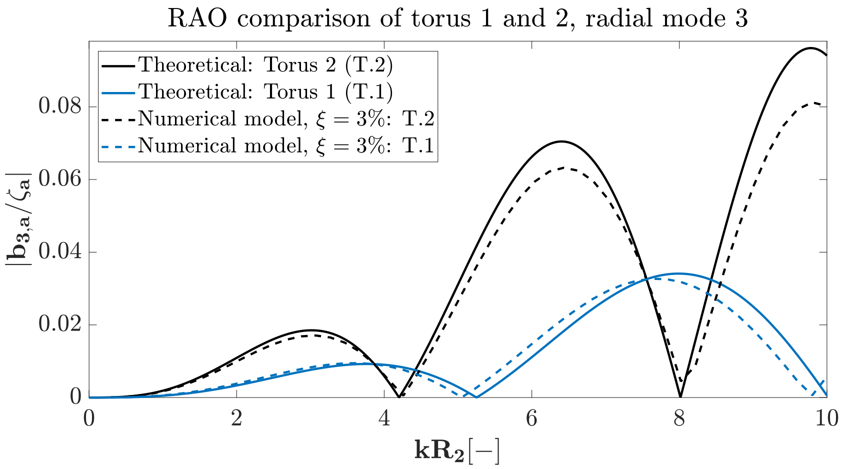

Figure D.7: RAO for second flexible radial mode of the inner(blue) and outer(black) torus. Numerical model with $\xi = 3\%$. No damping in surge.

D.2 Case 2: Additional RAOs

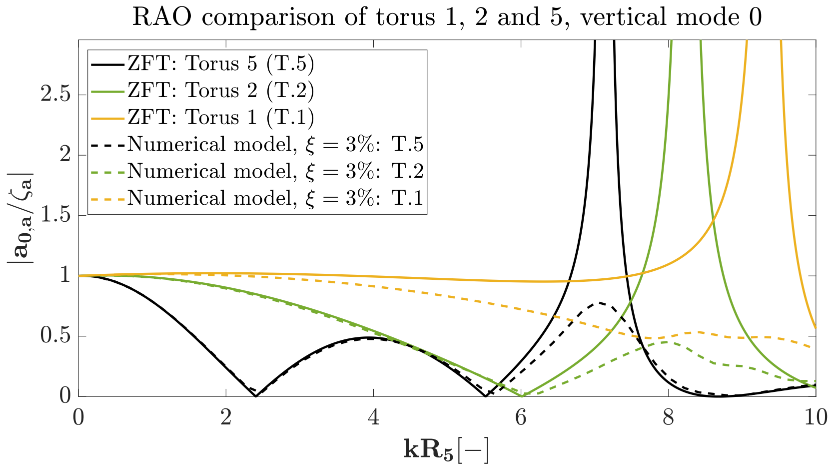

Figure D.8: RAO for heave for torus one(yellow), two(green) and five(black). Damping in surge.

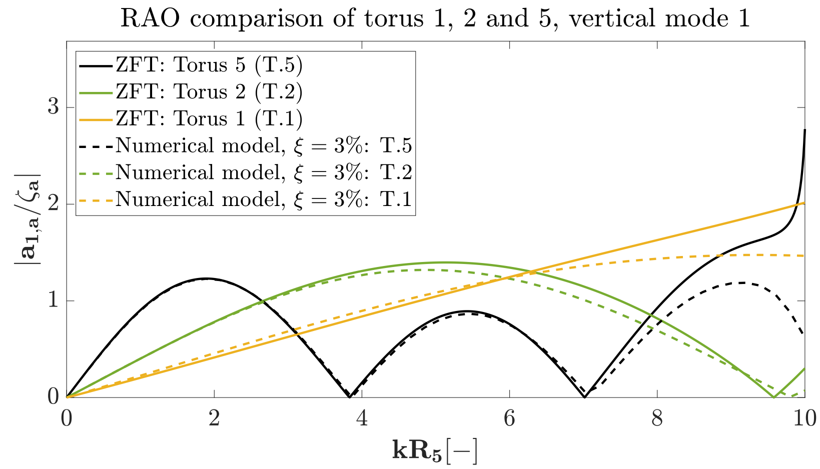

Figure D.9: RAO for pitch for torus one(yellow), two(green) and five(black). Damping in surge.

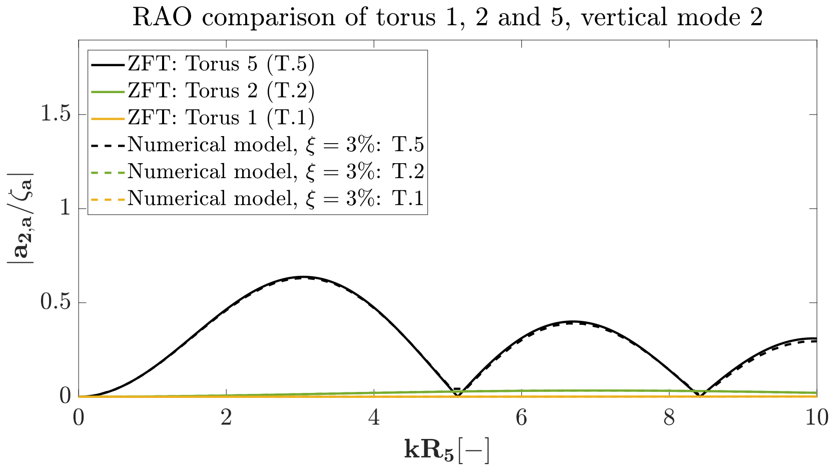

Figure D.10: RAO for first flexible vertical mode for torus one(yellow), two(green) and five(black). Damping in surge.

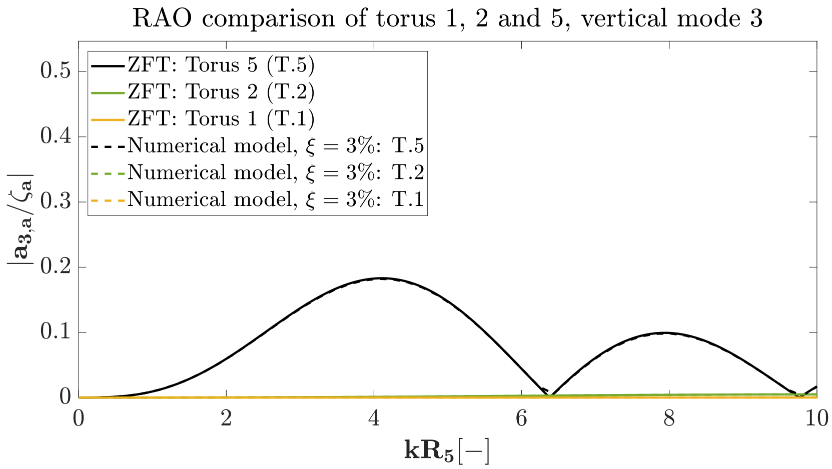

Figure D.11: RAO for second flexible vertical mode for torus one(yellow), two(green) and five(black). Damping in surge.

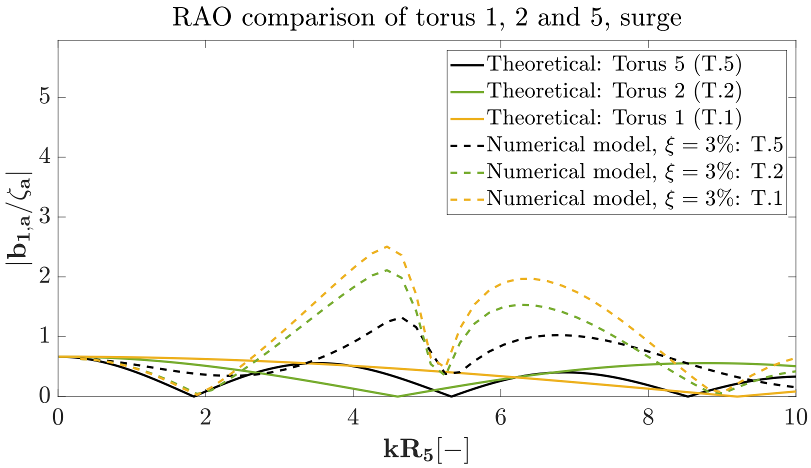

Figure D.12: RAO for surge mode for torus one(yellow), two(green) and five(black). Damping in surge.

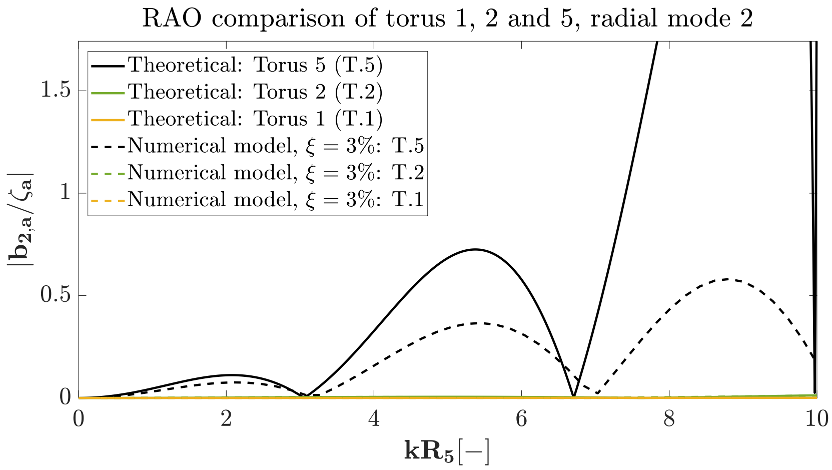

Figure D.13: RAO for first flexible radial mode for torus one(yellow), two(green) and five(black). Damping in surge.

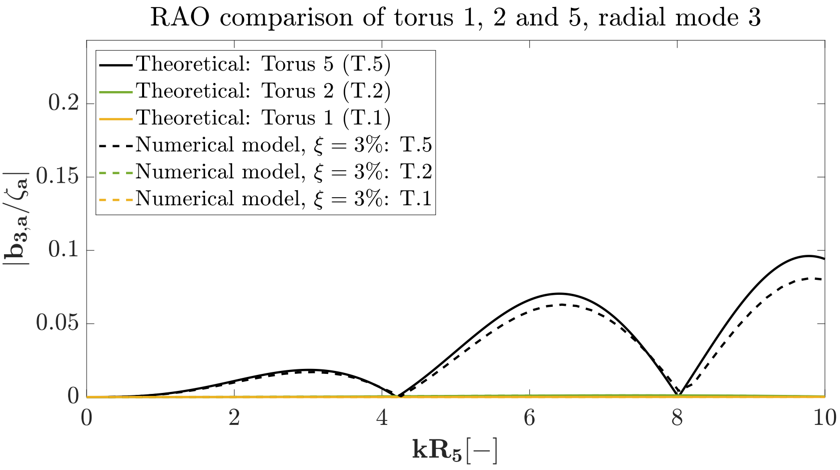

Figure D.14: RAO for second flexible radial mode for torus one(yellow), two(green) and five(black). Damping in surge.

D.3 Case 2: No surge modal damping

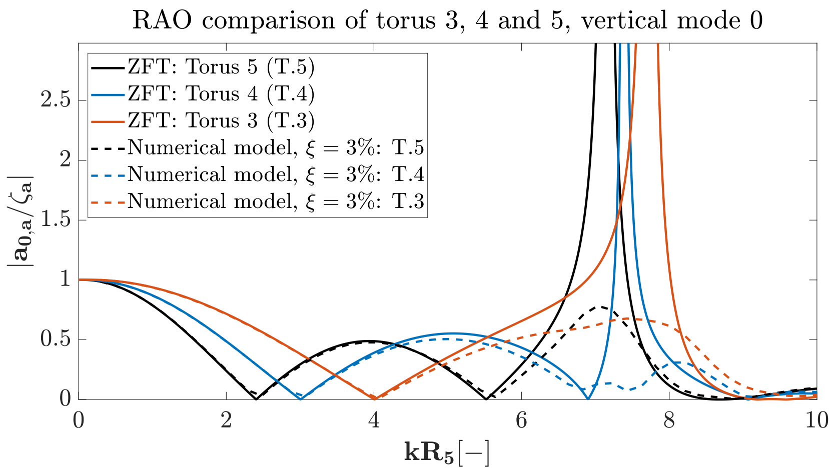

Figure D.15: RAO for heave for torus three(orange), four(blue) and five(black). No damping in surge.

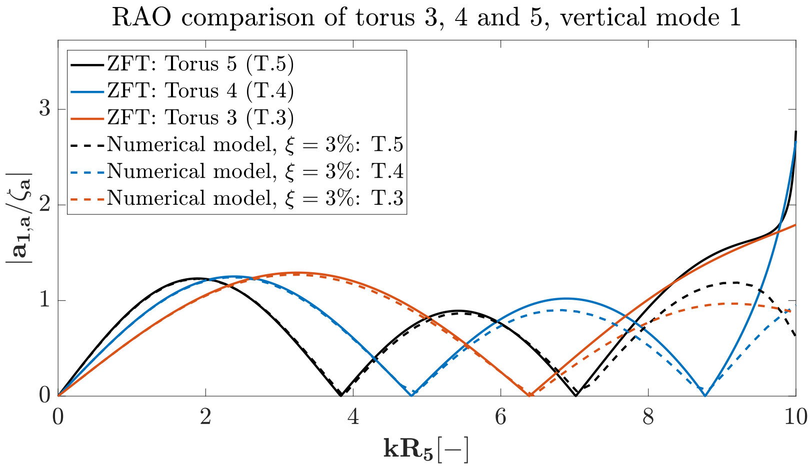

Figure D.16: RAO for pitch for torus three(orange), four(blue) and five(black). No damping in surge.

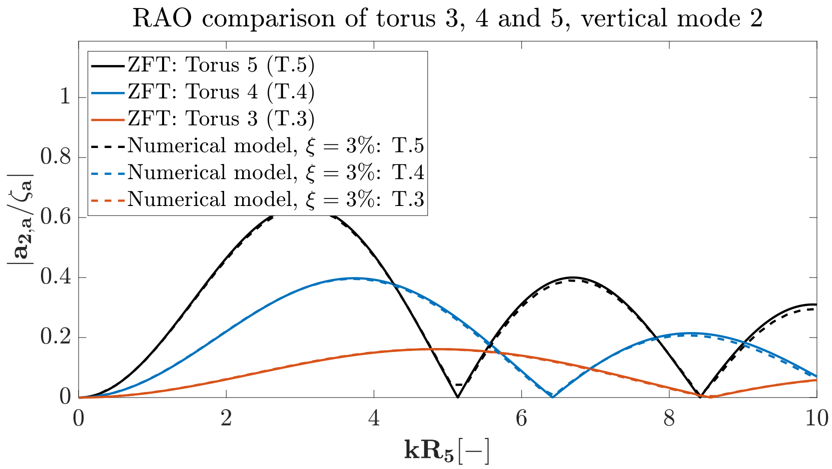

Figure D.17: RAO for first flexible vertical mode for torus three(orange), four(blue) and five(black). No damping in surge.

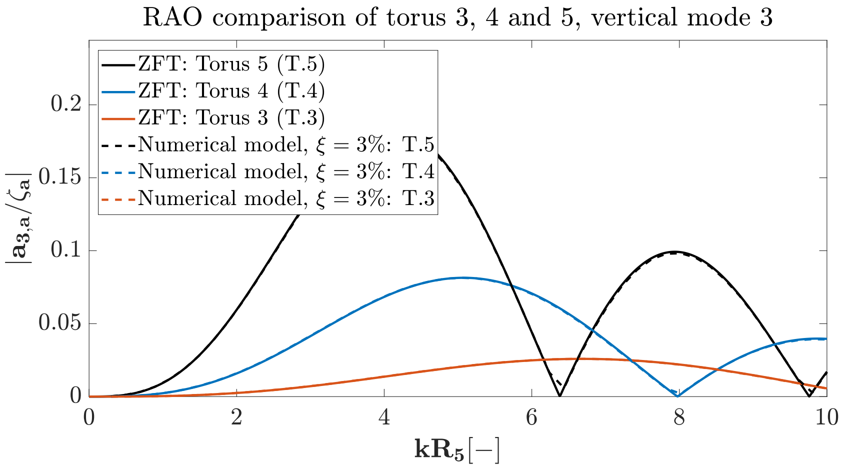

Figure D.18: RAO for second flexible vertical mode for torus three(orange), four(blue) and five(black). No damping in surge.

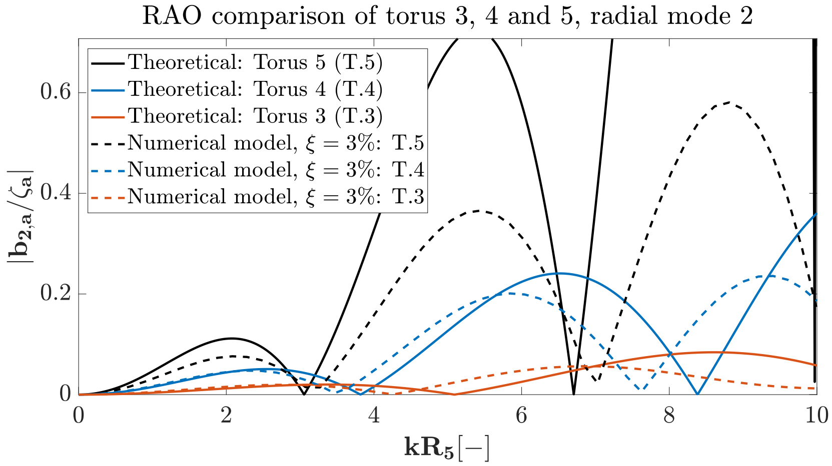

Figure D.19: RAO for second flexible radial mode for torus three(orange), four(blue) and five(black). No damping in surge.

D.4 Five-tori: Snapshot over one wave period, $T_w = 3s$.

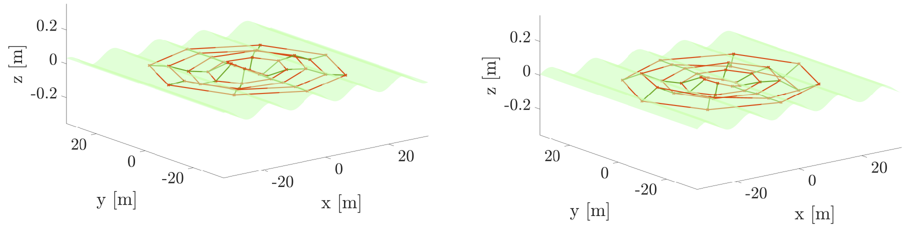

(a) $t + \frac{1}{6}T_w$

(b) $t + \frac{2}{6}T_w$

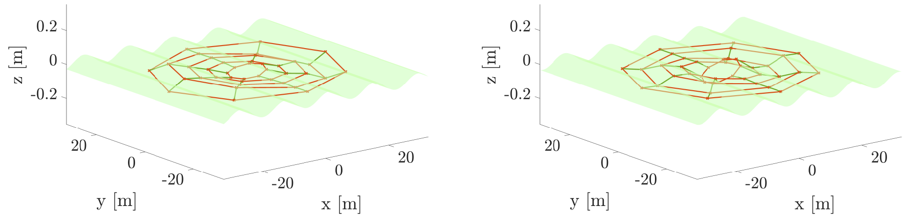

(c) $t + \frac{3}{6}T_w$

(d) $t + \frac{4}{6}T_w$

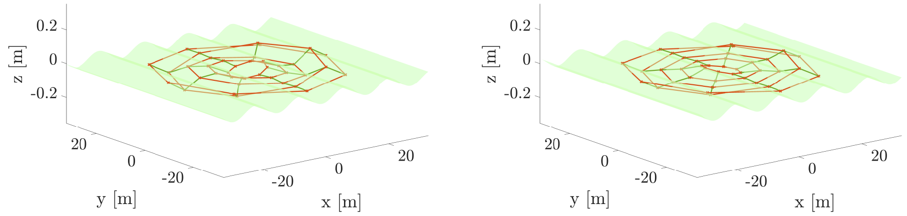

(e) $t + \frac{5}{6}T_w$

(f) $t + \frac{6}{6}T_w$

Figure D.20: Plot of full solar island, with incident wave of $T_w = 8s$, $H/\lambda = 1/200$. Orange lines are drawn between floater nodes on the same torus to illustrate the torus. Green lines are drawn between floater nodes on different tori but same direction in (x, y) space. Transparent green, represent a sinusoidal incident wave with $\zeta_a = 0.25m$.

Appendix E

Lab testing: Elastic bands used in experiments

On the 14th of May 2020, a test of the elastic bands used in the experiment was conducted. It was done to check the stiffness of the elastic bands that had been used. Two types of elastic bands were tested, and is seen in figure E.1.

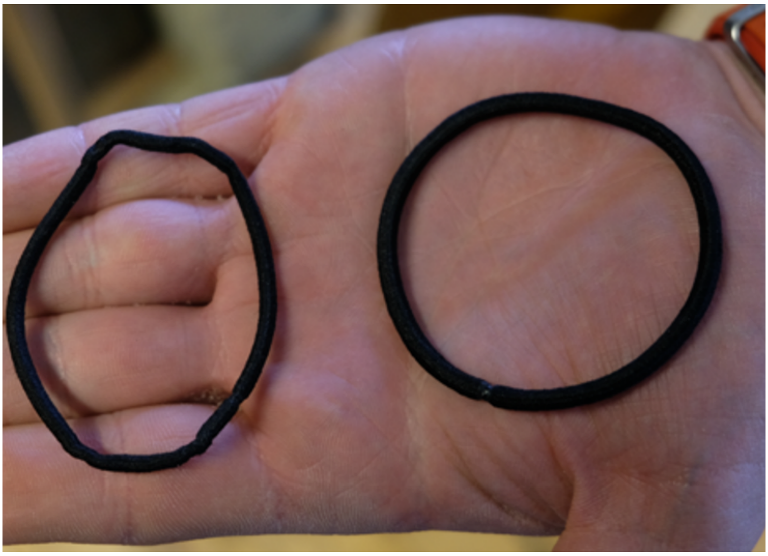

Figure E.1: Elastic bands. Band used by Mari(left), and the other(right).

The bands are similar, but some difference in size can be seen. The band to the left have been connected to the model with strips, as seen in figure E.2

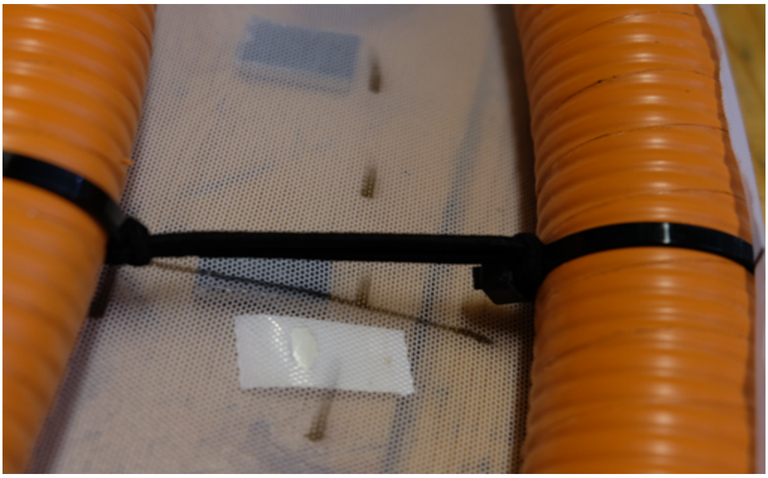

Figure E.2: Elastic bands connected to torus with strips.

Both elastic bands were connected in one end to a horizontal stick, making it to hang vertically initially. In the other end, a mass was attached, and the elongation was measured. A total of four weights were tested for both elastic bands. The initial displacement was subtracted, and the stiffness could be calculated from equation (2.9). The results can be seen in table E.1.

Table E.1: Results from stiffness test of two elastic bands with increasing added weight.

Test 1: Elastic band from (Mari)			Test 2: Elastic band (other)		
$m[kg]$	$\Delta l[m]$	$k[N/m]$	$m[kg]$	$\Delta l[m]$	$k[N/m]$
0.1	0.008	$\mathbf{122.6}$	0.1	0.005	$\mathbf{196.2}$
0.2	0.018	$\mathbf{109}$	0.2	0.017	$\mathbf{115.4}$
0.3	0.026	$\mathbf{113.2}$	0.3	0.030	$\mathbf{98.1}$
0.5	0.040	$\mathbf{122.6}$	0.4	0.057	$\mathbf{86.1}$

From table E.1 it is observed that the results show a varying stiffness with increase in added weight. Regarding Hooke's law, these should be constant. It indicates that the elastic bands do not behave according to Hooke's law.

Furthermore, it was seen that additional weight had to be applied in order for the elastic bands to elongate only in the vertical direction. Before this, the deflection was primary due to ovalising of the elastic band. After the weights were removed, the elastic bands had experienced a permanent deformation, which was more significant than that of the initial position. This indicates that the rubber inside the elastic band had been destroyed. The elastic bands are thus, exposed to degrading of their properties. This makes them behave non-linear, and further implies that they do not behave according to Hooke's law.

A degrading of the elastic bands was observed during the tests. See figure E.3.

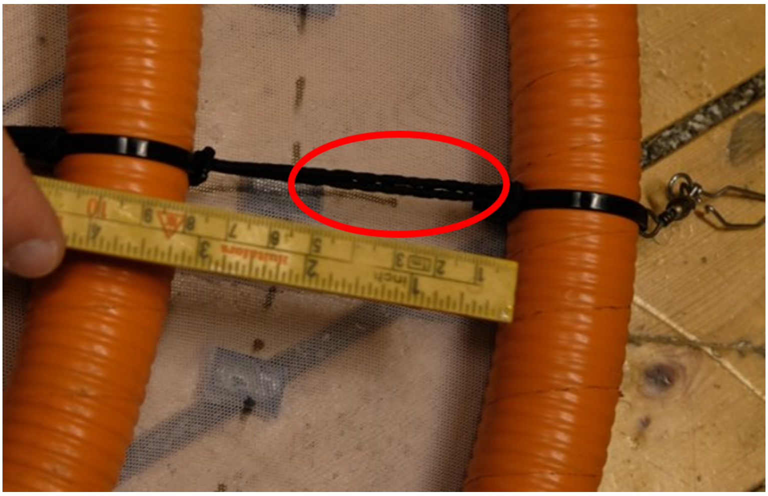

Figure E.3: Degraded elastic band connected to the solar island model. Red circle indicates the degraded part.

Øyvind Onestad Olsen

A Numerical Study of a Multi-torus Floating Solar Island Concept, with the use of Computer Programming

NTNU
Norwegian University of
Science and Technology